



POLITECNICO DI MILANO
DEPARTMENT OF PHYSICS
DOCTORAL PROGRAMME IN PHYSICS

Integrated Optical Circuits for Biosensing and Quantum Information by Femtosecond Laser Microfabrication

Doctoral Dissertation of:

Andrea Crespi

mat. 738787

Supervisor:

Dr. Roberto Osellame

Tutor:

Prof. Roberta Ramponi

The Chair of the Doctoral Programme:

Prof. Franco Ciccacci

2009 - 2011 XXIV Cycle

Contents

Introduction	iii
1 Background	1
1.1 Femtosecond laser waveguide writing	2
1.1.1 Laser-substrate interaction	2
1.1.2 Fabrication parameters	3
1.1.3 Passive photonic devices: state of the art	6
1.2 Integrated label-free optical biosensing	11
1.2.1 Refractive index sensing in lab-on-chips	11
1.2.2 Sensing by quantum light	15
1.3 Integrated quantum computing and optical simulation	18
1.3.1 Optical chips for quantum computing	18
1.3.2 Optical quantum simulation	21
1.3.3 Simulation of quantum phenomena by classical resources	24
2 Experimental	27
2.1 Waveguide writing setup	28
2.1.1 Cavity dumped oscillator	28
2.1.2 HighQLaser FemtoREGEN	29
2.1.3 Aerotech FiberGLIDE	29
2.2 Device characterization	30
2.2.1 Observation with optical microscope	30
2.2.2 Output mode characterization	30
2.2.3 Losses measurement	32
2.2.4 Polarization behaviour characterization	33
2.2.5 Waveguide fluorescence observation	33
2.3 Fiber pigtailling setup	34
3 Label-free biosensing by integrated interferometers	36
3.1 Spatially resolved label-free detection with a three-dimensional Mach-Zehnder interferometer	37
3.1.1 Motivation for the work	37
3.1.2 Development of the interferometric sensor	38
3.1.3 Integration in commercial lab-on-chip	43
3.2 Integrated quantum biosensing	46
3.2.1 Design of the optofluidic quantum biosensor	46

3.2.2	Device fabrication and measurement protocols	47
3.2.3	Experimental measurements and discussion	51
4	Integrated optical quantum computing and simulation	56
4.1	Polarization entangled states measurement on a chip	57
4.1.1	The idea behind the experiment	57
4.1.2	Development of the photonic device	58
4.1.3	Quantum characterization	64
4.2	Integrated photonic CNOT gate for polarization encoded qubits . .	67
4.2.1	A CNOT gate with partially polarizing directional couplers	67
4.2.2	Development of the photonic device	68
4.2.3	Quantum characterization	71
4.3	Experimental simulation of discrete quantum walk of bosons and fermions	74
4.3.1	The idea behind the experiment	74
4.3.2	Development of the photonic device	76
4.3.3	Quantum characterization	80
4.4	Photonic simulation of the Jaynes-Cummings dynamics	83
4.4.1	The idea behind the experiment	83
4.4.2	Fabrication of the photonic simulator	85
4.4.3	Experimental simulation of the deep strong coupling regime	88
5	Conclusions	92
A	Classical and quantum interference	95
A.1	Classical interference	95
A.2	Electromagnetic field quantization and quantum interference . . .	96
	Journal publications	99
	Bibliography	101

Introduction

Femtosecond laser microfabrication has emerged in the last decade as a powerful technique for direct inscription of low loss optical waveguides in practically any transparent dielectric substrate, showing outstanding versatility. Prototyping of new devices is made rapid, cheap and easy: optical circuits are written in the substrate, in full three-dimensional fashion, using the laser beam as an optical pen, without the need of the costly masks of conventional photolithography.

Many proof-of-principle demonstrations of the main integrated optics devices used in telecommunications have been successfully reported, including splitters, directional couplers, Mach-Zehnder interferometers and Bragg gratings. Furthermore, waveguides written in active materials have allowed to realize integrated amplifiers and laser sources. Anyway, the road towards applications has just been opened, and the unique capabilities of femtosecond laser micromachining will enable achievements inconceivable with other technologies.

In this thesis work, femtosecond laser writing is exploited to demonstrate complex photonic devices, which provide unprecedented functionalities in two applicative contexts: label-free sensing of biomolecules in microfluidic lab-on-chips, and integrated quantum computing and simulation. In the first case, the integration of Mach-Zehnder interferometers with buried microchannels is addressed, implementing interferometry with both classical and quantum light. In the second case, polarization sensitive and insensitive components are developed, which enable integrated quantum information experiments with polarization encoded qubits; in addition, phenomena governed by quantum mechanics are simulated by use of both classical and quantum light.

Chapter 1

Background

This Chapter depicts the theoretical and technological scenario in which this thesis work is placed.

In Section 1.1 the interaction between femtosecond laser pulses and substrate are briefly illustrated, the main parameters involved in the waveguide fabrication process are discussed and the state of the art of this technology is presented.

Section 1.2 illustrates the concept of lab-on-chip and the main issues regarding integrated label-free sensing, with particular focus on interferometric devices. After a review of present integrated interferometric technologies, the ideas and potential advantages of quantum sensing are introduced.

Section 1.3 recalls the main concepts and the state of the art of photonic quantum computation and simulation, highlighting the recent achievements yielded by integrated waveguides technology.

1.1 Femtosecond laser waveguide writing

Femtosecond laser waveguide writing is a powerful technique for direct fabrication of photonic devices in transparent substrates. Originated from a seminal work of Davis et al.[1], this technique has been object of growing interest and it has allowed in the last decade the demonstration of increasingly complex devices, for application fields ranging from telecommunications to integrated biosensing[2, 3].

As detailed in the following, this technology is based on nonlinear absorption of focused ultrashort laser pulses to induce localized and permanent modification of a dielectric material. In particular, for waveguide fabrication, the irradiation parameters are tuned to obtain a smooth refractive index increase. The optical circuit is produced by translating the sample under the laser beam along the desired path.

This gives to femtosecond laser writing several important advantages over conventional lithographic techniques for photonic devices fabrication:

- it is a single-step and maskless process, allowing important cost reductions and process speed-up, especially for small scale productions and prototyping of new devices
- it can be easily applied to different materials without changing the process, but just by tailoring the irradiation parameters
- it is an intrinsically three-dimensional technology, since it allows to directly fabricate waveguides at arbitrary depth in the substrate

It is worth noting that the latter is a unique capability of femtosecond laser writing that enables to develop circuit designs that are otherwise impossible to realize.

1.1.1 Laser-substrate interaction

In the femtosecond laser writing process, laser pulses interact with transparent dielectrics, where the photon energy $E_{\text{ph}} = hc/\lambda$ is smaller than the bandgap energy E_{g} . This implies the absence of linear absorption phenomena and this is indeed the key point of the intrinsic three-dimensionality of the technology. In fact, being driven by *non linear* phenomena, such as multiphoton, tunneling and avalanche ionization, the energy absorption and the resulting permanent modification is localized in the focal region.

Absorption of femtosecond pulses occurs on a time-scale that is typically shorter than the energy transfer to the lattice[4]. This actually decouples the two phenomena, which happen distinctly and in succession.

First, the leading edge of the pulse generates a seed of free electrons through nonlinear photoionization. For the electric field intensities of femtosecond pulses, multiphoton and tunneling ionization compete. Multiphoton ionization consists of simultaneous absorption of m photons, so that $mE_{\text{ph}} > E_{\text{g}}$. In tunneling ionization the intense electric fields deforms the energy barrier of the Coulomb potential, enabling electrons to tunnel from the valence to the conduction band.

This initial seed of free electrons is then amplified by avalanche ionization, creating an electronic plasma which, at a certain point, increasing in density, starts to absorb linearly the remaining energy of the pulse. The relative contribution of the different nonlinear ionization processes is still debated[5, 6].

On a time-scale of some picoseconds the absorbed energy is transferred to the lattice. The precise microscopic mechanisms that lead to the refractive index increase are not yet fully understood and are still under investigation. Diverse interaction phenomena enter into play, including colour center formation, densification, thermal diffusion and accumulation. The relative role of each of them has not been completely clarified[7, 8, 9, 10]; it depends anyway on the material and the exposure conditions.

It is worth stressing the fact that the interaction with femtosecond pulses is a highly deterministic process[5, 6], if compared to longer pulses. For pulses longer than a few tens of picosecond the intensity is not high enough to trigger the nonlinear photoionization processes described above. Anyway, it is sufficient to produce relevant avalanche ionization starting from a seed of free electrons already present in the material, i.e. either thermally excited or due to impurity and defect states. The number of these electrons is typically low and fluctuates in time and space, making the interaction process non-deterministic.

1.1.2 Fabrication parameters

1.1.2.1 Pulse energy and translation speed

Depending on the energy of the focused femtosecond laser pulses, qualitatively different features arise from the interaction process. In particular, three kinds of structures may be observed[11, 12, 13].

For low pulse energies a smooth refractive index change may be produced. The magnitude and the spatial distribution of the refractive index change varies from material to material, showing in general both positive and negative refractive index contrast. This energy interval is the most relevant for waveguide writing applications.

In fused silica glass, for slightly higher pulse energies, the formation of birefringent nanostructures is observed. The birefringence axis of these structures depends on the irradiation polarization[14, 15, 16]. This phenomenon has been exploited to demonstrate waveguides and photonic devices with polarization dependent characteristics.[16] In addition, the presence of these nanostructures in fused silica has been shown to give an elevate etching selectivity in HF solutions. The acid corrodes the irradiated substrate at a much higher rate than the bulk material, allowing to fabricate directly buried microchannels[17].

For even higher pulse energies femtosecond pulses may induce microexplosions, which result in microvoids formation. While these modifications do not generally show waveguiding properties, interesting applications have been envisaged for high-density three-dimensional data storage, where these submicron-size microvoids represent voxels (volume pixels). Readout can be performed exploiting scattering or luminescence [18, 19].

For a given pulse energy, the translation speed controls the amount of total energy deposited per unit volume and typically influences the achieved refractive

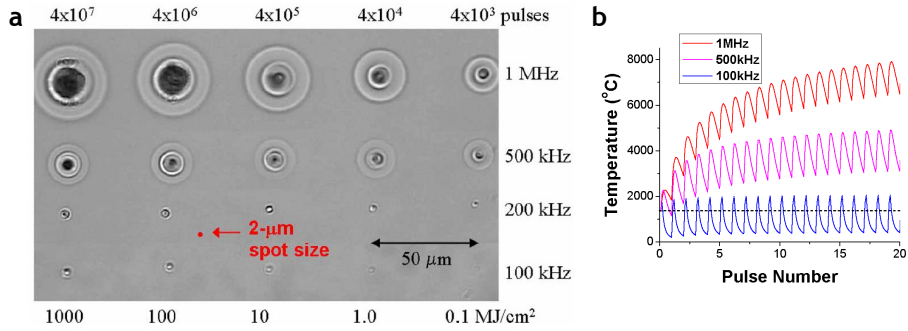


Figure 1.1: (a) Heat accumulation effects enlarge the modified region with increasing repetition rate and number of pulses, at fixed pulse energy. (b) Numerical simulation of the glass temperature (Schott AF45) as a function of time, for different repetition rates. Above 100 kHz repetition rate thermal effects of subsequent pulses accumulate. Both images are reprinted from Ref.[20].

index change. Anyway, given the non-linearity of the interaction process, lowering (increasing) the speed with the same pulse energy is in general not equivalent to increasing (lowering) the pulse energy for a fixed speed. The translation speed can also modulate cumulative thermal effects, which are the object of the following paragraphs.

1.1.2.2 Repetition rate: the occurrence of thermal effects

The repetition rate of the femtosecond laser pulse train is a crucial parameter which has a strong influence on the waveguide writing process, determining completely different regimes.

In the low repetition rate regime ($1 \div 250$ kHz), typical of traditional Ti:sapphire regeneratively amplified laser systems, the material cools down to the original temperature after the irradiation of each pulse; thus the substrate modification is mainly determined by individual pulses[20]. The shape of the modified region coincides with the irradiated volume and beam shaping techniques are required in order to obtain circular waveguide cross-sections.

If the repetition rate is increased to several MHz, such that the time interval between two consecutive pulses is much shorter than the heat diffusion time (which is about $1 \mu\text{s}$), strong cumulative thermal effects take place[21, 22]. In this regime femtosecond laser oscillators without amplification stage are typically employed, delivering low energy pulses, which require to be focused by high numerical aperture oil-immersion objectives in order to trigger the nonlinear absorption. Due to the tight focusing conditions, the region directly irradiated by the individual pulses is very small. However, thermal accumulation and heat diffusion generate a much larger modified region, which extends isotropically, thus providing a circular waveguide profile without the need of beam shaping techniques.

A very interesting regime is observed at intermediate repetition rates (hundreds of kHz to few MHz), in which a gradual appearance of the thermal accumulation effects occurs[23, 20, 24] (see Figure 1.1). To work in this repetition

rate regime Yb-based laser systems are a common choice, since they are capable of pulse energies up to some μJ . Tight focusing is no longer required and long working distance objectives can be employed, enabling a full exploitation of the three-dimensional capabilities of the laser writing technology. The region directly modified by the laser pulses, in this case, has comparable size to the thermal affected region and the advantages of the two regimes can be combined: a stronger refractive index increase, given by the action of more energetic pulses, comes together with thermal effects that help to make the waveguide more uniform and circular.

1.1.2.3 Writing geometries and beam shaping techniques

Two different writing geometries are traditionally identified, depending on the direction of translation of the sample under the laser beam for the femtosecond irradiation: longitudinal and transverse[1, 25].

In the longitudinal geometry, the sample is translated along the beam propagation direction. As a consequence, the produced waveguide has intrinsic transverse circular symmetry, with dimensions on the order of the focal spot size. However, the overall waveguide length is limited by the working distance of the microscope objective adopted.

In the transverse geometry, the sample is translated orthogonally to the beam propagation direction. The waveguide cross-section in this case becomes strongly asymmetric, since the width is approximately twice the beam waist w_0 , while the depth has a dimension comparable to the (much larger) confocal parameter of the focused writing beam $2nw_0/\text{NA}$ (where n is the refractive index of the glass and NA the numerical aperture of the objective). Despite this disadvantage, the gain in terms of design flexibility is enormous, since this gives complete freedom on a glass sample which is commonly few millimeters thick but some centimeters wide.

Beam shaping techniques have been indeed developed to fabricate circular cross-section waveguides, which yield good mode matching with optical fibers, even in the transverse writing geometry. These techniques enlarge the focus dimension in the plane orthogonal to the translation direction, in order to obtain a disc-shaped focal volume. A first beam shaping technique employs a cylindrical telescope[26] before the focusing objective. The demagnification ratio of the telescope reduces the beam dimension along one direction, producing an elliptical beam and a larger focus along that direction. The shape of the focal spot is then finely tailored controlling the beam astigmatism, by translating one of the lenses of the telescope. Another technique obtains similar results by employing a slit in place of the telescope[27, 28]. It basically consists in a spatial filtering of the beam, to reshape the focal spot. The setup is simpler than in the case of the telescope, but it implies the loss of a considerable amount of power.

A completely different technique for fabricating waveguides with symmetric cross-section is multi-scan irradiation[29, 30]. Many lines are written, each of them with elongated cross-section, slightly shifted relative to each other. An overall square and symmetric cross-section is thus obtained.

It is worth noting that, if a very high repetition rate is adopted, a circular

waveguide profile may be obtained in some materials (as mentioned before), due to isotropic thermal effects, without any beam shaping technique, even in the transverse writing configuration[31].

1.1.3 Passive photonic devices: state of the art

Femtosecond laser micromachining has proved in the recent years its capabilities in the fabrication of waveguides on diverse substrates, both passive and active, which have led to the demonstration of passive photonic circuits of growing complexity, waveguide amplifiers and lasers[2, 32]. Long period gratings and Bragg gratings have also been directly fabricated in optical fibers by femtosecond pulses[33, 34], as well as waveguide Bragg gratings[35]. It is also worth mentioning the possibility of integrating on the same substrate optical elements and microfluidic channels[36, 37], both fabricated by femtosecond lasers.

Due to the vastness of the applications, this section will focus only on the state of the art of femtosecond laser written passive photonic devices, since these are the ones most related to the subject of this thesis.

1.1.3.1 Y splitters

Y splitters have been demonstrated by femtosecond laser writing since the early years of this technology. A 1×2 Y splitter was demonstrated in 1999 in pure fused silica[38]. The longitudinal writing configuration was adopted, exploiting the 2 cm allowed working distance of a 10X objective. The fabricated structure was able to guide and split 514.5 nm light from an argon laser, with a splitting ratio close to 1:1. An analogous device was displayed some years later in lithium niobate[39], using the transverse writing configuration.

More complex devices, such as a 1×4 splitter[25] and a 1×8 splitter[40] have also been reported, respectively in aluminosilicate and fused silica glass (see Figure 1.2a-b), demonstrating in both cases well balanced power repartition in the output arms.

A unique possibility of femtosecond laser waveguide writing is that it can provide arbitrary three-dimensional waveguiding paths in the bulk, which is hardly possible with traditional lithographic technologies. The first demonstration of such a 3D device was reported by Nolte et al.[41] (see Figure 1.2c). A 1×3 splitter was realized in fused silica by an amplified Ti:sapphire laser. The three branches split at angles of 120° , each lying on a different plane. An almost equal 32:33:35 splitting ratio was measured at 1050 nm wavelength.

It can be noticed that, in order to fabricate Y splitters by femtosecond laser pulses, the common branch needs to be irradiated (at least) twice. This might in principle affect the waveguide properties with respect to a single scan. Some authors observed no discernible change[25] in the waveguide diameter with increasing number of passes; elsewhere[41] the input port of the splitter was found to become slightly multimode because of the multiple irradiation, while the output ports, irradiated only once, were reliably monomode.

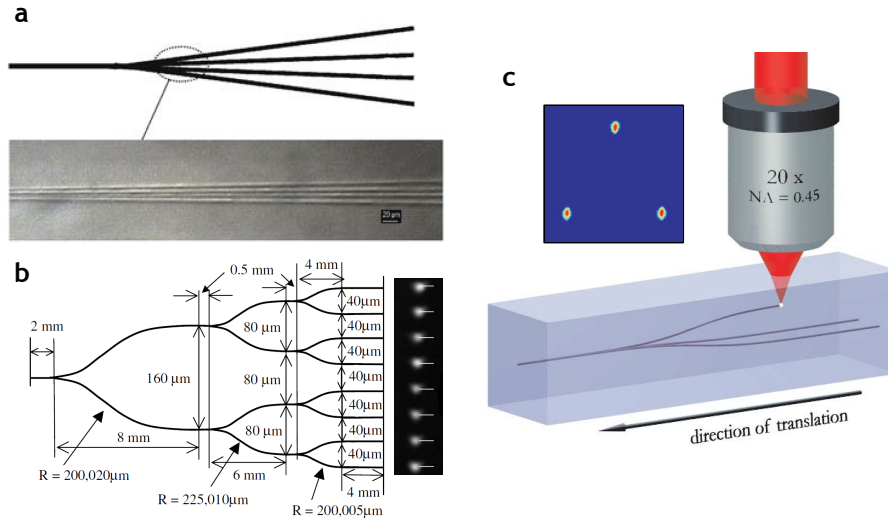


Figure 1.2: (a) Schematic and microscope image of a detail of a femtosecond laser written 1×4 splitter[25]. (b) Schematic of a 1×8 splitter, composed of cascaded 1×2 Y splitters[40]. (c) Femtosecond laser fabrication of a three-dimensional 1×3 splitter[41].

1.1.3.2 Directional couplers

In a directional coupler two waveguides are brought close and couple by evanescent field, so that optical power is exchanged between the waveguides, according to the coupled mode equations[42]. The behaviour of the device is very sensitive to even slight imperfections or variations in the circuit design or waveguide properties. Hence, the realization of directional couplers can be an effective benchmark for the capabilities of the fabrication technology.

Femtosecond laser written directional couplers were first reported in borosilicate glass, using the second harmonic of a high repetition rate Ti:sapphire oscillator[45].

Directional couplers operating in the full range of telecom wavelengths were demonstrated by Eaton et al.[46], displaying the reliability of the laser writing technology and marking an important step towards the applications. The devices were micromachined at high scan speed ($7 \div 25$ mm/s) in borosilicate glass by 1 MHz repetition rate laser systems. They showed low insertion losses (~ 2 dB), and single-mode operation with good overlap with the mode of standard telecom fibers. These results were later extended and improved by the same group, reporting both broadband directional couplers[47] and wavelength demultiplexers[48]. The spectral behaviour of these devices was controlled by tuning both the writing parameters and the coupler geometry.

The capabilities of femtosecond laser writing were exploited to demonstrate couplers with three-dimensional and innovative design (see Figure 1.3). Three-dimensional couplers involving three waveguides[49, 43] were reported, as well as X couplers with the two waveguides on different planes[44].

In addition, by inserting a spatial light modulator in the writing beam, it

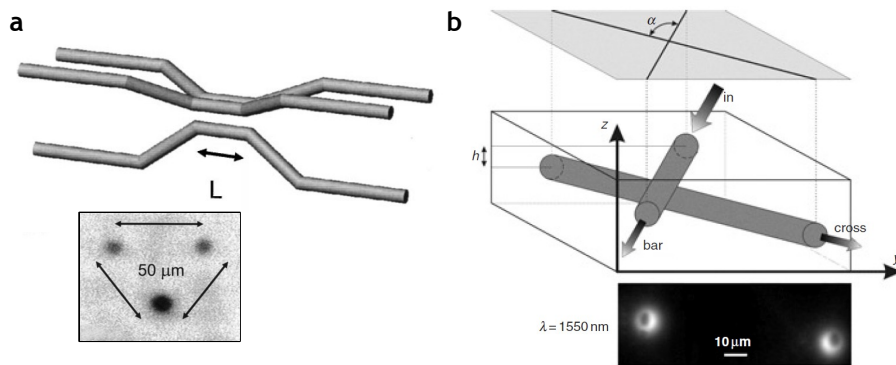


Figure 1.3: (a) Schematic of a three-dimensional 3×3 symmetric directional coupler[43]; in the inset inverse gray-scale CCD image of the waveguide outputs showing a balanced power splitting ratio. (b) Schematic of a vertical X coupler with waveguides on different planes[44]; a picture of the near-field of output facet at 1550 nm is reported below.

is possible to produce more than one focusing spot with a single objective, and simultaneous writing of the two branches of the directional couplers can be achieved[50, 51]. The dynamic variation of the phase pattern of the spatial light modulator allows to control in three dimensions the positions of the multiple foci.

1.1.3.3 Mach-Zehnder interferometers

Splitters and couplers, discussed in the previous paragraphs, are the building blocks for realizing more complex devices, such as Mach-Zehnder interferometers (MZIs). A MZI is composed of a first splitter or coupler, which divides the input power into two branches. Light from the two branches interferes on a second splitter or coupler and the output power depends on the phase difference between the two light beams. The origin of such phase difference can be a geometric imbalance of the two branches as well as a variation in the refractive index. Depending on the target application, the phase difference can be fixed or dynamically controlled in order to route or filter the input light; otherwise the phase itself can be object of measure.

One of the first demonstrations of a MZI fabricated by femtosecond laser micromachining was reported by Minoshima et al.[52]. The device was fabricated by a 4 MHz Ti:sapphire laser oscillator in sodalime glass and displays a very simple geometry, composed of two X couplers placed back to back with a crossing angle of 2° (see Figure 1.4a). Wavelength filtering functionality is achieved by the geometrically unbalanced design. By injecting broadband infrared light, interference fringes were observed in the transmission spectrum, whose periodicity fits for a $9.3 \mu\text{m}$ path imbalance. This showed good agreement with the design path length difference of $10 \mu\text{m}$.

Achieving the desired transmission spectrum in a MZI may be challenging. In fact, small imperfections or variations of the refractive index of the waveguides are sufficient to appreciably shift the interference fringes with respect to the design.

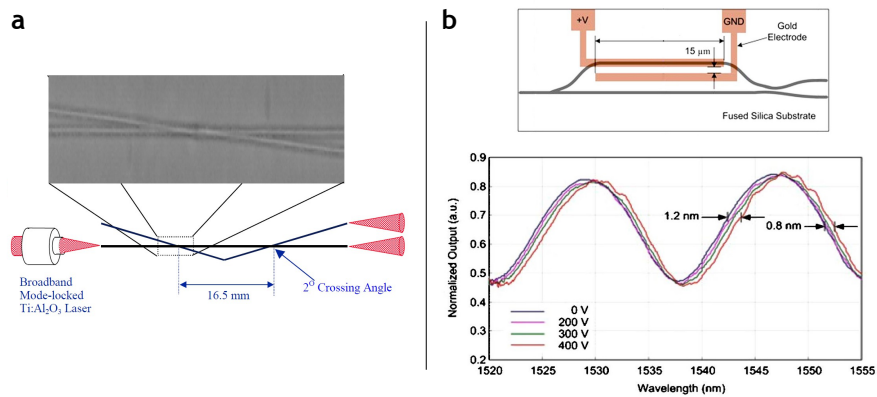


Figure 1.4: (a) Schematic of a MZI, composed of two X couplers[52]. In the blow up, microscope image of a detail of one coupler. (b) (top) Schematic of the Mach-Zehnder electro-optic modulator realized in fused silica substrate[54]. Thermal treatment induce second order nonlinearity; gold electrodes are deposited on the surface. (bottom) Spectral responses of the electro-optic modulator for increasing voltages.

Interestingly, Florea and Winick reported[53] successful tuning of a femtosecond laser written optical interleaver by performing a new irradiation with femtosecond pulses, localized on one of the interferometer's arm. The new irradiation shifts the interference fringes in the spectral response of the device: a real time monitoring of the device transmission allowed to achieve the desired fringes position.

The combination of femtosecond laser writing and thermal poling enabled the demonstration of a Mach-Zehnder electro-optic modulator in fused silica[54] (see Figure 1.4a), using a 238 kHz repetition rate laser at 790 nm wavelength and a writing speed of 100 $\mu\text{m/s}$. The substrate region in which the two interferometer's arms are fabricated by laser pulses is thermally treated so to induce an electro-optic coefficient. Gold electrodes, subsequently deposited on the surface of the sample, allow to impose an external electric field and thus modulate the refractive index seen by the light travelling in the two arms, generating a phase difference between them. The interferometer was actually designed with a three-dimensional geometry, thus exploiting the capabilities of the femtosecond laser writing technology. In fact, the input Y splitter and the output directional coupler were deeply buried in the substrate, to be less sensitive to surface or edge defects. The two arms, on the contrary, were written closer to the surface, to maximize the overlap with the 20 μm thick nonlinear layer induced by the thermal treatment.

A Mach-Zehnder electro-optic modulator was also reported by Liao et al.[55], directly fabricated in lithium niobate, one of the most common electro-optic materials. Propagation losses at 633 nm were measured as low as 1 dB/cm. Femtosecond laser pulses were also exploited for ablating and treating microgrooves in which copper electrodes were selectively deposited.

1.1.3.4 Discrete waveguide arrays

A class of photonic structures of preeminent scientific importance are discrete arrays of evanescently coupled waveguides. In fact, the Maxwell's equations formalism describing light propagation in such waveguiding structures offers interesting analogies with the formalisms employed in a wealth of other fields of physics, including quantum mechanics, atomic dynamics, solid state physics (see also Section 1.3.3).

These formal analogies have been investigated for decades[56]; however, research in this field is still active and flourishing of new ideas. In particular, the freedom provided by femtosecond laser waveguide writing have enabled many interesting experimental results in the recent years.

More than reviewing all these results, here we will aim at highlighting some significant examples in which the capabilities of the present fabrication technique have been advantageously exploited for developing and realizing this kind of photonic structures.

A first striking capability of femtosecond laser writing is its intrinsic three-dimensionality. This characteristic enabled the realization of two-dimensional waveguide arrays, with both square and hexagonal symmetry[57, 58] (Figure 1.5a). Waveguides were fabricated in fused silica by a Ti:sapphire amplified femtosecond laser system. Discrete diffraction was observed in the arrays, in experiments conducted at single wavelengths as well as with white light, obtaining good agreement with the theory.

The three-dimensional design also provides a further degree of freedom for engineering the coupling coefficients between waveguides, in particular their wavelength dependence[59].

By injecting high peak power laser pulses in properly designed three-dimensional arrays, the formation of two-dimensional spatial solitons has also been demonstrated [60, 61] (Figure 1.5b), showing dynamics governed by a nonlinear Schrodinger equation. The refractive index variation caused by third-order nonlinearity determines a change in the propagation constants of the waveguides, which reduces or even inhibits the evanescent coupling, resulting in discrete localization of the propagating light.

The capability of femtosecond laser pulses to process different materials can be exploited to fabricate waveguides in fluorescent substrates, in order to have a direct visualization of the propagation of the light in the arrays. For example, a curved waveguide array fabricated in an Erbium doped substrate allowed to directly observe the optical analogue of Bloch oscillations[63], by imaging the green upconversion signal.

Even more interestingly, femtosecond laser irradiation of fused silica rich in hydroxide content creates colour centers, emitting at 650 nm wavelength when excited with a 633 nm He:Ne laser. Thus, femtosecond laser writing in fused silica produces naturally fluorescent waveguides, where direct observation of the propagation pattern is enabled[64]. To mention just a few examples, this method was used to investigate dynamic localization in curved waveguide arrays[62] (Figure 1.5c), inhibition of light tunneling in arrays where a sinusoidal modulation of the propagation constant was provided by modulating the writing speed[65], effects of disorder and Anderson localization[66].

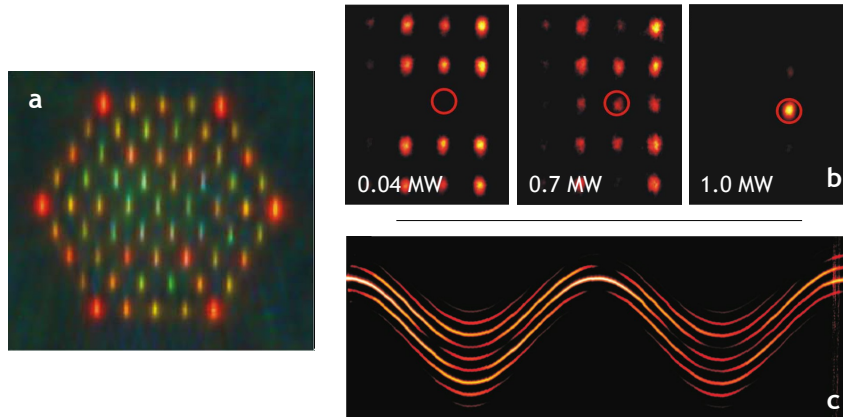


Figure 1.5: (a) Output colour intensity pattern of an hexagonal waveguide array, excited with white light[58]. To different wavelengths correspond different coupling coefficients and different output distributions. (b) Observation of a two-dimensional spatial soliton in a waveguide array[60]. Injecting laser pulses with increasing peak power, evanescent coupling decreases and light remains confined in the input waveguide (marked with a red circle). (c) Experimental fluorescence pattern showing dynamic localization of light in sinusoidally bent waveguides[62].

1.2 Integrated label-free optical biosensing

1.2.1 Refractive index sensing in lab-on-chips

1.2.1.1 Lab-on-chip technologies

Lab-on-chips (LOCs) are miniaturized systems aiming at the integration onto a single substrate of several functions[67, 68, 69], which would typically require an entire biochemical laboratory. The basis element of a LOC is a network of microfluidic channels[70], which is employed to manipulate very small volumes of biological samples (in the order of microlitres and nanolitres). Biochemical reactions and analyses can be performed directly on chip, with the possible aid of other integrated microcomponents, including filters, pumps, valves, mixers, electrodes and optical elements.

Extreme miniaturization and integration of diverse functionalities are the key concepts of the growing success of LOC technologies in the recent years. Size reduction provides for example better performance in terms of reduced reagent consumption, analysis speed, possibility of performing on the same chip different processes in parallel, easy automatization of the measurement process. The growing number of integrated functions has multiplied the field of applications, which include biology, chemistry, genomics, cellomics, clinic and forensic analysis.

Typical dimensions of the microchannels cross-section are in the order of few hundreds of microns. Hence, the surface-volume ratio becomes remarkably high and interesting surface effects arise, which are negligible in common macroscopic devices but here can be exploited for applications. The liquid flows in the laminar regime, thus there is no mixing, unless particular channel shapes are adopted (micromixers). With the application of an external electric field, electroosmotic

flow¹ may occur: this allows to finely control the motion of the fluid in the microfluidic network just by electrodes and without using pumps and moving parts.

It is worth mentioning the main substrates and fabrication techniques commonly employed for LOCs. First of all glasses (e.g. fused silica, pyrex, other borosilicate glasses), which are appreciated for their transparency and good chemical and biological compatibility. In this case fabrication employs well-established lithographic processes, developed by the electronic industry. By adding lithographic steps it is also possible to integrate electrodes or more complex electronic devices, useful for controlling fluxes in the microchannels or for detection. Lithography is anyway an expensive technology, suited for large scale productions but hardly convenient for prototyping new devices. Recently, polymeric LOCs are being developed: the polymeric substrate is typically cheaper than glass and machining can be performed by techniques borrowed from the plastic industry (e.g. replica moulding, injection moulding), which do not need the expensive instrumentation of lithography. Drawbacks of polymers include anyway possible chemical reactivity or biological incompatibility, as well as poor resistance to high temperatures and solvents.

1.2.1.2 Detection schemes for lab-on-chips

The reduced analysis volumes, which constitute a central advantage of LOC technology, mean on the other hand that the analyte quantity available for detection is reduced as well. Hence, two crucial factors that affect the choice of the detection method for microfluidic devices are sensitivity and scalability to smaller dimensions.

Optical techniques can fulfil these requirements and a growing research has been devoted, in the past years, to couple optical components to microfluidic devices, or to directly integrate them on LOCs.

Several techniques have been tested, with different advantages and disadvantages[71], including absorbance, fluorescence, chemiluminescence or refractive index measurements. Among these, fluorescence detection yields a large number of experimental examples, since it can benefit from superior sensitivity, being a background free technique, and extreme selectivity, exploiting chemical labelling of the analyte of interest.

A more traditional approach to detection employs benchtop optical instrumentation, which can reach elevate sensitivity. However, the compactness advantages of LOCs risk to be frustrated by the need of such massive devices for actually performing the measurements. Furthermore, careful alignment is needed between the chip and the external instrumentation.

For these reasons, a key element for the success of the LOC concept will be the ability to successfully integrate on-chip also the optical detection schemes, enabling a significant reduction in size, costs and overall complexity of the system. In particular, the use of optical waveguides has many clear advantages with

¹When filled by electrolytic solutions, the microchannel walls may acquire a surface charge. This surface charge attracts the ions in solution, which create a charged layer on the capillary walls. An electric field applied in the liquid will force this charged layer to translate, dragging the liquid with it in a laminar flow, called electroosmotic flow.

respect to standard free-space detection systems, in terms of alignment precision, compactness and portability.

Integration of optical waveguides and microchannels onto the same substrate has been demonstrated using silicon-based photolithographic technologies[72, 73]. This anyway increases costs and complexity of the LOCs fabrication process, since several photolithographic steps need to be added. Polymer technology is more cost-effective: liquid core waveguides and microchannels have been demonstrated in a single soft-lithography step[74]. Anyway, the optical waveguide quality is typically lower.

Femtosecond laser micromachining is indeed a powerful tool for this kind of applications, since it allows to directly fabricate both fluidic channels and high quality waveguides in fused silica substrate[75]. A single irradiation step is sufficient to fabricate fully three-dimensional photonic structures and microchannels, with intrinsic reciprocal alignment. Furthermore, femtosecond laser pulses enable the fabrication of waveguides, by simple post-processing, in commercial LOCs[76]. In this way the integration of photonic functionalities can be achieved without affecting the lithographic fabrication process of the fluidic chip.

1.2.1.3 Label-free sensing with integrated interferometers

Despite its excellent sensitivity, fluorescence may not be suited for applications in which the molecules cannot be labelled with fluorophores and should be detected in their natural form. Several approaches have been reported[77], involving refractive index sensing by surface plasmon resonance, interferometers, single waveguides, fiber gratings, ring resonators, and photonic crystals.

In the following, we will concentrate on integrated MZIs, to give a more focused background to the experimental work presented in Chapter 3 of this thesis.

The vast majority of waveguide MZI devices reported in literature interacts with the measurand by evanescent field. The waveguide of the sensing arm presents a region interfaced with the liquid to sense, and the evanescent tails of the guided mode spread for a small depth in the liquid. The external surface is treated, by depositing some biorecognition molecules (e.g. antibodies), in order to achieve chemical selectivity. The target molecule, when present in solution, binds to this deposited layer, thus increasing the effective refractive index seen by the propagating waveguide mode.

The first example of a MZI adopting integrated waveguides with sensitized surfaces for biomolecules detection was reported by Heidemann et al. in 1993[78]. The authors created a MZI using silicon planar waveguide technology. An antibody for human chorionic gonadotropin (hCG) was adsorbed onto the waveguide external surface and hCG was specifically detected in concentrations down to 50 pM, equivalent to a refractive index detection limit of 5×10^{-6} . In this, as in other early experiments that adopted planar waveguides, beam dividers and combiners at the input/output of the MZI consisted of external bulk beam splitters. This required the chip to be mounted in an interferometrically stable optical setup.

Channel waveguide technology allows a completely integrated design, in which

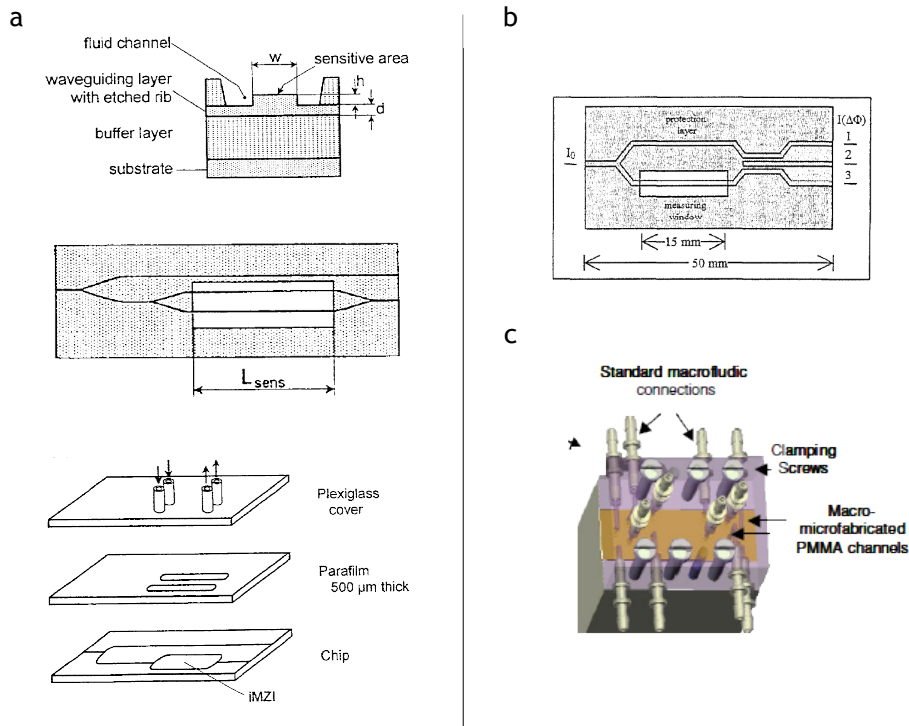


Figure 1.6: (a) Integrated MZI biosensor by Weisser et al.[79] (top) cross-section of the guiding structure with integrated fluidic channel (middle) waveguide chip layout (bottom) schematic of the final assembly of the chip (b) Schematic of the MZI realized by Drapp et al.[80]: the output beam combiner is a 3×3 coupler. (c) 3D picture of the integrated optical-microfluidic chip reported by Blanco et al.[81], enclosed in a robust PMMA housing with fluidic connections: it can operate with six independent microchannels on the top of the MZI devices on a single chip.

beam dividers and combiners are Y-junctions. For example, Weisser et al. showed an integrated MZI[79] (Figure 1.6a), realized by silicon oxynitride ridge waveguides. The waveguides are buried under a silica cladding layer, except for a sensing window which leaves uncovered parts of both the sensing and the reference arm waveguides. A microfluidic system is built above the chip, using a parafilm layer with the microfluidic channels pattern and a Plexiglas covering. Only the surface above the sensing arm is functionalized, but both arms get in contact with the liquid: this enables to cancel out common mode noise terms, such as temperature modulations, bulk liquid refractive index changes and non-specific adsorption. A limit of detection of streptavidine covering of $20 \text{ pg}/\text{mm}^2$ was claimed.

One drawback of the MZI structure is the loss in sensitivity when the working point is at a maximum or at a minimum of the interference fringe. Heideman and Lambeck[82] demonstrated a MZI, built by SiON waveguides, which integrates an electrooptic phase modulator. A properly designed AC signal, applied to the phase modulator, allows to find the quadrature points of the MZI response and

to retrieve in this way the refractive index. A refractive index detection limit of 10^{-7} was reported.

An innovative MZI design was proposed, for solving the same problem, by Drapp et al.[80] (Figure 1.6b). In their device, the light coming from the two arms is not recombined on a Y-junction, but on a 3×3 directional coupler. This coupler is designed to give interference with a $2\pi/3$ phase shift between different outputs. Thus, unambiguous detection of small phase changes can be achieved from the simultaneous observation of the three outputs. Employing this device for immunoassay of the herbicide symazine, a detection limit of 0.1 ppb was demonstrated.

An integrated MZI was also reported by Prieto et al.[83], with waveguides fabricated by the ARROW technology, which allows to enhance field penetration beyond the waveguide surfaces and thus increases the surface sensitivity.

Advancements towards the integration with microfluidics were shown by Blanco et al.[81] (Figure 1.6c). A three-dimensional network of microfluidic channels is built on the top of a silicon wafer in which a Mach-Zehnder interferometric sensor has been already fabricated. The fluidic part is realized by CMOS compatible SU-8 multilevel polymer technology and is effectively connected with tubing which precisely delivers the sample to the sensing area. A PMMA housing ensures robust leakage-free flow operation of the device. A bulk refractive index detection limit of 3.81×10^{-6} was obtained.

Whereas all these examples are based on evanescent field sensing, some interferometric configurations that allow to sense directly the volume were reported by Dumais et al.[73]. In their work, many refractive index sensors are presented, all based on self-forming microchannels in borophosphosilicate glass, monolithically integrated with silica waveguides. The microchannels have a typical diameter of $2 \div 3.5 \mu\text{m}$ and possess optical waveguiding properties when filled with liquid. In particular, a MZI is demonstrated, with the sensing arm partially constituted by a microchannel, which acts as a liquid core waveguide. This approach considerably increases the sensitivity of the device to the refractive index of the liquid medium, with respect to an evanescent field configuration, for the same interaction length.

1.2.2 Sensing by quantum light

1.2.2.1 Quantum limits to sensitivity

Quantum mechanics places precise limits to the accuracy that can be reached by an experimental measurement. The Heisenberg uncertainty principle imposes an intrinsic indetermination on complementary physical observables. Furthermore, the achievable measurement precision depends on the measurement system[84] and scales with the resources employed.

Classical laser interferometry measurements, the ones considered throughout the whole Section 1.2.1, make use of coherent light states. In coherent states the photon statistics follows a poissonian distribution and the ultimate limit to precision is given by the commonly called *shot* noise. This poissonian noise gives an uncertainty in the phase estimation $\Delta\phi_c = 1/\sqrt{N}$, where N is the number

of photons employed. This classical sensitivity limit is named *standard quantum limit*.

Increasing N is usually possible, by increasing the laser power at will. However, in some applications the practical limits of laser power are reached and the integration time cannot be increased without reducing the bandwidth of measurement below that required. This is the case of gravity wave interferometers[85]. In other scenarios, one could deal with samples which are very sensitive to light; thus, one would like to minimize the total number of photons employed for achieving the required precision. This could be the case of particularly photosensitive biological samples.

In these cases, quantum states of light with subpoissonian statistics can be used to beat the noise limitations of classical measurements and push the sensitivity towards the ultimate physical limits. Squeezed light states (currently used for the above mentioned gravity wave interferometry) allows to lower the phase estimation uncertainty to $\Delta\phi_s = 1/N^{\frac{3}{4}}$ in certain conditions. The use of Fock states² or specific entangled states enables to reach $\Delta\phi_H = 1/N$. This is indeed the lowest value of uncertainty allowed by the law of physics and is referred to as the Heisenberg limit.

1.2.2.2 Interferometry with N00N states

Particularly interesting non-classical states of light that enable to approach the Heisenberg limit, are the N00N states. These are defined as follows:

$$|N00N\rangle = \frac{|N0\rangle + |0N\rangle}{\sqrt{2}} \quad (1.1)$$

Note that this state involves two optical modes and the N photons can be found always in only one of the two modes: the uncertainty is on which of the two.

Introducing a sample in one optical mode, which would produce a phase shift ϕ on a single photon, in this case produces a $N\phi$ dephasing on one term of the entangled state:

$$\frac{|N0\rangle + e^{N\phi}|0N\rangle}{\sqrt{2}} \quad (1.2)$$

If a suitable detection scheme is adopted, an interference fringe with a period N times shorter than the classical one is observed. In case of unitary fringe visibility and perfect measurement efficiency (no photon losses or detector inefficiencies), a phase uncertainty of $\Delta\phi_{N00N} = 1/N$ can be reached, for a single measurement with a N photon N00N state. If the measurement is repeated k times the uncertainty will scale according to the usual laws of statistics: $\Delta\phi_k = 1/(\sqrt{k}N)$.

It has been demonstrated that observation of λ/N interference fringes, i.e. fringes with N -fold periodicity, which is called *super resolution*, can be performed also using purely classical resources[86]. Anyway it can be also shown that in this case no reduction in the phase uncertainty is gained.

An effective enhancement in sensitivity (*super sensitivity*) is, on the contrary, a purely quantum feature. However, non-optimum detection schemes which lower

²States of light with a determined number of photons (see Appendix A).

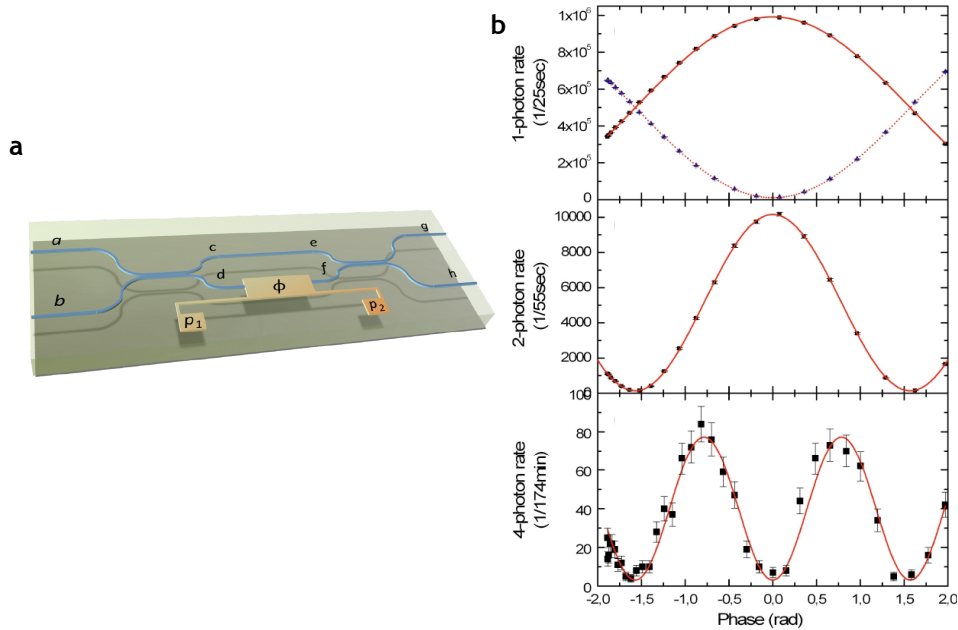


Figure 1.7: (a) Picture of the integrated waveguide MZI by Matthews et al. [91]. Metal electrodes are deposited on the top of the silica-on-silicon wafer, to provide thermo-optical phase control. (b) Experimental one-photon, two-photon and four-photon interference fringe, observed in the same device varying the phase accumulated in one arm of the Mach-Zehnder.

the fringe visibility, as well as losses and other inefficiencies which prevent photons to be detected, increase the experimental value of $\Delta\phi$ [87], making it hard to actually achieve the Heisenberg limit.

Up to now, several experiments of interferometry with $N00N$ states have been reported [88, 89, 90]. With proper detection schemes, λ/N interference fringes have been observed, even though inefficiencies of the present single-photon detectors prevent a real experimental super-sensitivity. In addition, measurements have been always performed on waveplates or phase shifters with known phase contribution. No experiments have been reported on samples from the “real world”, such as biological samples.

Interferometry with $N00N$ states with $N = 2$ and $N = 4$ has been demonstrated also in an integrated circuit architecture by Matthews et al. [91] (Figure 1.7). A waveguide MZI, consisting of two balanced directional couplers and a thermal phase shifter on one arm, was fabricated by the silica-on-silicon technology. In this kind of device (see also Section 3.2.1) a two-photon $N00N$ state is generated deterministically by injecting two indistinguishable photons in the two input ports, while four-photon $N00N$ states are generated non deterministically by injecting four indistinguishable photons, two in each input port. Varying the phase shift on one arm of the MZI, two-photons and four-photons interference fringes were observed with visibilities as high as 97% and 92%, respectively.

1.3 Integrated quantum computing and optical simulation

1.3.1 Optical chips for quantum computing

1.3.1.1 Quantum information with linear optics

Quantum information concepts and ideas have opened in the recent years new exciting perspectives in communication, computing and measurement sciences. In this framework, the unique properties of quantum mechanics could provide for example unprecedented security to cryptography, as well as exponential speedup in computing and simulation of complex quantum systems.

This whole revolution is based on encoding information in qubits, i.e. two level quantum systems. Whereas the classical bits are encoded on macroscopic systems, which can exist on two well defined states “0” or “1”, qubits can exist in a superposition of levels $|0\rangle$ and $|1\rangle$, according to the general expression:

$$|\psi\rangle = \cos\theta|0\rangle + e^{i\phi}\sin\theta|1\rangle \quad (1.3)$$

Two or more qubits can also be entangled together, giving rise to a wide spectrum of non classical properties.

Several approaches are being pursued by current research for implementing quantum qubits and develop a quantum computer. These approaches exploit different physical systems[92] such as photons, trapped atoms or ions, superconducting circuits or quantum dots.

Compared to other physical systems, photons manifest extremely low decoherence: this makes them ideal candidates for data transmission and metrology. Photonic qubits can be encoded in different degrees of freedom, such as polarization (which is perhaps the most used), linear momentum (also called path encoding) and orbital angular momentum.

Photons, anyway, hardly interact with each other. Extremely high optical nonlinearities would be required to be efficient at the single photon level. Hence, building quantum logic gates in which two qubits have to interact had appeared for many years a dramatically hard task.

Knill, Laflamme and Milburn in 2001 discovered[93] that universal quantum computation can be achieved using only linear optics, single photon sources and single photon detectors. In their scheme, optical nonlinearities are simulated by a clever exploitation of quantum interference (see Appendix A) and ancillary photons.

1.3.1.2 Linear-optics quantum CNOT gate

In the linear optics architecture mentioned above, quantum logic gates may be non-deterministic. This means that when two (or more) photonic qubits enter a logic gate, they will be correctly elaborated with a certain probability, but they will produce an inconsistent outcome in the other cases. Anyway, the correct output state will be *heralded* by some condition, e.g. the outcome will be correct if and only if the two qubits will exit the device from distinct ports.

One of the most significant examples of quantum gate is the CNOT (Controlled-NOT) gate; in fact, this two-qubit operation, together to one-qubit rotations, can provide universal quantum computation. Due to its importance, several experimental implementations of this gate have been demonstrated in the literature.

The CNOT gate flips the state of the target (T) qubit depending on the value of the control (C) qubit, according to the following truth table:

Input		Output	
C	T	C	T
0	0	0	0
0	1	0	1
1	0	1	1
1	1	1	0

It is worth stressing the fact that the truth table above would define also a classical logical gate. What characterizes the *quantum* logic gate is the possibility to work with superposition states of “0” or “1” or even entangled states. More specifically, the operation of a quantum gate may be expressed by a unitary (and reversible) transformation of the quantum state, which for a CNOT is described by the following operator:

$$U_{\text{CNOT}} = |00\rangle\langle 00| + |01\rangle\langle 01| + |11\rangle\langle 10| + |10\rangle\langle 11| \quad (1.4)$$

The first experimental demonstration of a photonic non-deterministic CNOT gate was reported by O’Brien et al.[94], implementing the scheme of Figure 1.8a by the use of calcite birefringent beam displacers and waveplates. Correct operation is heralded by the coincidence detection of two photons in two different output modes.

In general, four optical modes are needed for encoding two qubits. They can be four different spatial optical modes with the same polarization (in the case of path encoding), or two spatial modes with two different polarizations (in the case of polarization encoding). In the scheme used by O’Brien et al. the gate works for path-encoded qubits; anyway the qubits are generated in the polarization encoding, since it is in this encoding that the source adopted can produce two-qubits entangled states. Conversion from polarization to path encoding and vice versa is performed at the input and output of the gate by using polarization beam splitters and waveplates (see inset of Figure 1.8a).

Note that this CNOT scheme exploits both quantum and classical interference; thus, a phase stable optical circuit is required. Later, a different scheme of CNOT gate (see Figure 1.8b) was demonstrated[95, 96, 97], making use of partially-polarizing beam splitters and not relying on classical interference effects, hence being less demanding in terms of stability. It is actually a non deterministic C-phase gate: a device which inverts the phase of the target qubit depending on the value of the control qubit. Correct operation is heralded by coincidence detection. For polarization encoded qubits (e.g. $|H\rangle \equiv |0\rangle$ and $|V\rangle \equiv |1\rangle$), a C-phase gate acts with the following unitary transformation:

$$U_{\text{C-phase}} = |HH\rangle\langle HH| + |HV\rangle\langle HV| + |VH\rangle\langle VH| - |VV\rangle\langle VV| \quad (1.5)$$

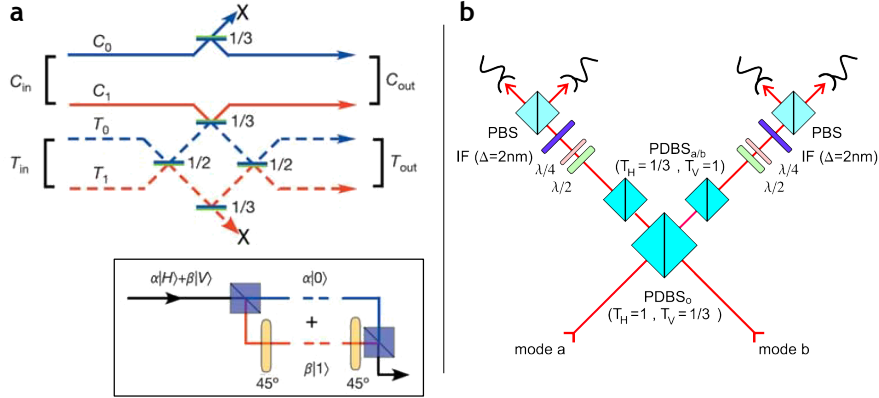


Figure 1.8: (a) Scheme of the first photonic CNOT gate experimentally demonstrated[94]. It operates on path-encoded qubits: the control qubit is encoded on the modes C_0 and C_1 ; the target qubit is encoded on the modes T_0 and T_1 . Conversion between path encoding and polarization encoding is achieved by a polarizing beam splitter and a half-wave plate at 45° (see inset). (b) CNOT gate without path interference, operating on polarization encoded qubits, based on three polarization dependent beam splitters (PDBS).[96]

It can be noticed that, using different encoding bases for the control (C) and target (T) qubits, namely:

$$\begin{aligned}
 |0\rangle_C &\leftrightarrow |H\rangle & |0\rangle_T &\leftrightarrow \frac{|H\rangle + |V\rangle}{\sqrt{2}} \\
 |1\rangle_C &\leftrightarrow |V\rangle & |1\rangle_T &\leftrightarrow \frac{|H\rangle - |V\rangle}{\sqrt{2}}
 \end{aligned} \tag{1.6}$$

the action of the operator of Eq. (1.5) becomes identical to the CNOT operator of Eq. (1.4). Such basis transformations are easily performed by waveplates.

1.3.1.3 Integrated quantum photonics

Quantum computation by linear optics has shown to be conceptually feasible[93] and proof-of-principle quantum gates built of bulk optical components have been demonstrated. However, the realization of complex quantum optical schemes is extremely challenging, since the bulk optics approach suffers from severe drawbacks regarding stability, precision and size. Phase stability requirements are particularly demanding when advanced interferometric structures have to be implemented. Hence, applications outside laboratories with controlled temperature and vibrations appear clearly out of reach.

In their pioneering work, Politi et al.[98, 99] demonstrated an innovative approach for realizing quantum optical circuits which employs integrated waveguides, realized by the silica-on-silicon technology. These waveguides are fabricated by well-established photolithographic processes, developed for the telecommunication industry. They yield low propagation losses and good mode-matching with single-mode optical fibers. High visibility Hong-Ou-Mandel[100] interference dips were shown in directional couplers, which play the role of bulk beam-

splitters, demonstrating high-quality quantum interference. An integrated CNOT gate for path encoded qubits was reported, exploiting the inherent stability of waveguide interferometric structures. In addition, integrated resistive heaters enabled dynamic phase control of MZIs and on-chip preparation and manipulation of entangled two photon states[91].

Hong-Ou-Mandel interference with two and three photons was demonstrated also in directional couplers fabricated in fused silica by femtosecond laser waveguide writing[101].

In all these experiments, however, photons were employed with fixed polarization states and qubits were path encoded. No integrated circuits have been demonstrated yet for polarization encoded qubits[99], which is indeed the most common approach for implementing quantum information protocols with entangled photons.

1.3.2 Optical quantum simulation

1.3.2.1 Quantum simulation and quantum walk

Simulating quantum physical systems using classical computers is a computationally hard task, as Feynman early pointed out[102]. In fact, the non-local probabilistic description of reality, characterizing the quantum physics approach, requires resources which grow exponentially with the system dimension, when simulation is performed by deterministic locally-interacting machines.

Random walk studies the trajectory of a particle which moves in the space with random steps. This has proven to be a powerful model for the simulation of classical stochastic processes with applications ranging from physics to biology or economy. Efficient algorithms based on random walk have been also developed in computer science for solving partial differential equations or searching a database.

The description of a classical random walk is fairly simple in one dimension, i.e. when a particle can move on an isotropic one dimensional lattice. If the particle is on one lattice site, it will have the same probability to hop to the site at its left or to the site at its right. Its trajectory will evolve in a probabilistic way: after many steps, the probability to find the particle on a certain site will tend to a gaussian distribution (for the central limit theorem).

This concept of random walk assumes the walking particle to be classical, i.e. completely described by its position on the walk. If a particle with quantum properties undergoes an analogous walk this description is insufficient, since the particle is characterized by a complex wavefunction. At each step, it is no longer correct to say that the particle *hops* to one of the two possible positions: the wavefunction *spreads* towards both the adjacent sites. In subsequent steps interference effects arise, displaying a highly non-classical behaviour, hard to simulate with classical resources.

The potentials of this quantum counterpart of the random walk, the *quantum random walk*, have been explored for almost two decades[103, 104], attracting much attention in the scientific community. A quantum walk model has been recently proposed for certain biophysical processes, such as energy transfer in photosynthesis [105]. Algorithms based on quantum walks have been theoretically investigated, which would enable exponential speedup in solving certain

computational problems[106, 107]. Quantum walks can also provide a framework for achieving universal quantum computation[108].

1.3.2.2 Discrete time quantum walk

Two different kinds of quantum random walk may be considered[104]: discrete and continuous time. In the former, the wavefunction evolution happens at discrete time instants, while in the latter the evolution is governed by a continuous time hamiltonian.

It is worth reviewing some basic concepts of the discrete time quantum walk on a one dimensional lattice. In a discrete quantum walk the particle state is described not only by the spatial position $|j\rangle$, i.e. its spatial wavefunction, but also by an additional degree of freedom spanning a two-dimensional space, named the *quantum coin*. At any given time the particle may be in a superposition of the two basis states, referred as up ($|U\rangle$) or down ($|D\rangle$) and representing the two “coin faces”. The quantum coin state directs the motion of the particle and the stochastic evolution by a unitary process. In fact, the dynamics of the discrete quantum walk is given by the following rules:

1. at each step the quantum coin state is changed by a “coin tossing” represented by a 2×2 unitary operator C . Note that, with respect to the classical “tossing” of a coin, this does not have a deterministic result: no measurement is taken and the wavefunction of the coin space does not collapse. The quantum coin just changes its general superposition state.
2. an evolution operator E is subsequently applied, which makes the particle shift to the higher or lower position, depending on the quantum coin state.

$$E = \sum_j |j-1\rangle\langle j| \otimes |U\rangle\langle U| + |j+1\rangle\langle j| \otimes |D\rangle\langle D| \quad (1.7)$$

If the particle has an initial state $|\psi_0\rangle = |j_0\rangle \otimes (\alpha_0|U\rangle + \beta_0|D\rangle)$ after N steps the particle state will be:

$$|\psi_N\rangle = (EC)^N |\psi_0\rangle \quad (1.8)$$

The coherent action of the two operators leads to entanglement between the position and the internal degree of freedom.

1.3.2.3 Photonic realizations of quantum walk

Several experimental implementations of single particle quantum walk have been demonstrated, exploiting different physical systems, such as photons, trapped atoms[109], ions[110, 111] and energy levels in NMR schemes[112].

Focusing on photonic quantum walks, different experimental approaches have been reported.

A chain of beam displacers (Figure 1.9a) has been used to observe discrete quantum walk of single photons[113]. Slight misalignments of the displacers provided tunable decoherence.

Discrete time quantum walk of single photons has been reported in a fiber loop configuration (Figure 1.9b). The position on the walk is encoded in the time

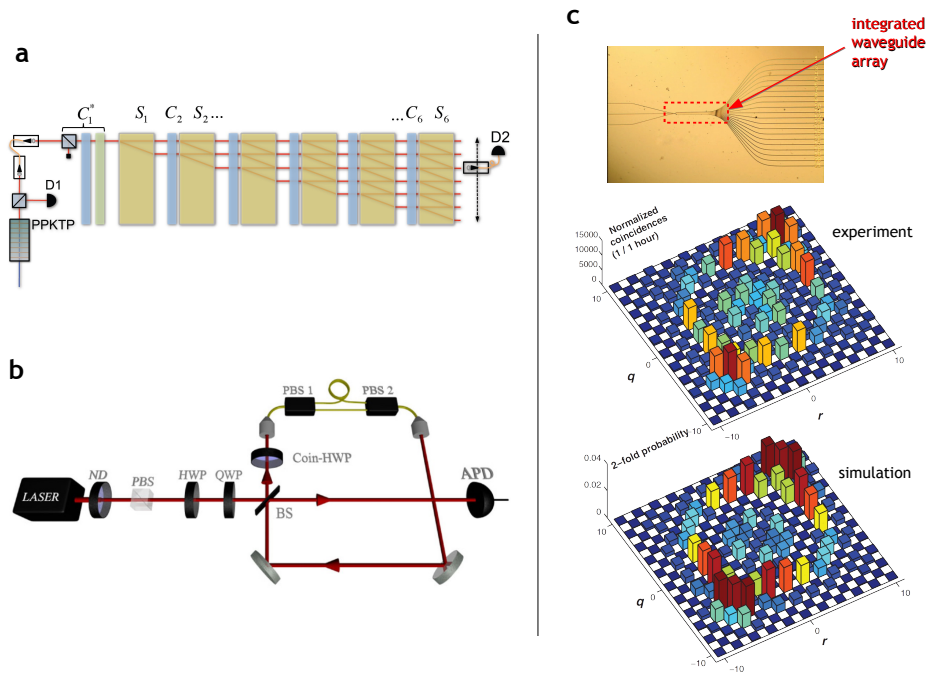


Figure 1.9: (a) Discrete time photonic quantum walk with bulk calcite beam displacers[113]. (b) Fiber loop setup for single photon discrete quantum walk[114]. (c) Continuous quantum walk of two correlated photons in a waveguide array[115]. (top) Photographic image of the integrated chip. The red square shows the actual waveguide array region. On its right and left approaching and departing waveguides allow for fiber coupling. (middle) Experimental and (bottom) simulated two-photon correlation when injecting two photons in neighbouring waveguides.

delay while the coin is encoded in the polarization of the photons. A polarizing beam splitter deviates with a certain probability the photon in a shorter or in a longer path, which is equivalent to hop a step back or a step forward in the time delay scale. A half wave plate before this polarizing beam splitter allows to adjust the coin flip operation[114]. Substituting the half wave plate by a fast switching Pockels cell [116] a dynamic variation of the coin operation was implemented, allowing to observe disorder effects as well as Anderson localization.

Photonic continuous time quantum walk was demonstrated by simply injecting coherent light in an integrated waveguide array[117]. In fact, the hamiltonian of a continuous time quantum walk shows analogies with the coupled mode equations governing the light propagation in such structure; furthermore, the interference effects of single photons are the same observed with coherent light.

Very recently, Peruzzo et al. carried out the first experimental investigation on the quantum walk of two correlated particles[115], by injecting two-photon states in a waveguide array and measuring two-photon correlations at the output (Figure 1.9c). This result is noteworthy since employing multiple particles enables an exponential increase of the computational power: for example quantum walk of two particles on a line is equivalent to a single-particle walk on a two dimensional square lattice.

Continuous quantum walk of two particles has later been shown also in a three-dimensional elliptical waveguide array[118].

1.3.3 Simulation of quantum phenomena by classical resources

As already mentioned in Section 1.1.3.4, formal analogies exist between electromagnetism equations describing light propagation in photonic structures and equations employed in several other fields of physics, in particular quantum mechanics. In fact, quantum mechanics itself, since its beginnings, brought the physics of waves into mechanics of material particles.

Accessing coherent phenomena of microscopic quantum systems often poses serious experimental challenges, due to the presence of many-body interactions, decoherence, fast time-scales. Engineered photonic structures, developed exploiting the formal analogy between optical propagation and microscopic phenomena, can therefore provide a unique laboratory tool to directly visualize dynamics otherwise difficult to observe experimentally.

The number of quantum-optical analogies which have been investigated in the recent years is incredibly wide[119]. A vast class of these analogies is based on the similarity between the scalar wave equation describing the spatial propagation of a monochromatic light beam in a dielectric structure and the temporal Schroedinger's equation for a quantum particle in a binding potential, possibly driven by external electric field. In fact, the propagation of a monochromatic linearly polarized wave of frequency ω , in a dielectric medium with refractive index distribution $n(x, y, z)$, can be described by the Helmholtz equation (for the scalar electric field E):

$$\nabla^2 E + \frac{\omega^2}{c^2} n^2(x, y, z) E = 0 \quad (1.9)$$

If the variations in the index distribution along the propagation direction z have a spatial scale much larger than the wavelength λ one can assume for the electric field a form $E = E_0(x, y, z) e^{-j(2\pi n_{\text{eff}}/\lambda)z}$, where n_{eff} is the effective index of the guided mode, and E_0 is an electric field profile slowly varying along z . Under these hypotheses one can rewrite (1.9) as:

$$i\lambda \frac{\partial E}{\partial z} = -\frac{\lambda^2}{2n_{\text{eff}}} \nabla_{x,y}^2 E + V(x, y, z) E \quad (1.10)$$

with $\lambda = \lambda/2\pi$ and $V = (n_{\text{eff}} - n(x, y, z))/2n_{\text{eff}}$.

Equation (1.10) is clearly similar to the two dimensional Schroedinger's equation³ for a particle of mass n_{eff} in a (binding) potential V , where the temporal coordinate is substituted by z and the reduced Planck constant \hbar is substituted by the reduced wavelength λ .

It is worth noting that the temporal coordinate is now mapped to the z propagation direction; hence, it is possible to easily visualize in space phenomena

³Schroedinger's equation for a particle of mass m in a two dimensional space (x,y) :

$$i\hbar \frac{\partial \Psi}{\partial t} = -\frac{\hbar^2}{2m} \nabla_{x,y}^2 \Psi + V(x, y, t) \Psi$$

which are typically ultrafast in time. In addition, variations of the refractive index distributions along the z direction are equivalent to variations of the potential V in time, i.e. action of external time-varying forces. In particular, this allows to mimic coherent laser-matter interactions just by simple bending or twisting of the waveguiding structures.

For example, the discrete periodic structure of a waveguide array, within this analogy, constitutes the periodic potential of a crystalline lattice. Several phenomena can be observed: from Bloch oscillations and Zener tunneling in presence of a constant external field[120, 63], to dynamic localization in presence of an oscillating field [121, 62].

Light propagation in a waveguide array can be described also in terms of coupled mode equations. Considering the simple case of a one-dimensional array of waveguides with nearest neighbours interactions, the complex amplitudes c_n of the different modes evolves during the propagation along z according to:

$$i \frac{dc_n}{dz} = \kappa_n c_{n+1} + \kappa_{n-1} c_{n-1} + \beta_n c_n \quad (1.11)$$

where κ_n is the coupling coefficient between the n -th and the $(n+1)$ -th waveguide and β_n is the propagation constant of the n -th mode. When describing a dynamic situation, both κ_n and β_n can be modulated along z . Hence, quantum-optical analogies based on Eq. (1.10) can often be rewritten in terms of Eq. (1.11) (modified, if necessary, to consider second-neighbour interactions or two-dimensional arrays). In addition, the latter equation enables another class of analogies, based on a description of a quantum mechanical problem in terms of coupled modes/levels. The temporal coordinate is substituted again by the z spatial coordinate, while the waveguide occupation c_n can be equivalent to occupation of more general states, such as energy levels.

For example, three waveguides can play the role of three atomic energy levels. Modulated coupling coefficients between them (provided by modulated inter-waveguide distances) are equivalent to dynamic coupling of the levels by external coherent field interactions (i.e. laser pulses). Within such scheme, the atomic STIRAP (STImulated Raman Adiabatic Passage) can be simulated[122] (see Figure 1.10a). This consists of the complete population transfer from the first level (waveguide) to the third level (waveguide), without populating the second one, achieved by a counterintuitive interaction scheme i.e. switching on the interaction between the second and the third levels before the one between the first and the second levels.

Another, more complex case, is that of a one-dimensional waveguide lattice in which the coupling coefficients are constant along z but scale with the waveguide number according to a square root law, i.e. in Eq. (1.11) one has $\kappa_n = g\sqrt{n+1}$. It has been demonstrated[123] that, in such array, waveguides can represent different Fock states and light propagation along z , due to this engineered coupling, is equivalent to continuous application of the Glauber displacement operator. Starting from the vacuum state ($|0\rangle$), application of the displacement operator generates a coherent field with increasing average photon number. Since coherent states, projected on the Fock basis, are characterized by a poissonian distribution of the photon numbers, in the optical analogue this corresponds to an intensity distribution in the waveguides which is poissonian, with

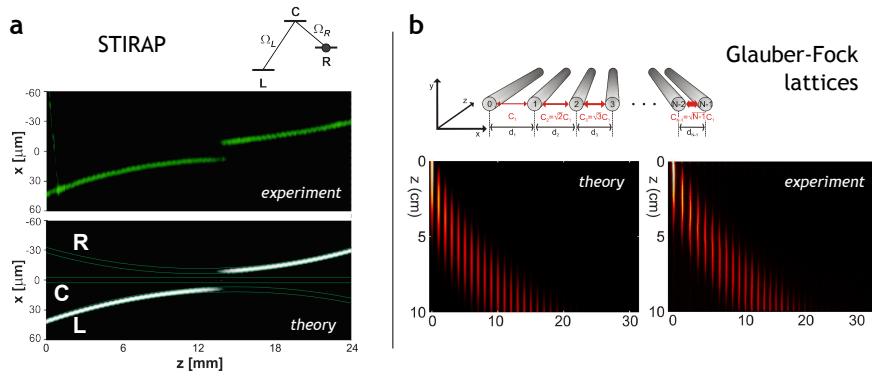


Figure 1.10: (a) (top) Scheme of the atomic STIRAP, involving three energy levels: L, C, R. (bottom) Experimental and theoretical light distribution along propagation in a three-waveguide system, in which each waveguide represent an atomic level[122]. The interaction between the levels is enabled bringing two waveguide closer: the counterintuitive interaction scheme allows a complete population transfer from L to R without populating C. (b) (top) Schematic of the waveguide structure used to simulate the action of the Glauber displacement operator in the Fock space[124]. (bottom) Theoretical and experimental light distribution pattern along the waveguide array.

an average waveguide number increasing with propagation. An experimental realization of such Glauber-Fock photonic lattices has been recently reported[124] (see Figure 1.10b).

Chapter 2

Experimental

The experimental techniques adopted in the work of this thesis are described in this Chapter. In particular, focus is given to the femtosecond laser waveguide writing setup (Section 2.1), together with the techniques and instrumentation for the characterization of waveguide devices (Section 2.2) and for the permanent coupling with optical fibers (Section 2.3)

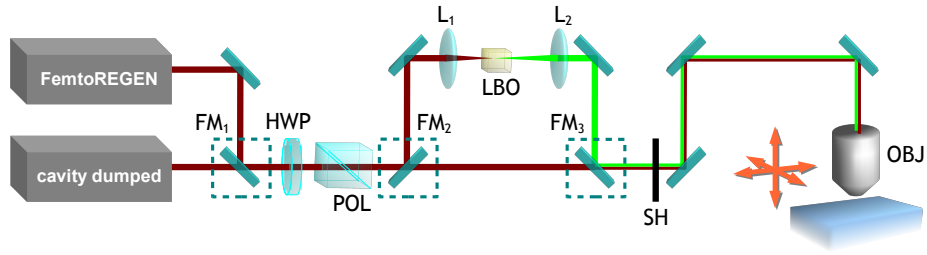


Figure 2.1: Waveguide writing setup. Two femtosecond laser systems (a cavity dumped oscillator and a HighQLaser FemtoREGEN) are available through a flip mirror (FM_1) that switches between the two sources. Attenuation to obtain the desired writing power is performed by a half-wave plate (HWP) and a Glan-Thomson polarizer (POL). A second harmonic generation stage can be inserted in line through the flip mirrors FM_2 and FM_3 . For the second harmonic generation laser light is focused by a 15 cm focal length lens (L_1) onto a lithium triborate crystal (LBO), properly heated to reach the non-critical phase-matching condition; the beam is then recollimated by a 30 cm focal length lens (L_2), thus enlarging the beam diameter to completely fill the objective aperture. A mechanical shutter (SH) blocks or enables the beam in the machining area. The beam is focused into the substrate by a microscope objective (OBJ). Three-dimensional translation of the sample is enabled by computer-controlled high-precision stages (see text).

2.1 Waveguide writing setup

The waveguide writing instrumentation used for the experimental work of this thesis is shown in Figure 2.1.

Two Yb-based femtosecond laser sources are available: one is a cavity-dumped mode-locked oscillator[125] developed in a collaboration between the Max Planck Institut of Heidelberg (Germany) and HighQLaser GmbH (Austria); the other is a commercial amplified system from HighQLaser GmbH.

A reconfigurable system of mirrors allows to steer either of the two laser beams in the machining zone or to direct the beam through a second harmonic generation stage, to change the laser writing wavelength. A shorter wavelength may be useful in high-bandgap substrate (e.g. fused silica) to enhance nonlinear absorption. Several objectives are available to focus the writing beam, with numerical apertures ranging from 0.3 to 1.4 (oil immersion). A cylindrical telescope for beam shaping can be optionally inserted before the objective. Sample translation is provided by high-precision three-axis stages.

A mechanical shutter (Thorlabs SH05), synchronized with the motion stages, is also adopted for enabling or blocking the laser beam in specific regions.

2.1.1 Cavity dumped oscillator

The active medium of this laser system[125] is a $KY(WO_4)_2$ crystal, doped at 5% concentration with Ytterbium. Laser emission is at 1030 nm wavelength. Pumping is performed by a InGaAs multiemitter laser diode bar at 980 nm wavelength. The employed optical pump power is on the order of 15 W.

The laser cavity is folded by the use of several mirrors, which allow to fit the 8.9 m total length of the cavity in a footprint of about 90 cm \times 50 cm. A

SESAM (SEmiconductor Saturable Absorber Mirror) is adopted as end mirror of the cavity and assures the passive mode-locking regime. The mode-locking pulse train is at 17 MHz frequency.

Cavity dumping of the laser pulses is performed by a Pockels cell combined with a thin film polarizer. An external electronic driver is synchronized to the mode-locking pulse train and acts on the Pockels cell with adjustable voltage and repetition rate. Due to the polarization rotation induced by the Pockels cell (proportional to the applied voltage), part of the pulse energy is reflected by the thin film polarizer and extracted from the cavity. The repetition rate can be adjusted from a few kHz to 1.1 MHz, spanning the integer submultiples of 17 MHz.

It has to be noted that depending on the pump power and the dumping ratio, different pseudo-solitonic regimes are sustained, with different pulse energies and durations[126]. Hence, by acting on these two parameter one can finely tune the pulse duration from about 250 fs to about 400 fs and thus optimize also this pulse characteristic for the waveguide writing process. Also the output pulse energy clearly depends on these parameters and can typically be greater than 1 μJ .

2.1.2 HighQLaser FemtoREGEN

The FemtoREGEN¹ encloses in a very compact footprint a mode-locked oscillator (HighQLaser FemtoTRAIN), a regenerative amplifier and a pulse compressor, following the usual scheme of chirped pulse amplification. The oscillator is passively mode-locked through a SESAM and produces a 130 fs pulse train at 63 MHz and central wavelength of 1040 nm. Laser pulses from the oscillator can be amplified with repetition rates of 350 kHz, 500 kHz or 960 kHz, reaching respectively an energy of 24 μJ , 16 μJ or 8 μJ . A pulse picker is inserted inline before the compressor, so that effective repetition rates of the output pulses can be arbitrary submultiples of the ones reported above, down to 1 kHz. Output pulses after compression are about 420 fs long.

The whole laser system is turn-key and completely controlled by software; in particular the repetition rate can be changed with extreme flexibility, thus making this laser a powerful tool for exploring various regimes of waveguide writing.

2.1.3 Aerotech FiberGLIDE

Sample motion under the laser beam is enabled by Aerotech FIBERGLIDE 3D² three-axis motion stages. By combining air-bearing and non-contact brushless linear motors, very low friction between the moving parts is reached, guaranteeing elevated smoothness in the translation. The stages position is constantly monitored by optical encoders to 1 nm resolution, enabling an active control of the motion with errors below 100 nm.

The stages are computer controlled and programmable by G-code language (common in CNC machining) to perform complex design microfabrication.

¹<http://www.highq-us.com/en/products/regenerative-amplifiers/femto Regen-series/>

²<http://www.aerotech.com/products/photonics/fg3d.html>

2.2 Device characterization

Different characterization measurements are typically performed on the fabricated waveguides and devices, which will be briefly discussed in the following, together with the required instrumentation.

2.2.1 Observation with optical microscope

A first important characterization of the fabricated structures can be performed using an optical microscope. To this aim a Nikon ME600 microscope was used, equipped with an optional DIC (Differential Interference Contrast) module, which enables enhanced vision of small index contrasts by exploiting interference phenomena. A high resolution CCD camera (PixeLINK B871) is also mounted on the microscope.

Observation from the top allows to appreciate the uniformity of the written structures and allows to check for the absence of interruptions or evident defects. Lateral observation is useful to examine details of the cross-section of the waveguides.

2.2.2 Output mode characterization

In order to investigate the radiation confinement properties of the waveguiding structures a qualitative and quantitative characterization of the waveguide output mode is crucial.

Laser light at the desired wavelength is coupled into the waveguide using a fiber or an objective (see Figure 2.2a-b). In the first case, the extremity of a single mode optical fiber³ is brought close to the input facet of the waveguide. In the other case, the objective focuses the laser beam in order to have the beam waist coincident with the waveguide input; the numerical aperture of the objective employed should be of the same order of that of the waveguide (~ 0.10). In both cases the aim is to obtain the optimum overlap between the optical mode of the input light and the optical mode of the waveguide.

Precise and stable alignment of the fiber (or objective) with the sample is required. Hence, the fiber or the objective are mounted on a three-axis micropositioners (Melles Griot NanoMAX), with 50 nm resolution; the sample is hold by a four-axis manipulator (Melles Griot AMT), which allows two micrometric translations in the plane transverse to the optical axis and two tilt adjustments.

The end facet of the waveguide is imaged onto a high-sensitivity *vidicon* camera (Hamamatsu C2400-03A), by another objective ($\sim 0.5 \div 0.6NA$). This particular camera is sensitive to the whole visible range and to the near infrared up to 1800 nm wavelength, thus covering also the full telecom bandwidth. The numerical aperture of the objective employed for the imaging should be higher than the numerical aperture of the waveguide, in order to collect most of the output light and to achieve a convenient magnification ratio.

The intensity profile measured by the camera can be acquired for further elaboration. In particular, if the waveguide is monomodal (which is the case

³Properly cut, after removing the external plastic tubing and coating.

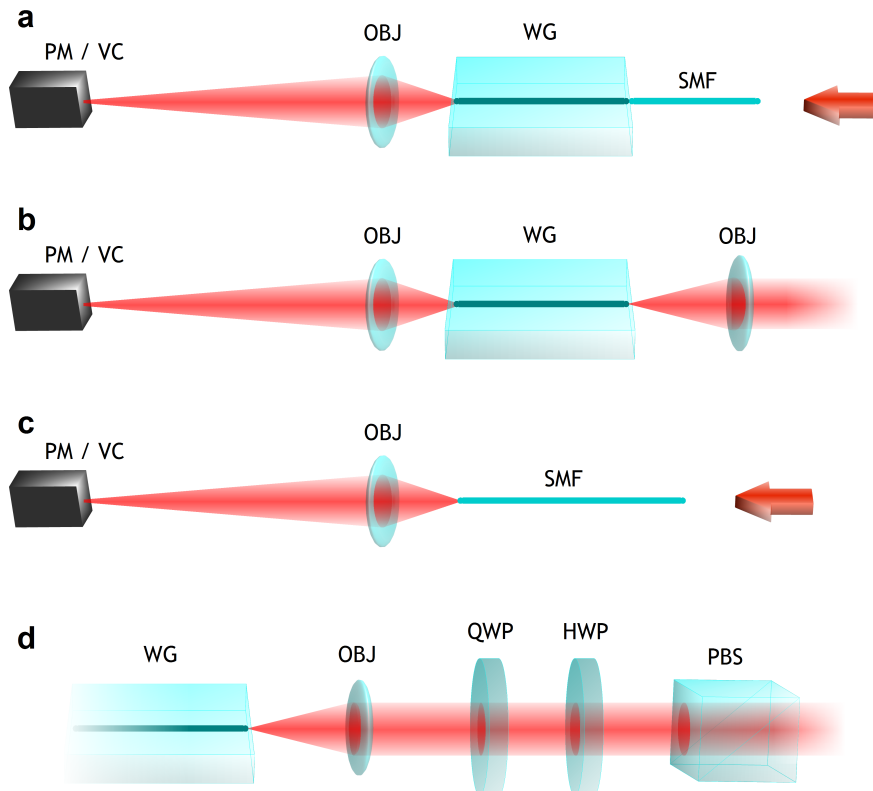


Figure 2.2: Principle schematic of the main configurations employed for waveguides characterization. **(a)** Laser light from a single mode fiber (SMF) is coupled to the waveguide (WG). An objective (OBJ) images the output facet of the waveguide onto a power meter head (PM), for measuring the transmitted power, or onto a videocamera (VC), for measuring the intensity profile of the guided mode. **(b)** A free-space laser beam is coupled to the waveguide through an objective; the collection setup is analogous to the previous case. **(c)** The waveguide is removed and the collection setup is used for measuring the power or the mode profile of a SMF. **(d)** A polarizing beam splitter (PBS), a half-wave plate (HWP) and a quarter-wave plate (QWP) are used to manipulate the polarization of the input light, in order to perform measurements of the polarization behaviour of the device.

of all the applications presented in this thesis), from the spatial intensity profile $I(x, y)$ one can retrieve the profile of the electric field $\vec{E}(x, y)$, given the formula:

$$\left| \vec{E}(x, y) \right| = C \sqrt{I(x, y)} \quad (2.1)$$

where C is a constant. Theory guarantees that the fundamental guided mode does not present sign inversions in the electric field profile, thus the calculation of the modulus is sufficient. Also the value of the constant C is not relevant, since one is interested to the normalized profile. Size calibration is performed acquiring the mode of a fiber with known dimensions (see Figure 2.2c).

2.2.3 Losses measurement

Insertion losses (IL) are defined as the total losses induced by the device, with respect to the case of absence of the device itself. They are typically expressed in decibels (dB). In order to measure the IL a setup similar to that described for acquiring the waveguide mode is adopted. In this case, a fiber is always adopted for launching light in the waveguide and the end-facet is not imaged on a camera but onto a power meter head (Figure 2.2a).

The output power from the device (P_{out}) and the output power from the fiber (P_{in}) are measured (using configurations of Figure 2.2a and Figure 2.2c respectively) and IL are calculated as:

$$IL = 10 \log_{10} \left(\frac{P_{out}}{P_{in}} \right) \quad (2.2)$$

In case of straight waveguides of length l , IL can be decomposed in the sum of different terms:

$$IL = CL + FL + PL \cdot l \quad (2.3)$$

with the following meaning for the addends:

- CL (Coupling Losses) are the losses due to the mode mismatch between the launch fiber and the waveguide and depend on the overlap integral between the two:

$$T_C = \frac{\left| \iint E_{wg} E_f dx dy \right|^2}{\iint |E_{wg}|^2 dx dy \cdot \iint |E_f|^2 dx dy} \quad (2.4)$$

$$CL = -10 \log_{10} T_C \quad (2.5)$$

The overlap integral T_C can be numerically evaluated once the field profile of the fiber and of the waveguide, respectively E_f and E_{wg} , have been acquired with the method previously described.

- FL (Fresnel Losses) originate from Fresnel reflections at the glass-air interface and assume the following expression, for a single interface:

$$FL_1 = -10 \log_{10} T_F = -10 \log_{10} \left[1 - \frac{(n_{glass} - n_{air})^2}{(n_{glass} + n_{air})^2} \right] \quad (2.6)$$

The insertion of the device involves adding two new glass-air interfaces, namely the input and output facets of the waveguide. For a single interface, being $n_{glass} \sim 1.45$, they are usually estimated as 0.18 dB. Hence, for the calculation of the total insertion losses, $FL \simeq 0.36$ dB. However, if index matching oil is used in fiber-waveguide coupling FL become negligible.

- PL (Propagation Losses) are the losses suffered per unit length of propagation in the waveguide. They are due to roughness and non-uniformity in the waveguide structure. In fact, theory predicts no propagation losses for a waveguide with perfect translational symmetry (i.e. uniformity) along the optical axis direction. They can be calculated from (2.3) once the other terms have been estimated.

2.2.4 Polarization behaviour characterization

When a specific polarization sensitivity or insensitivity of the fabricated devices is required (e.g. for the quantum optics applications described in Sections 4.1, 4.2 and 4.3), it becomes important to perform a characterization for different polarization states of light, for example by measuring how the power distributes over different output branches varying the input polarization.

In order to perform such measurements a polarizing beam splitter (PBS), a half wave plate (HWP) and quarter wave plate (QWP) are added before the launch objective, as shown in Figure 2.2d. For the rest, the setup is analogue to that of Figure 2.2b.

The laser source typically employed for this characterization is a 806 nm laser diode, since this is the wavelength required by the quantum optics experiments discussed in this thesis. Laser light passes through the PBS, which purifies the polarization to be exactly vertically oriented. The subsequent HWP and QWP allow to arbitrarily rotate the polarization state of the light, which is then injected into the waveguide by the objective.

It is worth highlighting the fact that fiber launch is not adopted in this case. In fact, common single mode optical fibers may introduce uncontrolled rotations of the polarization, even with minimum bending or mechanical stress of the fiber core.

2.2.5 Waveguide fluorescence observation

For the experiment described in Section 4.4, regarding quantum-optical analogies in photonic structures, it is required to measure how the light distributes in the structure during the propagation. To this aim, the fact, already mentioned in Section 1.1.3, that femtosecond laser written waveguides in fused silica present fluorescent colour centers, is exploited. These color centers emit at about 650 nm wavelength when excited with He:Ne laser light at 633 nm.

Imaging the fluorescence from above allows to quantitatively measure the light distribution in the waveguiding structures. The setup that we developed to perform such measurements is shown in Figure 2.3.

Light at 633 nm from a 15 mW He:Ne laser is coupled into the photonic structure by an objective. Objective and sample are mounted on micropositioners, as

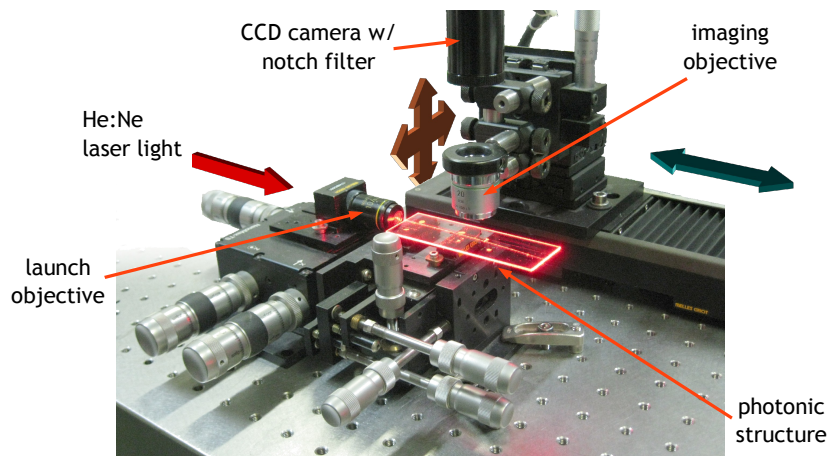


Figure 2.3: Setup employed to image the fluorescence pattern of the light propagation in waveguide arrays. Laser light at 633 nm is coupled into the photonic structure by an objective. The imaging setup, composed of an objective, a notch filter centered at the excitation wavelength and a CCD camera, is mounted on a three-axis translation stage. The translation along the waveguide axis is enabled by a computer controlled motorized stage; manual micropositioners adjust the position along the other two directions.

for mode and losses measurements (see Sections 2.2.2 and 2.2.3).

No imaging is performed of the end facet; on the other hand an imaging system is set for observing the sample from above. It consists of a 20X long working distance objective, a notch filter that suppresses light at 633 nm, and a CCD camera (Sony XC-ST70CE). The field of view of this system is limited to a few hundreds of microns, thus it is mounted on a motorized translation stage (Melles Griot Nanostep) with 150 mm travel and 1 μm precision, to allow scanning the whole sample. Manual translators on the other two axis are used to set the focus and the lateral adjustment.

Both the CCD camera and the motorized translation stage are computer controlled. A single MATLAB script synchronizes the image acquisition and camera translation. The stage is typically moved with steps of 500 μm and for each step a snapshot is taken with the CCD camera. An intensity profile is extracted averaging the three central pixel columns of the acquired image, then the stage is moved ahead. In this way the intensity distribution is sampled with steps equal to the translation step.

2.3 Fiber pigtailed setup

To provide enhanced operation reliability and robustness, the fabricated devices can be permanently coupled with optical fibers. This procedure is named *pigtail-ing* and consists in gluing optical fibers or fiber arrays to the input and output ports of the photonic device. A professional setup (Figure 2.4) is employed to this aim, which enables stable and precise reciprocal positioning of the fibers and

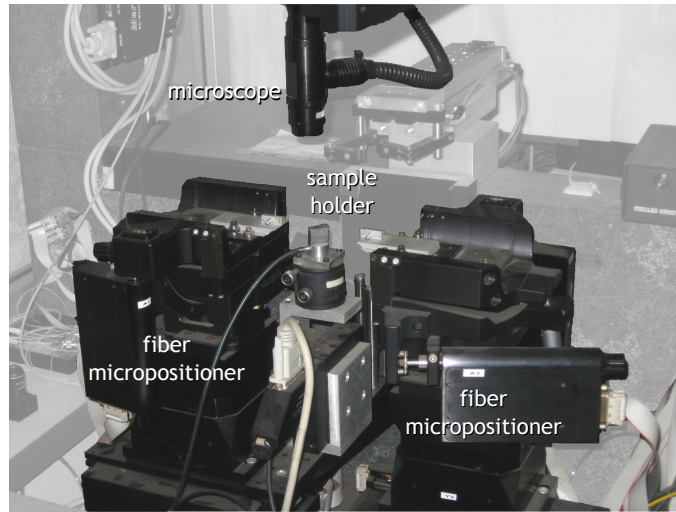


Figure 2.4: Fiber pigtailling setup. The waveguide device is mounted on the central stage. The two lateral stages allows for precise alignment of the fibers/fiber arrays, for an optimized waveguide coupling. A long working distance optical microscope allows observation from above.

the device.

The device is mounted on a two-axis motorized micropositioner (PI-Physik Instrumente), with three adjustable tilts. Other two servo-controlled micropositioners (Kensington Laboratories Inc.), each with three translational degrees of freedom and three tilts, are placed on the left and on the right of the sample. The fibers or fiber arrays to be glued to the sample are mounted on either (in case only the input/output ports need to be pigtailed) or both these micropositioners. The translation and tilting stages are computer controlled.

If single fibers have to be glued to the sample, the fiber tip is inserted in a glass ferrule, to provide more robustness.

The pigtailling procedure consists of a few steps. First, fiber and sample are carefully aligned using the micropositioners, optimizing the coupling between waveguides and fibers. The coupling efficiency can be monitored in real time by launching light at suitable wavelength in the input fiber and measuring the output power. Visual inspection of all the process is aided by a CCD camera mounted on an optical microscope.

Using the motorized micropositioners, fiber and sample are brought far from each other, enough to allow putting a drop of UV curing glue on the fiber tip and/or on the sample edge. Fibers are then brought close again to the waveguide ends. Due the high stability and reproducibility of the translation stages the optimized coupling conditions is not lost; anyway since the glue is still liquid it is possible to further adjust the reciprocal alignment. Finally, the glue is irradiated by a short-arc mercury lamp (Lumatec - Lightsource SUV DC E), providing more than 1 W of optical power in the wavelength range $320 \div 400$ nm. This allows permanent solidification of the glue with about 120 s of irradiation.

Chapter 3

Label-free biosensing by integrated interferometers

This Chapter discusses the development of two integrated interferometric devices for biosensing applications.

A first device, described in Section 3.1, was conceived in the context of the European project HIBISCUS. It addresses a precise problem, with application to microchip capillary electrophoresis and chemical reaction monitoring in a lab-on-chips: integrated label-free detection with high spatial resolution along a microfluidic channel. This is achieved by exploiting the unique capabilities of the fabrication technique, to produce a Mach-Zehnder interferometer with a three-dimensional geometry. The device was inscribed and tested both in a microfluidic chip completely fabricated by femtosecond laser pulses and in a commercial LOC for electrophoresis.

A second device, described in Section 3.2, consisting in an optofluidic chip fabricated by femtosecond laser, is used to explore the potentials of quantum interferometry on biological samples. The chip comprises again a Mach-Zehnder interferometer and a microfluidic channel, but measurements are performed with quantum states of light. This experiment was conceived in collaboration with the group of Prof. Jeremy O'Brien, at the Centre for Quantum Photonics of the Bristol University (UK). The design and fabrication of the femtosecond laser written chip was the main focus of my research activity; anyway I collaborated also to the measurements with quantum light, performed in the laboratories of the Bristol University.

3.1 Spatially resolved label-free detection with a three-dimensional Mach-Zehnder interferometer

3.1.1 Motivation for the work

Many of the integrated label-free sensors for lab-on-chips (LOCs) reported in literature (see Section 1.2.1) exploit an evanescent field interaction with the analyte. This approach is capable of excellent refractive index sensitivity, but typically needs a long interaction path. On the other hand, spatial resolution (hence, small interaction volumes) is required in several important applications, such as detection of molecules separated in a microchannel by capillary electrophoresis[127], counting cells in flow cytometry[128] or multipoint sensing[129] for monitoring the reaction kinetics in chemical microreactors.

In particular, within the framework of the European project HIBISCUS, we addressed the problem of label-free detection of the products of a chemical reaction, to monitor its efficiency. In particular, the reaction considered is the synthesis of an antibiotic from different peptides. A label-free detection technique is needed because fluorescent labelling would modify the chemical functionality of the reaction products. The reaction products are to be analyzed by microchip capillary electrophoresis[130]. In this technique the analytes, which are actually charged ions in solution, migrate along a microfluidic channel under the action of an intense electric field. The migration velocity depends on complex interactions between the ions and the solvent and it is different for ions with different shape and dimensions. Detection is performed at a point close to the extremity of the separation microchannel: ions with different speeds pass the detection point at different times. From the detection time one can identify the molecule, from the intensity of the detected peak one can retrieve the concentration. Note that the detection technique does not have to be *chemically* selective itself, but it must be *spatially* selective: since the molecules are moving along the channel, a large spatial detection window results in a large uncertainty in the arrival time.

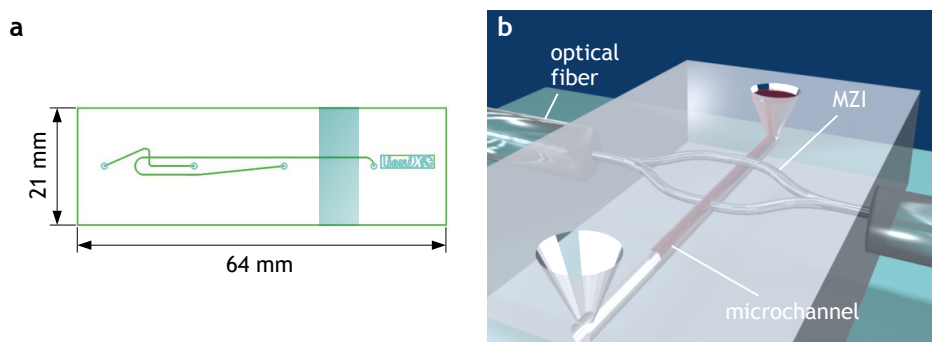


Figure 3.1: (a) Schematic of the commercial microchip for capillary electrophoresis (LioniX bv). The shaded area highlights the region where detection devices should be integrated. (b) Concept scheme of the integrated MZI fabricated by femtosecond laser, interfaced with a microfluidic channel. The sensing arm crosses orthogonally the channel, while the reference one passes over it.

A commercial LOC, optimized for capillary electrophoresis is produced by the company LioniX by (The Netherlands), which is one of the partners of the HIBISCUS project. The layout of the microchip is shown in Figure 3.1a. Two microchannels are present according to the classical cross scheme employed in microchip capillary electrophoresis (actually the cross is folded in order to minimize the footprint of the device). The microchannels are fabricated in a fused silica substrate, by photolithography followed by wet etching, and have a cross-section of $110\ \mu\text{m} \times 50\ \mu\text{m}$. In the sealed chip the microchannels are buried at a depth of $500\ \mu\text{m}$ from its surface. The shaded area of the chip in Figure 3.1a is the region where a detector for electrophoresis biomolecule recognition should be integrated.

In the light of the requirements discussed above, we chose to exploit the post-processing capabilities of femtosecond laser micromachining to fabricate an integrated Mach-Zehnder interferometer (MZI) in which the sensing arm crosses orthogonally the microchannel. The 90° intersection allows to achieve spatially selective detection, but at expense of the sensing length, which is limited to the channel width. Therefore, to maximize the phase shift induced by the analyte, direct intersection of the sensing arm with the microchannel is chosen (see concept scheme in Figure 3.1b). It is worth noting that in this configuration the reference arm, which must not interact with the microchannel, has to be fabricated at a different depth in the substrate with respect to the sensing arm: only femtosecond laser micromachining is able to produce a device with this geometry.

3.1.2 Development of the interferometric sensor

3.1.2.1 Preliminary fabrications

Waveguide optimization We chose to build a sensor working at telecom wavelengths, due to the great availability of compact tunable laser sources and detectors. Thus, we optimized waveguide fabrication in fused silica to achieve good mode matching with telecom fibers and low bending losses.

For waveguide writing, we adopted the second harmonic of the cavity-dumped femtosecond laser source, at 1 MHz repetition rate: the optimum processing parameters are reported in Table 3.1. Mode diameter at 1550 nm is $12\ \mu\text{m}$, propagation losses are about 1.5 dB/cm and bending losses down to 30 mm radius are negligible.

Planar Mach-Zehnder interferometers As a preliminary step to the integration with microfluidic channels, a planar unbalanced MZI was fabricated in plain fused silica substrate. The design adopted for this MZI is shown in Figure 3.2a. The bending radius for the curved segments is $R = 30\ \text{mm}$ and the overall device length is $D = 17\ \text{mm}$. The imbalance Δs between the two arm lengths is $56\ \mu\text{m}$. Y-splitters were employed as beam dividers and combiners, instead of directional couplers, in order to increase the compactness of the device and avoid any wavelength dependence of the splitting ratio.

To perform the device characterization, light from a fiber-coupled tunable laser (Agilent 8164B) was injected, using a polarization-maintaining single-mode fiber; output light was collected by a standard single-mode fiber and sent to a

Fabrication parameters	
Substrate	fused silica
Laser system	Yb:KYW cav. dump.
Wavelength	515 nm (SHG)
Repetition rate	1 MHz
Pulse energy	90 nJ
Translation speed	100 $\mu\text{m/s}$
Objective	0.6 NA

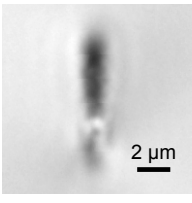


Table 3.1: Waveguide writing parameters used for inscribing the MZI. Microscope image of the waveguide cross-section is also shown: the guiding region is created below an elongated zone of negative refractive index modification.

power meter. This allowed to measure the wavelength dependent transmission of the MZI in the range $1460 \div 1570$ nm.

Theory predicts, for an unbalanced interferometer, a power transmission T as a function of the wavelength λ expressed by:

$$T = \frac{1}{2} \left[1 + \cos \left(\frac{2\pi}{\lambda} n_0 \Delta s \right) \right] \quad (3.1)$$

where $n_0 \simeq 1.45$ is the effective refractive index of the guided mode. Figure 3.2b shows the transmission spectrum of the unbalanced MZI together with a fitting curve following the expression in Eq. (3.1). From the fitting function one obtains $\Delta s = 54 \mu\text{m}$, which is in very good agreement with the design value $\Delta s = 56 \mu\text{m}$. This demonstrates a remarkable control of the geometric properties of the MZI and of the refractive index uniformity in the two arms. The overall insertion losses of the device, measured after butt-coupling two single-mode fibers at the input and output ports, are 7.4 dB. The fringe visibility depends on the splitting ratios of the input and output Y-coupler and on the propagation losses of the guided mode in the interferometer arms (see Appendix A). Therefore, the high fringe contrast obtained in our experiment (up to 13 dB in the considered 110 nm spectral range), is a clear indication of the high symmetry in the splitter and combiner sections and of the closely balanced propagation losses in the two arms.

3.1.2.2 All-femtosecond laser fabricated optofluidic sensor

Integration of the interferometer with an etched microchannel To benchmark the MZI capabilities before the final integration into a commercial LOC for electrophoresis, unbalanced MZIs were inscribed in a fused silica chip where a microfluidic channel had already been fabricated by femtosecond laser, realizing exactly the configuration of Figure 3.1b.

The microchannel was produced by irradiation of a U-shaped line with pulses from a Ti:sapphire laser system, followed by etching in HF solution, according to the procedure in Ref. [131]. Two access holes connect the 2 mm long and 100 μm buried microchannel to the top surface of the sample. Its average diameter is

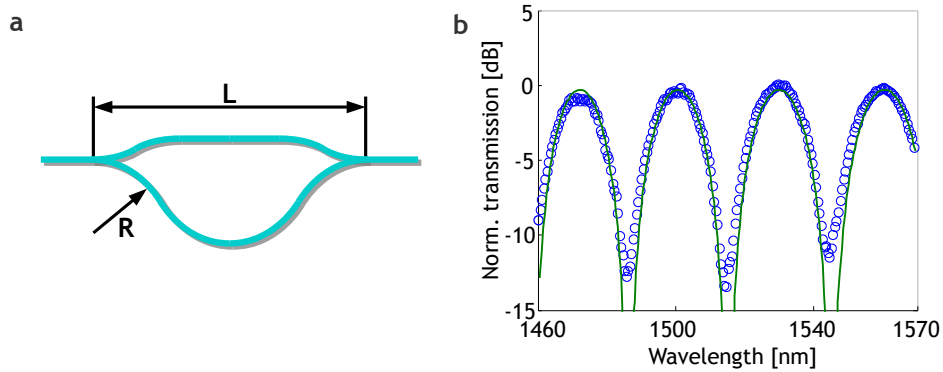


Figure 3.2: (a) Schematic of the unbalanced MZI with $R = 30$ mm and $D = 17$ mm. (b) Measured transmission spectrum of the MZI realized in plain fused silica substrate (*open circles*), with least-square fit of the theoretical function (*solid line*).

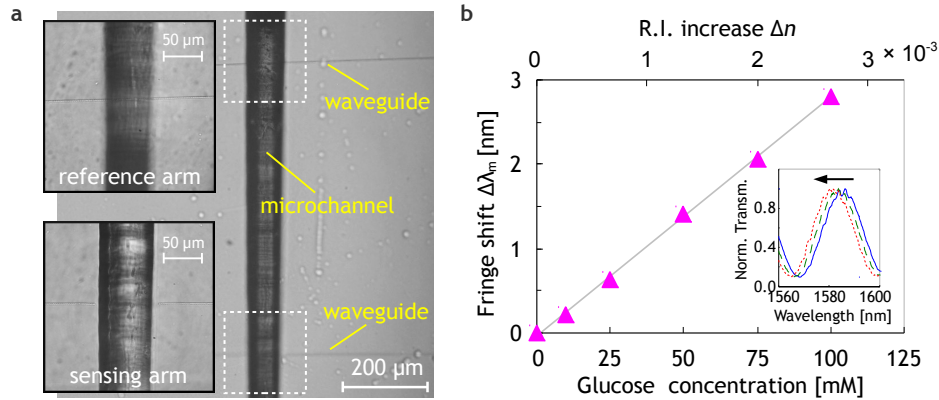


Figure 3.3: (a) Microscope picture showing the two arms of the MZI crossing the microfluidic channel. Because of the tilted geometry, the reference arm (*panel on top left*) passes over the channel while the sensing arm (*panel on bottom left*) crosses the channel. (b) Measured fringe shift for different concentrations of glucose-D in water (inset: 0 mM solid; 50 mM dashed; 100 mM dotted); the correspondent refractive index increase is also shown in the top axis.

about $60 \mu\text{m}$. External connection to syringes is achieved by gluing a Luer Lock connector to one of the access holes.

The shape and the dimensions of the MZI are the same of the planar prototype discussed previously (Figure 3.2a). To enable only one arm to intersect the microchannel, the MZI was inscribed in a plane tilted by 7° with respect to the horizontal. The sensing arm of the MZI (which is chosen as the shorter one) orthogonally intersects the microchannel in its center, while the reference arm passes $20 \mu\text{m}$ above the microchannel (see Figure 3.3a). To avoid damaging the channel walls, the writing laser beam was blocked by a synchronized shutter while inscribing the sensing arm through the channel, making the optical waveguide stop at $5 \mu\text{m}$ from the microchannel wall.

The MZI sensing arm, crossing the microchannel filled with water, experiences an additional loss of about 3 dB, due to both scattering at the channel walls and lack of waveguide confinement across the channel. This loss does not significantly affect the device performance, still allowing fringe contrast as high as 10 dB (see inset of Figure 3.3b).

The high spatial resolution achieved with this geometry can be appreciated by observing that the sensing region is a cylinder with a height equal to the channel width ($\sim 60 \mu\text{m}$) and a base with a diameter of the order of $10 \div 15 \mu\text{m}$, given by the waveguide mode size.

Operation principles of the interferometric sensor The transmission spectrum of the MZI crossing the microchannel has the following expression, slightly different from Eq. (3.1):

$$T = \frac{1}{2} \left[1 + \cos \left(\frac{2\pi}{\lambda} (n_0 \Delta s - (n_{channel} - n_0) L) \right) \right] \quad (3.2)$$

where we have neglected the difference in propagation loss of the two arms, for simplicity. In particular, the phase difference between the two arms of the MZI is not only due to a length difference (the $n_0 \Delta s$ term), but also to a different refractive index of the content of the microchannel ($n_{channel}$) with respect to the effective index of the guided mode (n_0) in the reference arm (the $(n_{channel} - n_0) L$ term, where L is the microchannel width). Consequently, the transmission spectrum shows fringes with peaks positioned at:

$$\lambda_m = \frac{n_0 \Delta s - (n_{channel} - n_0) L}{m} \quad (3.3)$$

where m is the fringe order.

If the content of the microchannel changes its refractive index by a quantity Δn , the transmission peaks shift by:

$$\Delta \lambda_m = - \frac{\Delta n L}{m} \quad (3.4)$$

Considering a limited portion of the transmission spectrum (a few fringe peaks) with m large enough (in our case on the order of 50) we can assume the $\Delta \lambda_m$ shift constant for all the fringes. As a consequence, the shift in the fringe peaks is proportional to the refractive index change Δn in the microchannel.

The fringe shift $\Delta \lambda_m$ can be accurately retrieved by a Fourier transform of the MZI transmission spectrum. In fact, the Fourier transform of the shifted $T(\lambda)$ can be expressed as:

$$\mathcal{F} \{ T(\lambda - \Delta \lambda_m) \} = \mathcal{F} \{ T(\lambda) \} e^{i 2\pi \Delta \lambda_m f} \quad (3.5)$$

where f is the Fourier frequency. Monitoring the phase shift of $\mathcal{F}(T)$ at a fixed frequency f (typically chosen as that corresponding to the peak of the Fourier transform amplitude) it is possible to easily retrieve the fringe shift $\Delta \lambda_m$. This procedure can be rapidly and automatically performed by standard numerical methods.

It can be observed that the acquisition of the device transmission spectrum, using a tunable laser, requires a finite time and is thus particularly suited for static measurements. For applications, such as capillary electrophoresis, which involve the detection of transient signals on faster time scales, different approaches are possible. A large bandwidth source and an optical multichannel analyzer can be adopted. Otherwise, aiming at even higher temporal resolutions, the device transmission can be measured at a fixed wavelength: in this case the fringe shift, induced by a refractive index change of the analyte, translates to a change in transmission.

Test with glucose solutions To characterize the sensitivity and the linearity of the interferometer response, the microchannel was filled with differently concentrated glucose-D aqueous solutions, acquiring for each of them the spectral response of the optofluidic device (see inset in Figure 3.3b) in static conditions. The measurement configuration was the same adopted for the characterization of the planar MZI. Figure 3.3b shows the fringe shift $\Delta\lambda_m$, obtained by the Fourier transform method illustrated above, as a function of glucose concentration. X-axis top scale represents the corresponding refractive index variation of the solutions with respect to pure water, based on data reported in the literature[132].

The fringe shift dependence on the molar concentration of the analyte in the microchannel is estimated by a linear fit to be 28.4 nm/M. Since the refractive index variation dependence on concentration is known to be 2.66×10^{-2} RIU/M the device responsivity is estimated at 1070 nm/RIU.¹

The standard deviation of the data taken from repeated measurements is $\sigma \simeq 3 \times 10^{-5}$ RIU: therefore a limit of detection of 1×10^{-4} RIU can be extrapolated for a signal-to-noise ratio $\simeq 3$. Temperature fluctuations of the analyte (± 0.5 °C) can indeed be identified as the main limiting factor for the device sensitivity. In fact, the refractive index variation of water due to temperature is on the order of 10^{-4} RIU/°C. On the other hand, the device itself is quite insensitive to temperature fluctuations, because the thermo-optical coefficient of fused silica is an order of magnitude lower (10^{-5} RIU/°C) and index changes of the fused silica waveguides are actually compensated in the MZI geometry, apart from the small length difference between the two arms. To confirm this hypothesis, measurements were repeated at room temperature with the empty microchannel, as the temperature dependence of the refractive index of air is much weaker than that of water. These measurements yielded a noise level $\sigma \simeq 3 \times 10^{-6}$ RIU, which leads to conclude that fluctuations in the data of Figure 3.3b are not due, for the most part, to the ultimate instrument sensitivity or by the data processing precision, but are indeed real variations of the refractive index of the analyte due to temperature fluctuations. One can thus foresee that an order of magnitude improvement in sensitivity could be achieved if the analyte were temperature stabilized.

We finally performed some dynamic measurements, to test the capability of the device to detect rapid transients. The same tunable laser used in spectral

¹RIU stands for Refractive Index Unit and is used only for clarity, being the refractive index an adimensional quantity.

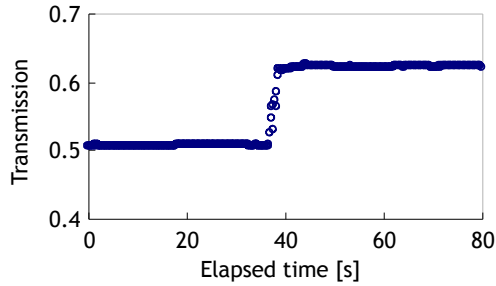


Figure 3.4: Transient measurement performed by driving a flow of glucose solution with 30 mM concentration into a channel originally filled with water.

acquisition was operated at constant wavelength and the transmission was acquired via a photodetector at 200 ms intervals. A flow of a glucose solution was driven into the microchannel, initially filled with water. A syringe connected to the microchannel was used to apply a constant pressure of 2.2×10^5 Pa, inducing a flow rate of 3 mL/s. Figure 3.4 shows the transition between pure water and the glucose solution with concentration of 30 mM, occurring in 2 s. This demonstrates the capability of our device to monitor fast refractive index transients in the microchannel.

3.1.3 Integration in commercial lab-on-chip

Sensing of peptides

The MZI sensor was finally integrated in the commercial microfluidic chip described in Section 3.1.1. Figure 3.5a shows four MZIs at the end of the separation channel (see shaded area in Figure 3.1a). Also in this case the sensing arm is crossing the microchannel, while the reference arm is passing above it (Figure 3.5b-c). Optical fibers were permanently bonded to the input and output waveguides².

Sensitivity characterization and device calibration were performed by filling the chip with aqueous glucose-D solutions at different concentrations. Figure 3.6 shows the experimental fringe shift as a function of the glucose concentration. From these measurements the device responsivity was estimated to be 1500 nm/RIU, larger than the one of the device working with the etched microchannel. The reason for the increased responsivity is the larger width of the microchannel (increased from 60 to 110 μm), thus implying a greater interaction length of light with the fluidic sample. Consistently with Eq. (3.4), it can be observed that the responsivity does not scale linearly with the interaction length L , because also m increases with L , for a fixed wavelength region. Repeating the measurement several times at each concentration a standard error $\sigma \simeq 4.8 \times 10^{-5}$ RIU was estimated, which is very similar to that obtained in Section 3.1.2.2. This allows to extrapolate, also for this device, a limit of detection of 1.5×10^{-4} RIU (equivalent to about 5 mM of glucose-D) for a signal-to-noise ratio $\text{SNR} = 3$.

²Precisely, a polarization maintaining fiber at the input and a standard single mode fiber at the output

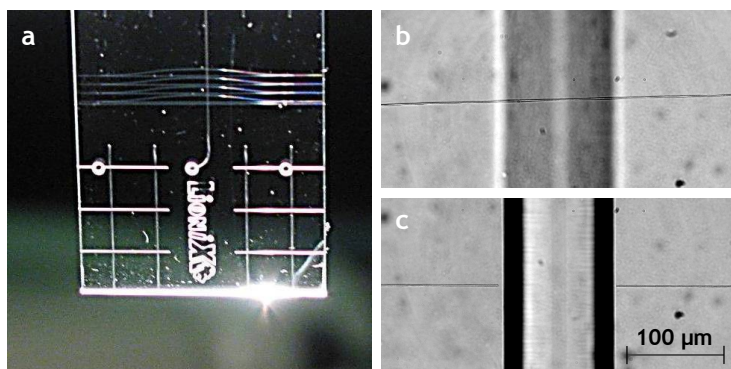


Figure 3.5: (a) Picture of the commercial LOC with 4 MZIs inscribed across a microchannel; the grid of microchannels at the bottom of the chip facilitates the sealing of the device and has no fluidic function. Microscope images of (b) the reference arm passing over the microchannel and (c) the sensing arm crossing it.

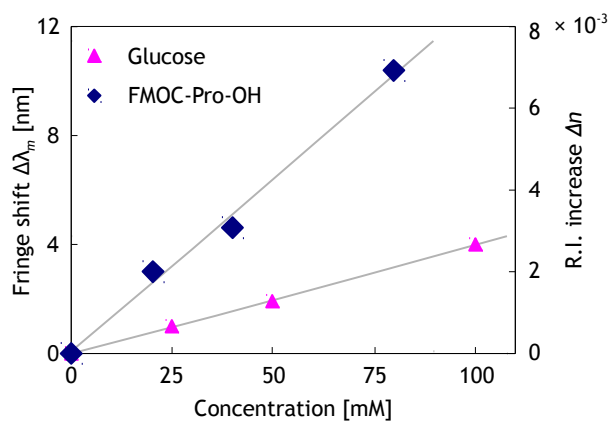


Figure 3.6: Measured fringe shift for different concentrations of FMOc-Pro-OH in ethanol (*diamonds*) and correspondent refractive index increase. The refractive index scale has been calibrated with the data related to glucose in water (*triangles*).

Having assessed the performance of the device, we employed it to detect biochemically relevant molecules such as peptides, used for drug synthesis in the pharmaceutical industry. Figure 3.6 shows the concentration dependent signal of the mono-peptide Fmoc-Pro-OH in ethanol. The previous calibration, based on glucose solutions, quantitatively associates a refractive index increase to the measured phase shift. Thus, the refractive index dependence on concentration for Fmoc-Pro-OH can be determined, which resulted to be linear with a slope of 8.2×10^{-5} RIU/mM. In this case, given the higher temperature dependence of the refractive index of ethanol with respect to that of water, a standard error of 2.6×10^{-4} RIU was measured. Therefore, we can estimate a limit of detection of 9 mM for the peptides. This value is very well suited for the applications we aimed at, such as detection in microchip capillary electrophoresis of the products of chemical reactions, which have typical concentrations in the tens of mM range, and can thus be monitored in a label-free way thanks to the integrated MZI.

3.2 Integrated quantum biosensing

3.2.1 Design of the optofluidic quantum biosensor

Quantum interferometry on biological samples One of the applications envisaged for quantum interferometry is the measurement of samples that are photo-sensitive: the quantum enhancement in sensitivity would allow to use less photons, with respect to a classical measurement, for extracting the desired information. Nevertheless, quantum interferometry, and in particular quantum interferometry with N00N states, which is able to reach the Heisenberg limit, up to now has been benchmarked only with artificial phase shifters. In the experiment described in the following, we explore the possibility of performing quantum optical interferometry on biological solutions to retrieve their refractive index, which can be related, for example, to the solution concentration. We propose and experimentally test an optofluidic approach to this problem, using femtosecond laser fabrication to realize a LOC in some aspects analogous to the one described in Section 3.1.2.2. In particular, our architecture consists of a MZI interfaced with a microfluidic channel, according to the design in Figure 3.7. Note that in this way the intrinsic stability of integrated photonics, which is an unquestionable requirement for real world applications of quantum optics (see discussion in Section 1.3.1.3), is conjugated with the superior capabilities of microfluidics in handling with high precision chemical and biological samples.

Generation of N00N states in a Mach-Zehnder interferometer Before going into the details of the experiment, it is useful to briefly review how a MZI can be used for quantum sensing with two-photon N00N states[91]. Deterministic generation of N00N states is a non trivial task, in the general case. The case $N = 2$ is however fairly simple, since a $(|20\rangle + |02\rangle) / \sqrt{2}$ state is generated with unitary probability at the outputs of a balanced beam splitter, when two indistinguishable photons are injected in the two inputs (see Appendix A). The overall matrix of

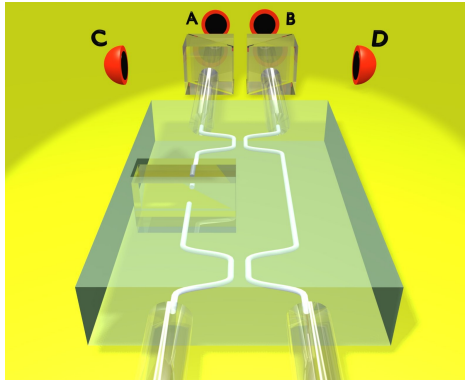


Figure 3.7: 3D picture of the femtosecond laser fabricated LOC for quantum interferometry. A Mach-Zehnder interferometer is interfaced with a rectangular microchannel. Concept scheme of the detection setup is also depicted, consisting of two beam splitters and four detectors (A, B, C, D). In the experimental realization beam splitters and detectors are fiber-coupled.

a lossless Mach-Zehnder device, with a phase retarder ϕ on one mode (it is the sample in the sensing arm), can be written³ as

$$U_{\text{MZ}} = ie^{i\phi/2} \begin{bmatrix} -\sin\left(\frac{\phi}{2}\right) & \cos\left(\frac{\phi}{2}\right) \\ \cos\left(\frac{\phi}{2}\right) & -\sin\left(\frac{\phi}{2}\right) \end{bmatrix} \quad (3.7)$$

hence, the MZI will perform the following transformation on an input state of two indistinguishable photons (neglecting the common phase term):

$$|1_a 1_b\rangle = a^\dagger b^\dagger |0\rangle \longrightarrow \cos(\phi) a^\dagger b^\dagger |0\rangle + \sin(\phi) \frac{a^{\dagger 2} - b^{\dagger 2}}{2} |0\rangle \quad (3.8)$$

Two states are possible at the output, $|1_a 1_b\rangle$ and $(|2_a 0_b\rangle - |0_a 2_b\rangle)/\sqrt{2}$, with the following detection probabilities:

$$p_{|11\rangle} = \cos^2 \phi = \frac{1 + \cos(2\phi)}{2} \quad p_{\frac{|20\rangle - |02\rangle}{\sqrt{2}}} = \sin^2 \phi = \frac{1 - \cos(2\phi)}{2} \quad (3.9)$$

Both probabilities oscillate at 2ϕ frequencies: this means that detecting one or both the output states an interference fringe can be observed, at varying ϕ , with half the periodicity of the classical one (super resolution). It can be shown that the unitary visibility of the fringe also yields supersensitivity.

3.2.2 Device fabrication and measurement protocols

3.2.2.1 A lab-on-chip for quantum interferometry

Optimization of the Mach-Zehnder interferometer In order to allow the fabrication of both waveguides and microchannels by femtosecond laser pulses, the substrate must be fused silica. The first step of the work was the optimization of single mode waveguides at 785 nm wavelength; this was the wavelength of the available source of indistinguishable photons. The mode supported by these waveguides must be sufficiently confined to allow bending with reasonably low losses and good mode matching with optical fibers.

Optimum processing parameters are reported in Table 3.2. Waveguides were fabricated using five overlapped scans at the same speed, at 400 μm depth into the substrate. A cylindrical telescope, shaping the writing beam, is employed to control the shape of the waveguide cross-section. In particular, elliptical waveguides were produced, so that the asymmetry in the cross-section induced a waveguide birefringence. This helps to preserve the photon polarization in the integrated MZI and maximizes the interference between the photons of the sensing and reference arms.

³It is the ordered product of the matrix of the second beam splitter, the matrix of the phase retarder in the sensing mode only and the matrix of the first beam splitter.

$$U_{\text{MZ}} = \frac{1}{\sqrt{2}} \begin{bmatrix} 1 & i \\ i & 1 \end{bmatrix} \times \begin{bmatrix} 1 & 0 \\ 0 & e^{i\phi} \end{bmatrix} \times \frac{1}{\sqrt{2}} \begin{bmatrix} 1 & i \\ i & 1 \end{bmatrix} \quad (3.6)$$

Fabrication parameters	
Substrate	fused silica
Laser system	Yb:KYW cav. dump.
Wavelength	515 nm (SHG)
Repetition rate	1 MHz
Pulse energy	300 nJ
Translation speed	1.5 mm/s (five scans)
Objective	0.6 NA + cyl. telescope

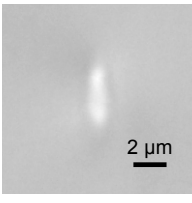


Table 3.2: Waveguide writing parameters used for building the MZI for quantum biosensing. Microscope image of the waveguide elliptical cross-section is also shown.

Mode dimension at 785 nm is $9\ \mu\text{m} \times 19\ \mu\text{m}$. Propagation losses in the waveguides were estimated to be less than 0.5 dB/cm and additional bending losses less than 0.5 dB/cm for the 80 mm bending radius adopted in the MZI design.

Differently from the one described in Section 3.1, the MZI design (Figure 3.7) does not adopt Y-splitters as beam dividers and combiners, but directional couplers. To perform N00N states interferometry, it is indeed necessary to access both the optical modes at the input and at the output (see discussion in Section 3.2.1).

The interaction length for the directional couplers was tuned to achieve balanced splitting ratio.

Fabrication of the lab-on-chip The integrated optofluidic device was entirely fabricated using the Yb:KYW cavity-dumped oscillator. Several devices, each composed of a microchannel interfaced with a MZI, are realized on the same $2\ \text{cm} \times 2\ \text{cm}$ glass chips.

Waveguides were produced with the parameters of Table 3.2.

The microchannel is realized by laser irradiation followed by etching in HF solution, using the technique described by *Vishnubhatla et al.*[133]. In order to obtain perfect verticality of the microchannel walls it is necessary to compensate for the intrinsic tapering induced by the etching process along the z-axis. This is achieved by irradiating a helicoidal path in order to obtain double-pyramidal structure (Figure 3.8a). A single laser scan at 0.5 mm/s, using 300 nJ pulses of the second harmonic, is employed, with the same focusing setup used for the waveguides. After laser irradiation the sample is immersed in HF solution for 70 min. The HF acid selectively etches the irradiated material, proceeding along the z-axis from the bottom and top surfaces, simultaneously. This technique produces a microchannel through the 1 mm thick glass sample with a uniform rectangular cross-section of $55\ \mu\text{m} \times 500\ \mu\text{m}$.

Laser irradiation for both interferometers and microchannels is performed in the same run (Figure 3.8b). The HF etching does not attack the waveguides because the irradiation was interrupted some microns before the microchannel region and before the sample edge: in this way they do not reach any interface which is in contact with the acid. On the contrary, the microchannel irradiation reaches the top and bottom surfaces of the sample. Polishing of the edges of the

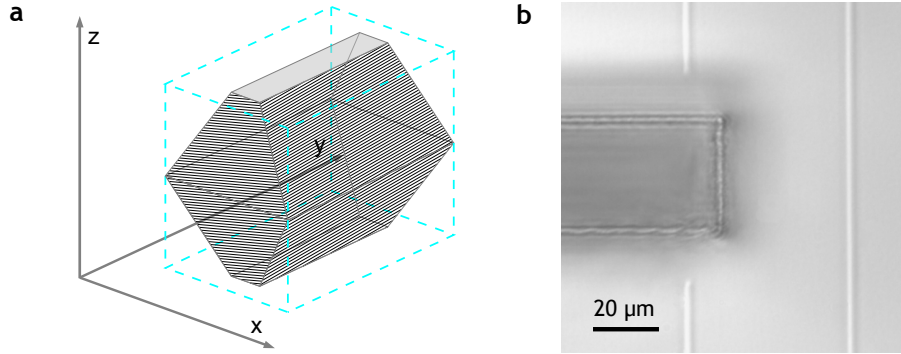


Figure 3.8: (a) Schematic of the double-pyramidal structure irradiated by femtosecond pulses, and then etched in HF solution, in order to obtain a rectangular microchannel with vertical walls. (b) Interface region between the sensing arm of the MZI and the microchannel, imaged with an optical microscope after laser irradiation, before etching. Both the waveguides and the microchannel structure are irradiated in the same run. The waveguide of the sensing arm is interrupted at a distance of some microns from the microchannel structure, in order not to be etched by the acid.

chip is performed after the etching process: this allow effective fiber butt-coupling to the interferometers.

The chosen geometry for the microchannel allows easy filling with the desired liquid just by casting a droplet on the top aperture and exploiting capillary action. This geometry was chosen for its simplicity but extension to a completely integrated microfluidic delivery of the sample is straightforward[70].

3.2.2.2 Measurement setup and normalization procedures

To perform the sensing experiment, a separable state $|11\rangle$ of identical photons was prepared using spontaneous parametric down-conversion and injected by polarization maintaining fibers into the input ports of the MZI. Output photons were collected by standard telecommunication fibers (monomodal at 1550 nm wavelength, but multimodal at 785 nm wavelength used), in order to increase the collection efficiency. Photons were then detected by four single-photon avalanche photodiodes (A, B, C and D in Figure 3.7), cascaded to two 50:50 beam splitters.

Both classical and quantum optical interferometric experiments consist in measuring a specific output state rate. Considering the 2×2 -ports MZI employed in our experiment, classical measurements can be performed feeding the device with single photons from one input and counting output states $|01\rangle$ or $|10\rangle$. Quantum measurements with two-photon $N00N$ states can be performed, as discussed, by feeding the interferometer with two indistinguishable photons and detecting the output states $|11\rangle$, $|20\rangle$ or $|02\rangle$.

The detection rate of any of these states depends on the interferometric phase (which is what we want to measure), as well as on photon losses and detector efficiencies. In particular, in the two-photon quantum interferometry experiments reported in literature, only the coincidence counts from a couple of detectors, e.g. A and B, are commonly taken as measurement results. This approach requires an

extremely stable setup and a careful calibration of the optical elements employed. Furthermore, variations in the losses or in the efficiencies cannot be distinguished from variations in the interferometric phase. However, to develop a reliable sensor the results should be insensitive to the environment perturbations and should be quite reproducible even when performed on different sensing chips. Therefore, we developed and adopted robust normalization procedures for both the singles and coincidences measurements.

For obtaining the single photon fringe, the following counts are considered:

$$\begin{aligned} A1|_{\text{meas}} &= p_{|10\rangle} \eta_A N_1 \\ A2|_{\text{meas}} &= p_{|01\rangle} \eta_A N_2 \\ B1|_{\text{meas}} &= p_{|01\rangle} \eta_B N_1 \\ B2|_{\text{meas}} &= p_{|10\rangle} \eta_B N_2 \end{aligned}$$

where $Xk|_{\text{meas}}$ stays for experimental single counts rate for detectors X when photons are injected through input k . $p_{|ij\rangle}$ is the probability for a $|ij\rangle$ state to be emitted by the interferometer, N_k is the rate at which input photons are effectively injected and efficiency η_X is the fraction of states $p_{|ij\rangle}$ that is actually detected, and includes losses, splitting ratios and detector efficiency. $p_{|01\rangle}$ can be retrieved independently from all the unknown parameters, with the following formula:

$$p_{|01\rangle} = \frac{\sqrt{A2|_{\text{meas}} B1|_{\text{meas}}}}{\sqrt{A2|_{\text{meas}} B1|_{\text{meas}} + \sqrt{A1|_{\text{meas}} B2|_{\text{meas}}}}} \quad (3.10)$$

The latter can be adopted as normalized quantity for constructing the single-photon interference fringe.

An analogous normalization method is adopted for the evaluation of the two-photon interference fringe. Coincidence counts of detectors AB, CD, AC and BD are acquired, and can be written as:

$$\begin{aligned} AB|_{\text{meas}} &= N_{|11\rangle} \eta_A \eta_B \\ CD|_{\text{meas}} &= N_{|11\rangle} \eta_C \eta_D \\ AC|_{\text{meas}} &= N_{|20\rangle} \eta_A \eta_C \cdot 2 \\ BD|_{\text{meas}} &= N_{|02\rangle} \eta_B \eta_D \cdot 2 \end{aligned}$$

where $XY|_{\text{meas}}$ stays for experimental coincidence count rates for the couple of detectors XY and $N_{|ij\rangle}$ for the rate at which the state $|ij\rangle$ is emitted at the output of the interferometer. The factor 2 in the expressions of $AC|_{\text{meas}}$ and $BD|_{\text{meas}}$ takes into account that the two photons can be inverted. In this case we calculate the following normalized quantity:

$$x_{|11\rangle} = \frac{N_{|11\rangle}}{N_{\text{tot}}} = \frac{N_{|11\rangle}}{N_{|11\rangle} + N_{|20\rangle} + N_{|02\rangle}} \quad (3.11)$$

being $N_{|20\rangle} = N_{|02\rangle}$, which is true if we consider a MZI with two 50:50 couplers. The former expression is related to the acquired coincidence counts by:

$$x_{|11\rangle} = \frac{\sqrt{AB|_{\text{meas}} CD|_{\text{meas}}}}{\sqrt{AB|_{\text{meas}} CD|_{\text{meas}} + \sqrt{AC|_{\text{meas}} BD|_{\text{meas}}}}} \quad (3.12)$$

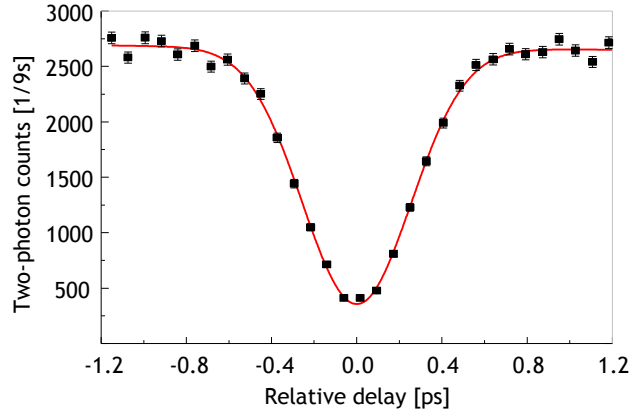


Figure 3.9: Quantum interference in the MZI when the microfluidic channel is filled with distilled water. The coincidences at the detectors A and B are plotted as a function of the relative delay between the two photons.

As detailed above, all the experimental quantities $Xk|_{\text{meas}}$ or $XY|_{\text{meas}}$ depends on efficiency terms which in principle could be characterized in each setup, but in real applications could vary in time between measurements anyway, e.g. due to misalignments induced by external perturbations. On the contrary, the normalized quantities of Eq. (3.10) and (3.12) completely eliminate this issue.

3.2.3 Experimental measurements and discussion

3.2.3.1 Hong-Ou-Mandel interference

As a preliminary experiment, we performed a Hong-Ou-Mandel[100] experiment, with the microchannel filled by distilled water (Figure 3.9). In fact we observed that the phase induced by the distilled water in the sensing arm is approximately equal to $\pi/2$: hence, in this condition, the interferometer behaves like a balanced beam splitter (see the expression of the matrix of a MZI in Eq. (3.6)). Two indistinguishable photons were injected in the device and coincidences counts at detector A and B were acquired, varying the temporal delay between the two photons. This allowed to optimize the temporal superposition of the photons. A visibility⁴ $\mathcal{V} = 86.7 \pm 1.3\%$ of the quantum interference dip is observed. This value has to be compared to a theoretical upper bound of $\mathcal{V}_{\text{HOM}} = 88\%$, which can be calculated taking into account photon losses due to the microchannel crossing (see also Section 3.2.3.3). Slightly changing the refractive index of the liquid to reach a precise 50:50 splitting ratio of the MZI may further increase the experimental visibility; anyway, the rather high measured value already confirms

⁴Visibility of the Hong-Ou-Mandel dip is defined as $\mathcal{V} = \left| \frac{c_0 - c_{int}}{c_0} \right|$, where c_0 and c_{int} correspond respectively to the coincidence rate outside interference (i.e. input photons with a reciprocal delay larger than their coherence time) and inside interference (perfect temporal overlap).

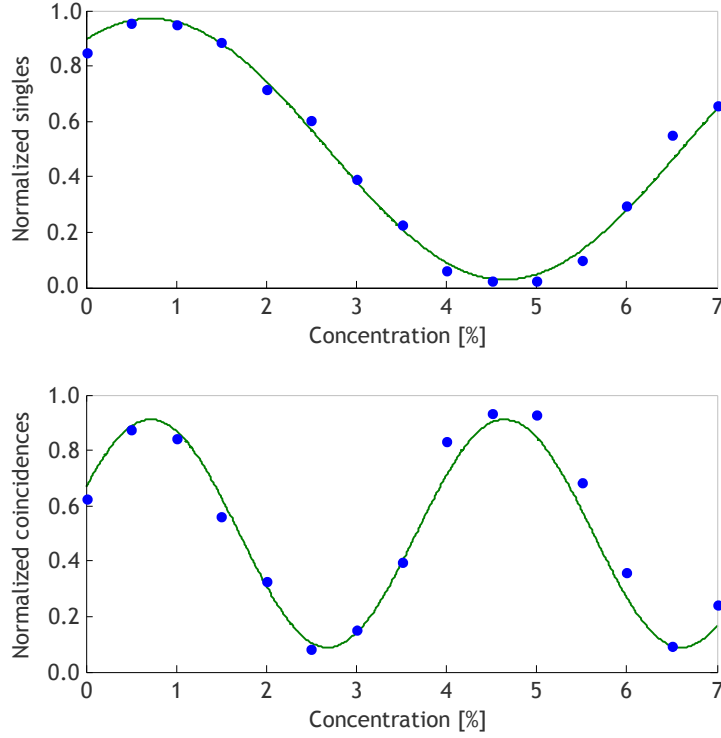


Figure 3.10: Normalized single photon counts (*top*) and two photon coincidences (*bottom*) for different concentrations of bovine serum albumin in a buffer solution (*full circles*). The solid line represents a fitting of the experimental points with a sinusoidal curve.

the fact that the optofluidic chip nicely preserves the quantum coherence of the photons.

3.2.3.2 Measuring albumin concentration

We then proceeded to measure real biological samples. In particular, we chose to measure bovine serum albumin (BSA) solutions because it is a sample with well known properties, good stability and numerous biochemical applications.

Normalized coincidence counts $x_{|11\rangle}$ were acquired for the microchannel filled with different BSA concentrations in buffer solution, ranging from 0% to 7% with 0.5% step. Rinsing of the microchannel with deionized water and acetone was performed before and after each measurement. Results are reported in Figure 3.10. For each concentration we also acquired normalized single photon counts $x_{|10\rangle}$, to have a comparison with a classical measurement.

Both the experimental data set were fitted with a sinusoidal curve, which allowed to calculate 94% and 82% fringe visibilities, respectively, for the single photon counts and the two-photon coincidences.

From the fitting we could also infer the phase shift dependence on sample concentration $d\phi/dC = 1.58$. The phase shift is related to the concentration of

the sample through the following

$$\frac{d\phi}{dC} = \frac{2\pi LN}{\lambda} \frac{dn_s}{dC} \quad (3.13)$$

where $L = 55 \mu\text{m}$ is the microchannel length, $N = 2$ is the number of photons of the N00N state and $\lambda = 0.785 \mu\text{m}$ is the photon wavelength. From the above equation we can retrieve the dependence of the sample refractive index on its concentration $dn_s/dC = 1.79 \times 10^{-3}$, which is in excellent agreement with the 1.82×10^{-3} value reported in literature[134]. This result validates the present method, based on quantum interference, as a reliable tool to measure significant quantities of biological samples.

3.2.3.3 Fringe visibility, losses and sensitivity

The visibility of the two-photon interference fringes has often been used in literature as an indicator of the possibility of overcoming the standard quantum limit (i.e. the sensitivity limit of classical measurement). In fact, neglecting all losses and inefficiencies, with a two-photon measurement the standard quantum limit is beaten with an experimental visibility higher than the threshold value $\mathcal{V}_{\text{th}} = 1/\sqrt{2} = 71\%$. It can be noticed that our result is well above this threshold. However, in our device some not negligible losses are present, due to the fact that the sensing arm crosses the microchannel that contains the sample. Light, formerly confined into the waveguide, diverges during the microchannel crossing because of diffraction and thus experiences some losses when coupling back to the waveguide on the other side of the microchannel. As a matter of fact, losses in the sensing arm of an interferometer are recognized as a preeminent problem in quantum sensing as pointed out in some recent papers[135, 136].

These losses are quite intrinsic of our optofluidic sensing strategy and can be reduced by decreasing the microchannel length, but at the expense of device sensitivity. It is thus useful to model and discuss more accurately the influence of these losses.

Losses in the sensing arm can be modeled by adding a further beam splitter in the Mach-Zehnder structure, which makes the sensing mode interact with the loss mode(Figure 3.11a). The matrix describing the evolution of the annihilation operators of the three-modes is ⁵ :

$$U_{\text{MZI},\text{loss}} = \begin{bmatrix} \frac{1}{2}(1 - te^{i\phi}) & \frac{i}{2}(1 + te^{i\phi}) & -\sqrt{\frac{1-t^2}{2}} \\ \frac{i}{2}(1 + te^{i\phi}) & -\frac{1}{2}(1 - te^{i\phi}) & i\sqrt{\frac{1-t^2}{2}} \\ -e^{i\phi}\sqrt{\frac{1-t^2}{2}} & ie^{i\phi}\sqrt{\frac{1-t^2}{2}} & t \end{bmatrix} \quad (3.14)$$

where $T = t^2 = 61\%$ is the experimentally measured power transmission in the sensing arm when crossing the microchannel. As a consequence, we can calculate

⁵It is given by the product of the matrices of the single elements, as follows:

$$U_{\text{MZI},\text{loss}} = \begin{bmatrix} \frac{\sqrt{2}}{2} & i\frac{\sqrt{2}}{2} & 0 \\ i\frac{\sqrt{2}}{2} & \frac{\sqrt{2}}{2} & 0 \\ 0 & 0 & 1 \end{bmatrix} \times \begin{bmatrix} 1 & 0 & 0 \\ 0 & t & i\sqrt{1-t^2} \\ 0 & i\sqrt{1-t^2} & t \end{bmatrix} \times \begin{bmatrix} 1 & 0 & 0 \\ 0 & e^{i\phi} & 0 \\ 0 & 0 & 1 \end{bmatrix} \times \begin{bmatrix} \frac{\sqrt{2}}{2} & i\frac{\sqrt{2}}{2} & 0 \\ i\frac{\sqrt{2}}{2} & \frac{\sqrt{2}}{2} & 0 \\ 0 & 0 & 1 \end{bmatrix}$$

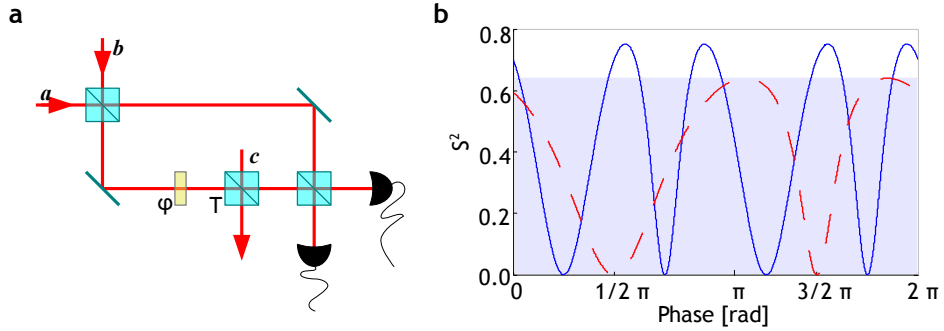


Figure 3.11: (a) MZI with a further beam splitter on the sensing arm, which models the interaction with a loss mode, i.e. the losses suffered in crossing the microchannel. (b) Phase sensitivity \mathcal{S}^2 as a function of the phase shift induced by the sample in the sensing arm for two-photon (solid blue curve) and single photon (dashed red curve) interference. Shaded area represents the phase sensitivity region achievable with classical measurements.

the probability of detecting a $|11\rangle$ state at the output when the input state is $|11\rangle$ (considering the three modes, this state correspond to $|110\rangle$). Under the hypothesis of unitary detection efficiency, we have:

$$p_{|11\rangle} = \left| \frac{t^2 e^{j2\phi} + 1}{2} \right|^2 = \frac{1}{2} \left(\frac{1 + T^2}{2} \right) (1 + \mathcal{V}_{2\text{ph}} \cos 2\phi) \quad (3.15)$$

where the fringe visibility is $\mathcal{V}_{2\text{ph}} = \frac{2T}{1+T^2}$.

An analogous procedure can be applied to the single photon case, providing:

$$p_{|10\rangle} = \frac{1}{2} \left(\frac{1 + T}{2} \right) (1 + \mathcal{V}_{1\text{ph}} \cos \phi) \quad (3.16)$$

where $\mathcal{V}_{1\text{ph}} = \frac{2\sqrt{T}}{1+T}$. In both cases (more strongly in the two-photon case) the fringe visibility is affected by the losses.

From the detection probabilities in Eq.(3.15) and (3.16), assuming the ideal case of binomial photon detection statistics, one can calculate[87] the phase uncertainty $\delta\phi$ of the measurement. A comparison with the standard quantum limit is given by the ratio $\mathcal{S} = \delta\phi/\delta\phi_{\text{SQL}}$, where $\delta\phi_{\text{SQL}} = 1/\sqrt{N}$ is the phase uncertainty at the standard quantum limit. If $\mathcal{S} > 1$ this limit is potentially beaten.

Figure 3.11b shows the calculated values of \mathcal{S}^2 for quantum (two-photon) and classical (single-photon) measurements. Experimental values for transmission T , $\mathcal{V}_{1\text{ph}}$ and $\mathcal{V}_{2\text{ph}}$ are considered. It can be noted that in this case the quantum measurements do not overcome the standard quantum limit. However, it should also be observed that in this case not even the classical measurement is able to reach it. Indeed, a more meaningful comparison could be between the sensitivity \mathcal{S}^2 obtainable for quantum and classical measurements, but both performed in the same conditions, i.e. in the same sensing chip. As shown in Figure 3.11b, the presence of those losses do not prevent the quantum measurement to yield an improved phase sensitivity with respect to the classical one.

A more detailed calculation which involves all losses and inefficiencies would show that in this experiment the quantum measurement is actually less sensitive than the classical one. This is mainly due to the inefficiency of single-photon sources and detectors. It can be observed that the latter limitation affects all the current experiments of quantum metrology with single photons, so that no demonstration of *real* supersensitivity has been reported yet in N00N state interferometry. However, the discussion above shows that using better sources, detectors and connections, non-classical enhancements in sensitivity could be achieved in this optofluidic device. Hence, this is a valid architecture for investigating the possibilities of quantum interferometry in biological applications.

Chapter 4

Integrated optical quantum computing and simulation

This Chapter reports on four experiments involving the development of photonic structures for different applications in the quantum information and optical simulation fields.

The first three experiments have been conducted in collaboration with the Quantum Optics group of the Physics Department of La Sapienza University of Rome. In particular, in Section 4.1 the development of a directional coupler, which acts as a filter for polarization entangled photons, is reported. In Section 4.2 the realization of an integrated CNOT gate for polarization encoded qubits is described, based on partially polarizing directional couplers. Section 4.3 concerns the development of a specific polarization insensitive network of directional couplers, which enables on-chip implementation of discrete quantum walk of photon entangled states, with both bosonic and fermionic symmetry. Each of these Sections is further divided in three Subsections: the first one describes the main ideas behind the experiment, conceived in close collaboration with the University of Rome; the second one discusses the development and fabrication of the different photonic devices, which was the main focus of my research activity; the third one summarizes the results of the devices characterization with quantum light, performed in Rome, to which I also participated.

Finally, the last section of the Chapter (Section 4.4) regards the design and realization of a photonic structure for simulation of quantum phenomena with classical light. In particular, the simulation of the deep strong coupling regime of the Jaynes-Cummings dynamics was addressed.

4.1 Polarization entangled states measurement on a chip

4.1.1 The idea behind the experiment

Entanglement filtering by a directional coupler

The capability to filter and analyze entangled states is of great interest in the field of quantum information. Qubits encoded in the Bell states basis¹ allow for example to harness non-locality effects and implement dense coding protocols[137].

A simple integrated circuit which enables filtering of the singlet Bell state is a polarization independent directional coupler. In the Heisenberg picture, the operation of such a device can be described as a transformation of the annihilation operators of the four optical modes involved (two polarizations per each spatial mode), which takes the form of the following matrix equation (see also Appendix A):

$$\begin{bmatrix} a'_H \\ b'_H \\ a'_V \\ b'_V \end{bmatrix} = \begin{bmatrix} t_H & i r_H & 0 & 0 \\ i r_H & t_H & 0 & 0 \\ 0 & 0 & t_V & i r_V \\ 0 & 0 & i r_V & t_V \end{bmatrix} \begin{bmatrix} a_H \\ b_H \\ a_V \\ b_V \end{bmatrix} \quad (4.1)$$

where a_X and b_X are the annihilation operators of the two input modes with polarization X , a'_X and b'_X are the annihilation operators of the output modes with polarization X , r_X and t_X are the beam splitter transmissivity and reflectivity for the polarization X ($|r_X|^2 + |t_X|^2 = 1$).

In general, injecting two-photon input states with one photon per spatial mode in the device can result in two photons output states with one photon per mode, which will give coincidence detection, or two photons in one of either modes. The probabilities of these different outcomes depend on the specific input state and on the beam splitter transmissivity and reflectivity. For example, injecting a couple of indistinguishable photons in a perfectly balanced beam splitter ($r = t = 1/\sqrt{2}$) will produce the Hong-Ou-Mandel[100] effect with vanishing probability of output coincidence detection.

If we limit ourselves to consider the subset of cases in which two photons are detected at different outputs of a polarization insensitive beam splitter ($r_H^2 = r_V^2 = R$ and $t_H^2 = t_V^2 = T = 1 - R$), the device operation on two polarization encoded qubits can be described as follows:

$$|\psi_{\text{OUT}}\rangle = U_{\text{BS}}|\psi_{\text{IN}}\rangle \quad (4.2)$$

¹Bell states for polarization entangled photons are defined as:

$$|\psi^\pm\rangle = \frac{|HV\rangle \pm |VH\rangle}{\sqrt{2}} \quad |\phi^\pm\rangle = \frac{|HH\rangle \pm |VV\rangle}{\sqrt{2}}$$

The states $|\psi^+\rangle, |\phi^+\rangle$ and $|\phi^-\rangle$ (triplet) have a symmetric expression, with respect to the exchange of the two photons. The state $|\psi^-\rangle$ (singlet) has on the contrary an antisymmetric expression.

with

$$U_{\text{BS}} = \begin{bmatrix} 1-2R & 0 & 0 & 0 \\ 0 & 1-R & -R & 0 \\ 0 & -R & 1-R & 0 \\ 0 & 0 & 0 & 1-2R \end{bmatrix} \quad (4.3)$$

for qubits encoded in the $(|V\rangle, |H\rangle)$ basis:

$$|\psi\rangle = c_{\text{HH}}|HH\rangle + c_{\text{HV}}|HV\rangle + c_{\text{VH}}|VH\rangle + c_{\text{VV}}|VV\rangle \quad (4.4)$$

On the other hand, if the qubits are encoded in the Bell basis:

$$|\psi\rangle = c_{\psi^+}|\psi^+\rangle + c_{\psi^-}|\psi^-\rangle + c_{\phi^+}|\phi^+\rangle + c_{\phi^-}|\phi^-\rangle \quad (4.5)$$

by applying the basis transformation, the beam splitter operation results:

$$U_{\text{BS,Bell}} = \begin{bmatrix} 1-2R & 0 & 0 & 0 \\ 0 & 1 & 0 & 0 \\ 0 & 0 & 1-2R & 0 \\ 0 & 0 & 0 & 1-2R \end{bmatrix} \quad (4.6)$$

It can be noted that, if the beam splitter is also perfectly balanced ($R = 1/2$), its operation is equivalent to the projector on the $|\psi^-\rangle$ singlet Bell state:

$$U_{\text{BS,Bell}} = \begin{bmatrix} 0 & 0 & 0 & 0 \\ 0 & 1 & 0 & 0 \\ 0 & 0 & 0 & 0 \\ 0 & 0 & 0 & 0 \end{bmatrix} = |\psi^-\rangle\langle\psi^-| \quad (4.7)$$

Hence, by post-selection of the coincidence events, which is a common technique in quantum optics experimental protocols, discrimination between the symmetric and antisymmetric subspaces can be achieved.

4.1.2 Development of the photonic device

4.1.2.1 Low-birefringence waveguides

A directional coupler consists of two waveguides brought close at a distance d for a length L called interaction length (see Figure 4.1). In this region the two waveguides couple by evanescent field and exchange optical power, according to the coupled-mode theory[42].

In analogy to bulk beam splitters, power reflectivity R and transmissivity T of a the directional coupler can be conveniently defined, referring to Figure 4.1 : launching light into port IN1, $R = P_{\text{OUT1}}/(P_{\text{OUT1}} + P_{\text{OUT2}})$ and $T = 1 - R = P_{\text{OUT2}}/(P_{\text{OUT1}} + P_{\text{OUT2}})$, respectively (P indicates the optical power). The symmetry of the device guarantees that the same relations hold when light is launched into port IN2, by simply inverting the two indices. For a coupler made of two identical waveguides, it holds:

$$R = |r|^2 = \cos^2(\kappa L) \quad T = |t|^2 = \sin^2(\kappa L) \quad (4.8)$$

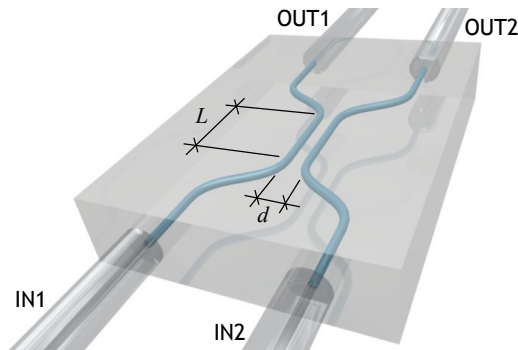


Figure 4.1: Schematic of a directional coupler. d is the distance between the waveguides in the interaction region and L is the interaction length.

where κ is the coupling coefficient between the two waveguides, r and t are the amplitude reflectivity and transmissivity.

The coefficient κ depends on the overlap integral between the modes of the two waveguides, which in general can differ for the two polarizations, in presence of waveguide birefringence. Using waveguides with the lowest possible birefringence enables to fabricate couplers with polarization insensitive behaviour. Furthermore, waveguide birefringence causes polarization-mode dispersion which can remove photon indistinguishability. Decoherence of the large bandwidth photon states typically employed in quantum optics experiments may also be induced. As a consequence, birefringent waveguides are not suitable for operation with polarization encoded photonic qubits.

It should also be noted that present demonstrations of integrated photonic quantum circuits are mostly based on silica-on-silicon waveguides, which suffer from intrinsic birefringence, typically reported[138] on the order of 4×10^{-4} . In fact, these waveguides are fabricated in a doped silica multilayer structure on a silicon substrate, and this causes material stress due to lattice mismatches between the different layers. Techniques for reducing this stress and the induced birefringence have been proposed, but they pose serious difficulties in terms of fabrication complexity and reproducibility[139].

Substrate choice In order to minimize the waveguide birefringence, a correct choice of the substrate is crucial. For example, quantum operation with fixed polarization photons has been reported in waveguides fabricated by femtosecond laser in fused silica[101]. However, irradiation of fused silica by femtosecond pulses is known to create birefringent self-aligned nanogratings, especially when high refractive index changes are required[140, 16], as in the case of curved waveguides.

For this reason, we chose to employ a borosilicate glass (EAGLE2000, Corning) as a substrate, where the formation of birefringent nanogratings has never been observed[13]. In addition, high repetition rate laser pulses induce isotropic thermal diffusion and melting of the material around the focal point, helping to circularize the waveguide cross-section without the need for any shaping of the

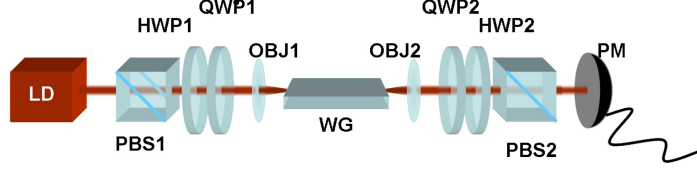


Figure 4.2: Setup for birefringence measurement. LD: laser diode emitting at 806 nm wavelength and with bandwidth $\Delta\lambda = 2$ nm. PBS1 and PBS2: polarizing beam splitters. HWP1 and HWP2: half-wave plates. QWP1 and QWP2: quarter-wave plates. OBJ1 and OBJ2: objectives for injecting light into the waveguide (WG) and collecting transmitted light at the output. PM: power meter.

writing laser beam (see also Section 1.1.2.2 and Ref. [24]). A symmetric waveguide cross-section is important because some modal birefringence can be induced also by waveguides asymmetry even in absence of any bulk birefringence[141]. A simpler writing setup without beam-shaping optics may also be preferable for a better reproducibility of the fabricated devices, since there are less optical elements whose day to day slight misalignment affects the fabrication conditions. Another advantage of the use of this substrate is that low loss waveguides can be produced with very high writing speeds ($10 \div 50$ mm/s).

Birefringence measurement The birefringence of the fabricated waveguides is characterized using the setup depicted in Figure 4.2. This setup is similar to the one described in Section 2.2.4 for the polarization dependent waveguide characterization, except for the addition of a polarization analysis section (QWP2 + HWP2 + PBS2), cascaded to the collection objective.

In order to perform the measurement, light with six different polarization states is injected into the waveguide, namely:

$$\begin{aligned}
 |H\rangle & & |V\rangle \\
 |+\rangle &= \frac{|H\rangle + |V\rangle}{\sqrt{2}} & |-\rangle &= \frac{|H\rangle - |V\rangle}{\sqrt{2}} \\
 |L\rangle &= \frac{|H\rangle + i|V\rangle}{\sqrt{2}} & |R\rangle &= \frac{|H\rangle - i|V\rangle}{\sqrt{2}}
 \end{aligned}$$

The states are selected by rotating HWP1 and, if necessary, by adding and rotating also QWP1. For each input state the output state is projected on the same six polarization states by acting on the waveplates HWP2 and QWP2 and measuring the power transmitted after PBS2. These projections allow to calculate the normalized Stokes vector for the output state, which defines completely the

polarization state, by the following:

$$\vec{S} = \begin{bmatrix} 1 \\ (P_H - P_V) / (P_H + P_V) \\ (P_+ - P_-) / (P_+ + P_-) \\ (P_L - P_R) / (P_L + P_R) \end{bmatrix} \quad (4.9)$$

where each P_X is the power measured for the projection on the state X .

A generic linear optical element modifies the input polarization state \vec{S}_{IN} by means of a matrix relation:

$$\vec{S}_{\text{OUT}} = M\vec{S}_{\text{IN}} \quad (4.10)$$

M is the so called Mueller matrix associated to the optical element, \vec{S}_{OUT} is the output Stokes vector. The waveguide can be assumed to be analogous to a uniaxial birefringent material with the optical axis tilted by an angle θ , which introduces a dephasing δ between the two polarizations. The latter dephasing δ is proportional to the difference between ordinary and extraordinary refractive indices. Such an optical element yields a Mueller matrix of the form:

$$M_{\text{WG}} = \begin{bmatrix} 1 & 0 & 0 & 0 \\ 0 & \cos^2 2\theta + \sin^2 2\theta \cos \delta & \sin 2\theta \cos 2\theta (1 - \cos \delta) & -\sin 2\theta \sin \delta \\ 0 & \sin 2\theta \cos 2\theta (1 - \cos \delta) & \sin^2 2\theta + \cos^2 2\theta \cos \delta & \cos 2\theta \sin \delta \\ 0 & \sin 2\theta \sin \delta & -\cos 2\theta \sin \delta & \cos \delta \end{bmatrix} \quad (4.11)$$

A matrix of this form is thus fitted by a least-squares method in order to give the experimental output Stokes vectors for the corresponding input states (whose Stokes vector is known). θ and δ are the free parameters in the fitting process. However, it has to be noted that a single measurement of δ cannot be used for direct determination of birefringence, since ambiguity occurs with multiple-order birefringence. Thus, the sample is cut to different lengths and all the measurements described above, together with the fitting to calculate θ and δ , are repeated for each length. This allows to remove the ambiguity and finally obtain the actual waveguide birefringence.

4.1.2.2 Directional coupler geometry optimization

The directional coupler geometry, i.e. its characteristic dimensions d and L (Figure 4.1), has been optimized in order to make the structure less sensitive to possible differences in the coupling coefficients κ for the two polarizations.

Interaction length A first consideration regards the interaction length L . Since the transfer function of the directional coupler is periodic, several values of L would equally give the same power repartition (which in our case should be balanced). We can study the influence of small differences in κ on the output power by differentiating the transmission expression in Eq. (4.8) with respect to κ :

$$\frac{\partial T}{\partial \kappa} = L \sin(2\kappa L) = L \quad (4.12)$$

since for a balanced directional coupler $\kappa L = \pi/4$. The output power sensitivity to variations in κ is proportional to L ; for this reason having a short interaction length is overall preferable.

Distance between coupled waveguides The dependence of the coupling coefficient κ on the distance d between the coupled waveguides can be approximated by an exponential law[59]:

$$\kappa = C e^{-\frac{d}{d_0}} \quad (4.13)$$

where d_0 is related to the mode dimension and waveguide properties, and C is a constant. A different κ for the two polarizations can be actually modelled by a different d_0 for the H and V polarized modes. It is useful to analyze how variations in d_0 affect the resulting coupling coefficient κ :

$$\frac{1}{\kappa} \frac{\partial \kappa}{\partial d_0} = \frac{d}{d_0^2} \quad (4.14)$$

where the derivative $\partial \kappa / \partial d_0$ has been divided by κ because one is interested in relative variations. It can be observed that the relative variations of κ are proportional to d . Thus, small values of interwaveguide distance will make the coupling less sensitive to birefringence.

Another point that can be discussed is the sensitivity to geometric fabrication tolerances. This is not related to the polarization behaviour, but it is useful to know if certain coupler designs are more or less sensitive to errors or fluctuations in the distance d . To this aim, one can evaluate:

$$\frac{1}{\kappa} \frac{\partial \kappa}{\partial d} = -\frac{1}{d_0} \quad (4.15)$$

This expression is not depending on d , thus the influence of geometric fabrication errors which alters the distance d is always the same for every value of d . At least, no specific drawbacks are found in building a coupler with a small interwaveguide distance, as appears preferable from the previous discussions.

Fabrication parameters	
Substrate	EAGLE2000
Laser system	Yb:KYW cav. dump.
Wavelength	1030 nm
Repetition rate	1 MHz
Pulse energy	220 nJ
Translation speed	40 mm/s
Objective	0.6 NA

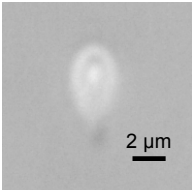


Table 4.1: Waveguide writing parameters. Microscope image of the waveguide cross-section is also shown.

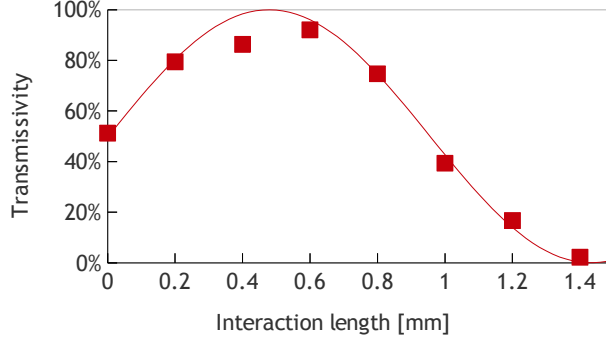


Figure 4.3: Typical experimental transmission of directional couplers fabricated with different interaction lengths, measured at 806 nm wavelength for the polarization H. The continuous line is a fitting with a \sin^2 curve.

4.1.2.3 Fabrication details

The waveguides were fabricated in Corning EAGLE2000 borosilicate glass using the Yb:KYW cavity-dumped laser system (see Section 2.1.1). The optimized fabrication parameters for single mode guiding at 806 nm wavelength are shown in Table 4.1. All devices were realized buried 170 μm under the glass surface.

At the operation wavelength, the waveguides support a single gaussian mode of circular profile with $\sim 8 \mu\text{m}$ $1/e^2$ diameter. Coupling losses with single mode fibers (Thorlabs SM800-5.6-125) have been estimated as 0.7 dB. Measured propagation losses are 0.5 dB/cm. Additional bending losses are lower than 0.3 dB/cm for the 30 mm bending radius adopted.

The waveguide birefringence value was measured with the method described in Section 4.1.2.1 to be $B = n_{\text{eff, TM}} - n_{\text{eff, TE}} = 7 \times 10^{-5}$, with the fast axis aligned with the TE polarization. This residual birefringence can be attributed to ellipticity of the waveguide profile, notwithstanding the thermal mechanism of the waveguide formation. However, it is worth observing that this value is about one order of magnitude lower than the typical birefringence value of silica-on-silicon waveguides.

For the reasons discussed in Section 4.1.2.2, we fabricated directional couplers with the smallest possible interwaveguide distance, which was found experimentally to be $d = 7 \mu\text{m}$. In fact, for smaller distances insertion losses of the device were found to increase, likely because the writing process of the second waveguide damages the first waveguide already written. The waveguide separation at the input and output ports of the device is 250 μm .

Several directional couplers have been fabricated varying the interaction length L , spanning the range $0 \div 1000 \mu\text{m}$ (see Figure 4.3) and the corresponding transmissivities and reflectivities were measured. The length $L = 0 \mu\text{m}$ yielded a transmissivity of about 50% at 806 nm wavelength. Indeed, the possibility to achieve a 50% splitting with no straight segment is due to the coupling between the modes already occurring in the curved parts of the two approaching and

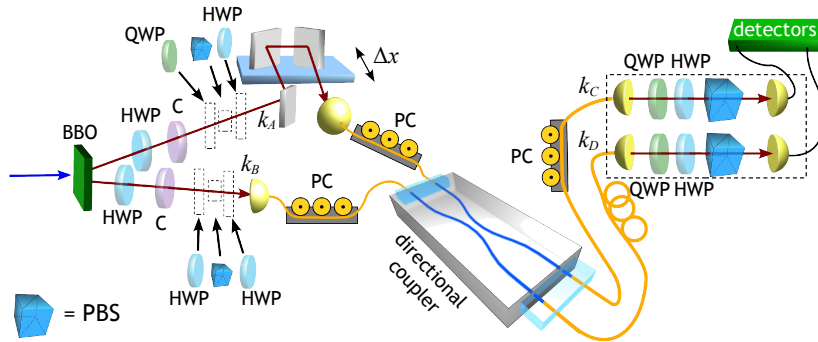


Figure 4.4: Setup for the characterization of the directional coupler with polarization-entangled photons. The parametric down-conversion photon source, the fiber-pigtailed directional coupler and the detection system are shown. Polarizing beam splitters (PBS), half-(HWP) and quarter-(QWP) waveplates are optionally inserted in the paths k_A and k_B to prepare different input states. A delay line Δx in the k_A arm enabled the variation of the temporal delay between the two input photons. The components shown in the dashed box are inserted only during the tomography measurements of the filtered state. Other elements are C: compensators for the birefringence of the BBO crystal, PC: polarization controllers.

departing waveguides.

Precisely, the transmissivity of the directional coupler with $L = 0 \mu\text{m}$ was measured to be $50.8\% \pm 0.2\%$ for H polarization and $41.9\% \pm 0.2\%$ for V polarization. Input and outputs of this device were fiber coupled (Section 2.3) for more reliable operation and tested with quantum light.

4.1.3 Quantum characterization

Measurements with entangled photons

Characterization of the device by non-classical light was carried out using the setup shown in Figure 4.4.

First experiments tested the Hong-Ou-Mandel interference[100] by injecting different separable states in the directional coupler. Separable states can be obtained by placing two polarizing beam splitters in the k_A and k_B modes. Figure 4.5a reports the coincidence counts as a function of the reciprocal delay Δx of the two input photons in the state $|HH\rangle$. Measured visibilities² for the Hong-Ou-Mandel dips are $\mathcal{V} = 0.937 \pm 0.009$ for input state $|HH\rangle$, $\mathcal{V} = 0.926 \pm 0.012$ for $|VV\rangle$ and $\mathcal{V} = 0.954 \pm 0.011$ for $|++\rangle$.

Hong-Ou-Mandel experiments were then repeated injecting entangled states (see Figure 4.5b). Whereas for the symmetric triplet states the typical dip is observed, for the singlet antisymmetric states a peak appears instead. This is the filtering operation discussed in Section 4.1.1: in the coincidence subspace the symmetric states are suppressed (dip) and only the antisymmetric state is efficiently transmitted (peak). The measured visibilities are $\mathcal{V}_{|singlet\rangle} = 0.930 \pm 0.005$ and $\mathcal{V}_{|triplet\rangle} = 0.929 \pm 0.005$. These high visibility values testify the high quality of the non-classical interference in the integrated device.

²See definition in Footnote 4 at pag. 51 .

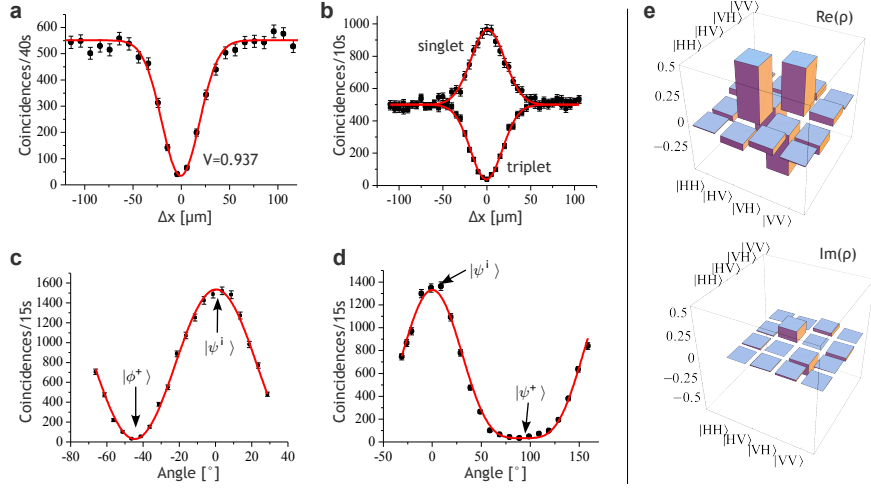


Figure 4.5: (a) Hong-Ou-Mandel dip with input state $|\text{HH}\rangle$. (b) The peak or dip corresponding to the singlet or triplet input state. (c) Fringe pattern obtained by rotating the HWP on mode k_B . (d) Fringe pattern obtained by rotating the QWP on mode k_A . All curves represent experimental fits. (e) Quantum state tomography of a filtered singlet state on the two output modes k_C and k_D . The real and imaginary part of the experimental density matrix are shown.

To further benchmark the directional coupler behaviour with entangled states, further experiments were conducted. The temporal delay was set at $\Delta x = 0$ and the source was tuned to generate the entangled state $|\psi^+\rangle$. By inserting on mode k_B a half waveplate with the optical axis oriented at an angle θ with respect to the vertical direction, it is possible to generate the states:

$$-\cos 2\theta|\psi^-\rangle + \sin 2\theta|\phi^+\rangle \quad (4.16)$$

In this case, the expected coincidence rates between detectors D_C and D_D after the beam splitter is $\mathcal{N}_0[1 + \tilde{\mathcal{V}} \cos 4\theta]$, where \mathcal{N}_i is a constant. The experimental results are shown in Figure 4.5c, yielding a visibility $\tilde{\mathcal{V}} = 0.962 \pm 0.018$.

Then, the source was tuned to generate $|\psi^i\rangle = \frac{1}{\sqrt{2}}(|H\rangle_A|V\rangle_B - i|V\rangle_A|H\rangle_B)$. By adding a quarter waveplate (QWP) rotated by an angle θ' on the mode k_A , it is possible to obtain the state:

$$\cos^2 \theta'|\psi^-\rangle - i \sin^2 \theta'|\psi^+\rangle + \frac{e^{-i\frac{\pi}{4}}}{\sqrt{2}} \sin 2\theta'|\phi^i\rangle \quad (4.17)$$

In this case it can be shown that the expected coincidence rate follows a $\cos^4 \theta'$ curve. Figure 4.5d shows the experimental fringe pattern, which displays a visibility $\mathcal{V} = 0.951 \pm 0.008$.

These results demonstrate the high overlap between the interfering modes k_A and k_B and show that this integrated directional coupler may be used as an appropriate tool for the manipulation of polarization encoded qubit.

Finally, the capability of the directional coupler to project a two-photon states on the singlet subspace was characterized in more detail. The separable state

$|H\rangle_A \otimes |V\rangle_B$ was injected and the quantum state tomography[142] of the output state, conditioned to the detection of the two photons in different outputs, was performed. The experimental density matrix ρ_{CD} , shown in Figure 4.5e, exhibits a high fidelity to the singlet state ($\mathcal{F} = 0.929 \pm 0.007$).

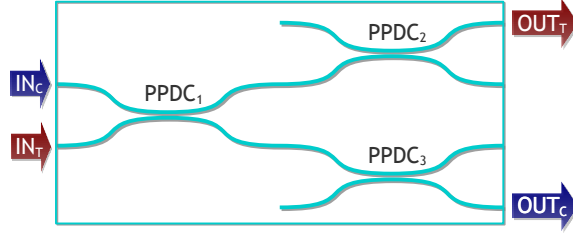


Figure 4.6: Schematic of a CNOT gate build by three PPDCs. IN_C , IN_T are the input ports for the control and target qubit respectively. OUT_C , OUT_T are the output ports for the control and target qubit respectively.

4.2 Integrated photonic CNOT gate for polarization encoded qubits

4.2.1 A CNOT gate with partially polarizing directional couplers

In Section 4.1 it has been shown experimentally how femtosecond laser written waveguides can support polarization encoded qubits. In particular, reliable entanglement filtering has been reported by a practically polarization-insensitive directional coupler. Anyway, the effective manipulation of polarization encoded photonic qubits by integrated optical circuits requires the development of more complex linear optics quantum gates, which are based on polarization *sensitive* integrated components.

Incidentally, it can be observed that little work is reported in literature regarding polarization dependent photonic components fabricated by femtosecond lasers. Most work regards the study of birefringent structures fabricated in fused silica, exploiting the laser induced birefringent nanogratings. Anyway, as already pointed out in Section 4.1.2.1, this kind of waveguides may exhibit an excessive birefringence which would affect coherence of polarization encoded qubits.

We address the realization of an integrated CNOT quantum gate for polarization encoded qubits, whose importance for quantum computation purposes has been discussed in Section 1.3.1.2. We choose, due to its simplicity, a scheme analogous to that of Ref. [96] (see also Figure 1.8). The bulk optics scheme consists of only three partially polarizing beam splitters. Quantum interference between the two input qubits happens on the first beam splitter, while the other two have simply the function to attenuate one polarization with respect to the other. In an integrated optics approach, the partially polarizing beam splitters are to be replaced by partially polarizing directional couplers (PPDCs), with different transmissivities and reflectivities for the two polarizations, disposed in a circuit as in Figure 4.6.

Injecting in the gate a generic two-qubit state:

$$|\psi\rangle = c_{HH}|H\rangle_C|H\rangle_T + c_{HV}|H\rangle_C|V\rangle_T + c_{VH}|V\rangle_C|H\rangle_T + c_{VV}|V\rangle_C|V\rangle_T \quad (4.18)$$

will result[96] in an output state (limited, as usual, to the subset of coincidence

photon detection):

$$\begin{aligned}
|\psi_{out}\rangle = & (c_{HH}t_H^2 a_H b_H - c_{HH}r_H^2 a_H b_H) |H\rangle_C |H\rangle_T + \\
& + (c_{HV}t_H t_V a_H b_V - c_{VH}r_V r_H a_H b_V) |H\rangle_C |V\rangle_T + \\
& + (c_{VH}t_V t_H a_V b_H - c_{HV}r_H r_V a_V b_H) |V\rangle_C |H\rangle_T + \\
& + (c_{VV}t_V^2 a_V b_V - c_{VV}r_V^2 a_V b_V) |V\rangle_C |V\rangle_T
\end{aligned} \tag{4.19}$$

where t_X and r_X are transmission and reflection amplitudes for polarization X on the first directional coupler (PPDC₁) a_X and b_X are transmission amplitudes for polarization X on the directional couplers PPDC₂ and PPDC₃. In both Eqs. (4.18) and (4.19), the subscripts C and T identify the control qubit and the target qubit.

Using directional couplers with the following properties:

$$\begin{aligned}
|r_V|^2 = |a_H|^2 = |b_H|^2 = \frac{1}{3} & & |t_V|^2 = \frac{2}{3} \\
|r_H|^2 = |a_V|^2 = |b_V|^2 = 1 & & |t_H|^2 = 0
\end{aligned} \tag{4.20}$$

one has:

$$|\psi_{out}\rangle = -\frac{1}{3} (c_{HH}|H\rangle_C |H\rangle_T + c_{HV}|H\rangle_C |V\rangle_T + c_{VH}|V\rangle_C |H\rangle_T - c_{VV}|V\rangle_C |V\rangle_T) \tag{4.21}$$

which is, apart from a common factor, the operation of a C-phase gate, as defined in Eq. (1.5). As already discussed, the CNOT operation is readily achieved by a change of basis.

4.2.2 Development of the photonic device

4.2.2.1 How to build a partially polarizing directional coupler

A directional coupler made by slightly birefringent waveguides is typically characterized by coupling coefficients κ_H and κ_V which slightly differ for the two polarizations. For short interaction lengths L , this will just produce small differences in the directional coupler transmissivities (see Section 4.1.2.2):

$$T_H = |t_H|^2 = \sin^2(\kappa_H L) \quad T_V = |t_V|^2 = \sin^2(\kappa_V L) \tag{4.22}$$

Anyway, if longer interaction lengths are adopted, covering a few beating periods, it is possible to strongly enhance the difference in the polarization behaviour of the device, as shown in Figure 4.7. Polarizing or partially polarizing directional couplers with finely tailored characteristics can be realized by this approach. In particular, by a judicious choice of the interaction lengths, PPDCs which satisfy the requirements (4.20) can be obtained.

4.2.2.2 Fabrication details

For the fabrication of partially polarizing directional couplers, following the ideas explained in the previous section, we employed the commercial HighQLaser FemtoREGEN system at 960 kHz repetition rate. This laser system has indeed comparable pulse characteristics with respect to the cavity dumped oscillator, but

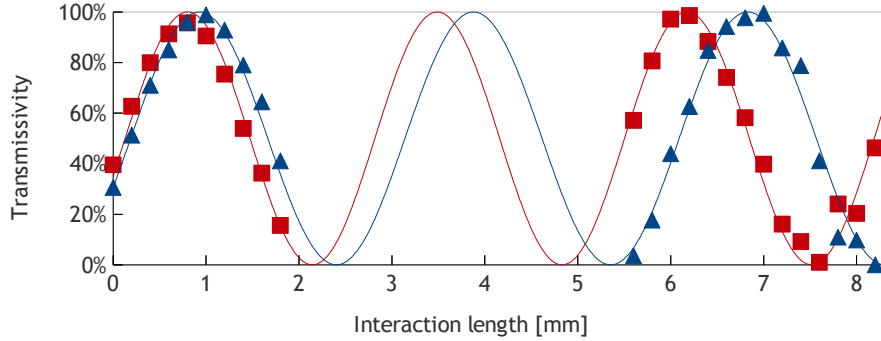


Figure 4.7: Experimental transmission of directional couplers fabricated with different interaction lengths, measured at 806 nm wavelength for both polarizations, H (*squares*) and V (*triangles*). The continuous lines are fittings with theoretical curves.

Fabrication parameters	
Substrate	EAGLE2000
Laser system	FemtoREGEN
Wavelength	1040 nm
Repetition rate	960 kHz
Pulse energy	240 nJ
Translation speed	20 mm/s
Objective	0.45 NA

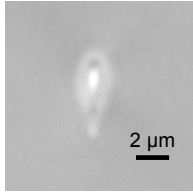


Table 4.2: Waveguide writing parameters used for the fabrication of the CNOT gate. Microscope image of the waveguide cross-section is also shown.

it provides better power stability. Waveguides with similar properties to those employed for the directional coupler described in Section 4.1 were indeed found for almost identical writing parameters (see Table 4.2): 240 mW writing power and 20 mm/s translation speed.

In order to calibrate the fabrication parameters, several directional couplers have been produced with different interaction lengths, ranging from 0 mm to 2 mm (Figure 4.3). The distance between the two waveguides in the interaction region was kept constant at 7 μm and bending radius of 30 mm was employed. This allowed to estimate the coupling coefficients for the two polarizations.

A second fabrication run was then performed, scanning L from 5.6 mm to 8.2 mm (Figure 4.3). It can be observed that for an interaction length $L_1 \simeq 7.4$ mm a device with $T_H = 0$ and $T_V = \frac{2}{3}$ is obtained, fulfilling the requirements for PPDC₁, whereas a length $L_2 \simeq 7$ mm provides $T_H = \frac{1}{3}$ and $T_V = 1$ and can be adopted for PPDC₂ and PPDC₃. Several CNOTs have been fabricated according to the schematic of Figure 4.6 with slightly different interaction lengths around the values of L_1 and L_2 to take into account possible fabrication imperfections. The footprint of each integrated CNOT is 500 $\mu\text{m} \times 3$ cm.

After characterization with a classical laser source, the device providing the best estimated performance has been selected. Parameters of this device are reported in the following table, compared to the ideal values:

	T_V		T_H	
	Exp.	Theo.	Exp.	Theo.
PPDC ₁	$(64 \pm 1)\%$	67%	$< 1\%$	0%
PPDC ₂	$(98 \pm 1)\%$	100%	$(43 \pm 1)\%$	33%
PPDC ₃	$(93 \pm 1)\%$	100%	$(27 \pm 1)\%$	33%

Despite the accurate calibration procedure, a difference of a few percent with respect to the desired values is observed. The reasons of such reproducibility problems are investigated in the following.

To improve the robustness and stability of the device, single-mode fiber arrays have been permanently bonded to the input and output ports.

4.2.2.3 Coupling coefficients and writing power: the laser stability issue

Fabrication of partially polarizing directional couplers has posed some issues regarding reproducibility, even though the obtained results do not prevent obtaining very high fidelity in the quantum gate operation, as it will be shown in Section 4.2.3. It is worth investigating in some more depth the origin of these difficulties.

We studied the dependence of the coupling coefficient from the laser writing power, to quantify the influence of small variations of the latter (which could be given by instabilities or noise) on the directional coupler behaviour. We fabricated several identical directional couplers, with dimensions $L = 7.5$ mm and $d = 7$ μ m, varying the writing power in the range $240 \div 270$ mW; the geometrical parameters are the same used for the couplers in the CNOT gate. The transmissivity of the directional couplers was measured for the polarization H, the coupling coefficient was retrieved and thus the dependence of the latter from the writing power was calculated. An approximately linear relation was found and the variation of coupling coefficient for unit power was estimated to be $\partial\kappa/\partial P_{wr} = 1 \times 10^{-2}$ mm⁻¹mW⁻¹ (Figure 4.8). The influence on these coupling variations on the transmissivity of the directional coupler depends on the position on the beating fringe:

$$\frac{\partial T}{\partial P_{wr}} = \frac{\partial T}{\partial \kappa} \frac{\partial \kappa}{\partial P_{wr}} = \frac{\partial \sin^2 \kappa L}{\partial \kappa} \frac{\partial \kappa}{\partial P_{wr}} = L \sin(2\kappa L) \frac{\partial \kappa}{\partial P_{wr}} \leq L \frac{\partial \kappa}{\partial P_{wr}} \quad (4.23)$$

In the worst case $\partial T/\partial P_{wr} = 7.5 \times 10^{-2}$ mW⁻¹, which means that a variation of 1 mW in the writing power can cause a variation of the transmissivity up to 7.5%. This must be compared to the writing power employed, which is 240 mW.

The declared stability of the laser system is 0.3%, which corresponds to about 0.7 mW over 240 mW. In the light of these observations, reproducibility issues in the fabrication of the directional couplers can be reasonably explained by small fluctuations in the laser power, and could be overcome with more stable laser sources.

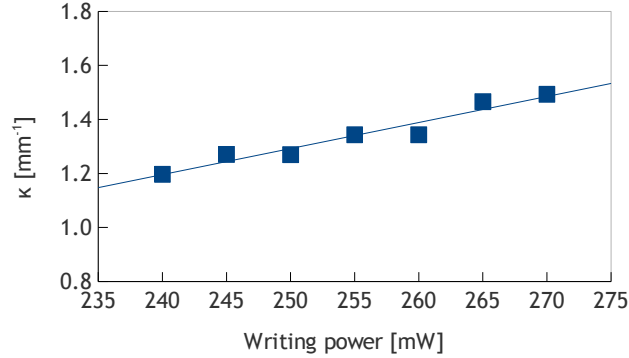


Figure 4.8: Retrieved coupling coefficient κ in couplers with interaction length $L = 7.5$ mm and $d = 7$ μm , as a function of the power of the writing laser beam.

4.2.3 Quantum characterization

4.2.3.1 Experimental truth table

A first important characterization of the integrated CNOT gate was the measurement of the experimental truth table. The setup shown in Figure 4.9 was adopted, which is similar to the one used for the characterization of the directional coupler in entanglement filtering (compare to Figure 4.4). In this case waveplate rotations were computer-controlled and programmable, to perform the measurements more efficiently. Temporal superposition of photon wavepackets on the first directional coupler of the CNOT was obtained by acting on the delay line DL.

The four states of the computational basis $|0\rangle_{\text{C}}|0\rangle_{\text{T}}$, $|0\rangle_{\text{C}}|1\rangle_{\text{T}}$, $|1\rangle_{\text{C}}|0\rangle_{\text{T}}$ and $|1\rangle_{\text{C}}|1\rangle_{\text{T}}$ were injected in the device and the probability of detecting each of them at the output was measured. Note that the polarization encoding basis for the control qubit (C) and for the target qubit (T) are different (see definitions (1.6)).

The obtained truth table is reported in Figure 4.10a. The measured fidelity of the logical basis[96] was calculated to be $\mathcal{F} = 0.940 \pm 0.004$. We can compare this value with the expected fidelity of the device $\mathcal{F} = 0.975 \pm 0.007$, estimated by taking into account the measured transmissivities of the partially polarizing directional couplers. The discrepancy between the experimental and expected fidelities can be attributed both to partial distinguishability of the photon wavepackets and non perfect compensation for the polarization rotation produced in the single mode optical fibers.

4.2.3.2 Transformation of entangled states

As it can be easily verified, the CNOT operator (Eq. (1.4)) transforms separable states into maximally entangled Bell states, and vice versa. In detail:

$$\begin{aligned} |\pm\rangle_{\text{C}}|0\rangle_{\text{T}} &\xleftrightarrow{\text{CNOT}} |\Phi^{\pm}\rangle \\ |\pm\rangle_{\text{C}}|1\rangle_{\text{T}} &\xleftrightarrow{\text{CNOT}} |\Psi^{\pm}\rangle \end{aligned}$$

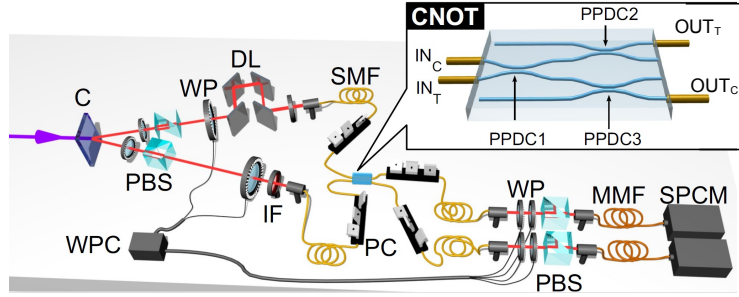


Figure 4.9: Sketch of the experimental setup for the characterization of the quantum behaviour of the integrated CNOT gate. Photon pairs at wavelength $\lambda = 806$ nm are generated via spontaneous parametric down conversion in β -barium borate crystal (C) pumped by a CW diode laser. Photon polarization states are prepared by using polarizing beam splitters (PBS) and waveplates (WPs). A delay line (DL) is inserted to control the temporal overlap of the photons, which are then coupled to single mode fibers (SMFs) and injected into the integrated CNOT gate. Interference filters (IFs) determine the photon bandwidth $\Delta\lambda = 6$ nm. The polarization state of the qubits emerging from the chip is analyzed by standard analysis setups (WP + PBS). Photons are then delivered to single photon counting modules (SPCM) through multimode fibers (MMFs) and coincidences between the two channels are measured. Polarization controllers (PCs) are used before and after the CNOT device to compensate polarization rotations induced by the fibers. A waveplate controller (WPC) drives the motorized waveplates to automatize the measurements.

where $|\pm\rangle = (|0\rangle \pm |1\rangle) / \sqrt{2}$.

We experimentally verified this behaviour by injecting into the device the separable states above reported and measuring a set of observables in order to obtain a tomographic reconstruction of the density matrices of the output states. Figure 4.10b shows the experimental tomographic reconstruction of the Bell state $|\Phi^+\rangle$, obtained by injecting the separable state $|+0\rangle$. Figure 4.10c reports, for each separable input state, the output state projection on the Bell basis, i.e. the probability to generate the different Bell states. Fidelities of the output density matrices with respect to the corresponding Bell states are remarkably high: $\mathcal{F}_{|\Phi^+\rangle} = 0.930 \pm 0.014$, $\mathcal{F}_{|\Psi^+\rangle} = 0.939 \pm 0.008$, $\mathcal{F}_{|\Phi^-\rangle} = 0.900 \pm 0.006$, $\mathcal{F}_{|\Psi^-\rangle} = 0.877 \pm 0.011$. The average fidelity is: $\mathcal{F}_{Bell} = 0.912 \pm 0.005$.

The four Bell states were then prepared at the input and injected in the CNOT and the output states were characterized as before, to check the inverse operation. The projection of the output states on the separable state basis is reported in Figure 4.10d. This inverse operation can be exploited to discriminate the four Bell states. The discrimination probability is 0.877 ± 0.007 , slightly lower than the previous fidelities due to imperfections in the entanglement source.

4.2.3.3 Quantum tomography of the CNOT gate

A complete characterization of the quantum behaviour of the device was provided by carrying out the quantum process tomography[143]. This consists in preparing the photons in a complete set of input basis states, and characterizing the outputs by projections on this same basis.

A generic quantum process \mathcal{E} acting on a two-qubit density matrix ρ , can be expressed as $\mathcal{E}(\rho) = \sum_{m,n=0}^{15} \chi_{mn} \Gamma_m \rho \Gamma_n^\dagger$ where the operators Γ_m are defined as

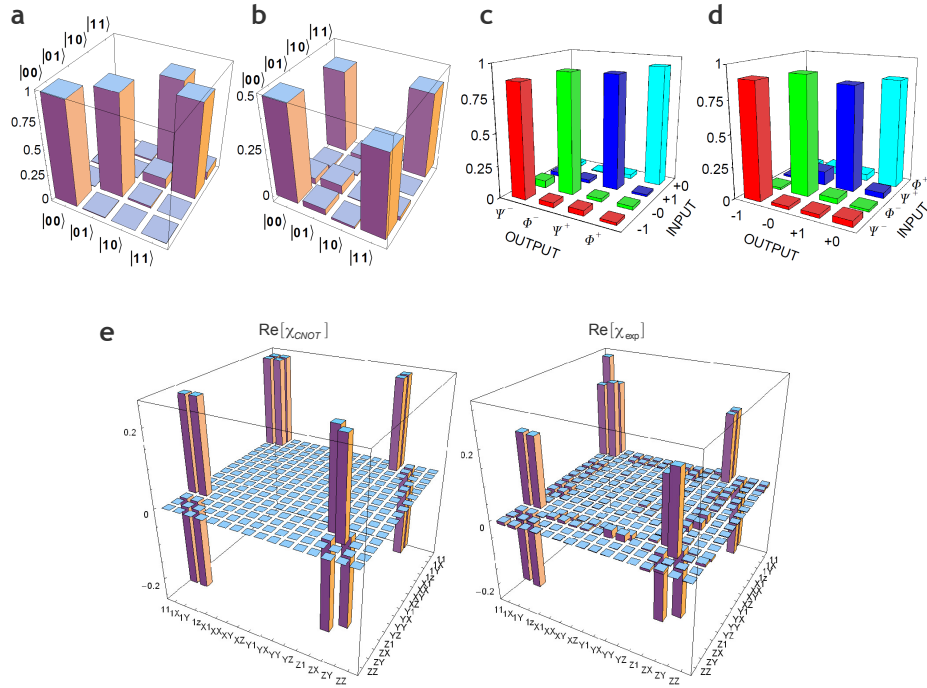


Figure 4.10: (a) Measured truth table. (b) Experimental tomographic reconstruction of the Bell state $|\phi^+\rangle$ obtained by injecting the separable state $|+0\rangle$ in the CNOT. (c) Measured probabilities of the output Bell states corresponding to the different input separable states. (d) Measured probabilities of the output separable states corresponding to the different input Bell states. (e) (right) Ideal χ_{CNOT} and (left) experimental χ_{exp} matrices (real part) obtained from the quantum process tomography of the CNOT gate. The imaginary part is negligible. X, Y and Z correspond to Pauli matrices σ_1 , σ_2 and σ_3 , respectively.

tensor product of Pauli matrices $\{\Gamma_m \equiv \sigma_i \otimes \sigma_j\}$, $i, j = 0, \dots, 3$, $m = 0, \dots, 15$.

The reconstructed 16×16 matrix χ_{exp} is shown in Figure 4.10e. A figure of merit of the gate is the process fidelity[144] with the ideal CNOT gate, which was calculated to be $\mathcal{F}_{\text{exp}} = 0.906 \pm 0.003$.

4.3 Experimental simulation of discrete quantum walk of bosons and fermions

4.3.1 The idea behind the experiment

Simulating bosons and fermions with entangled states

The basic idea of this experiment is that the evolution of two identical bosons and fermions undergoing a quantum walk can be simulated precisely by using two entangled photons (i.e. two entangled bosons) and changing the symmetry of the entangled state.

The different bunching-antibunching behaviour of symmetric and antisymmetric entangled states has been experimentally observed also in the entanglement filtering experiment described in Section 4.1. This analogy can be extended rigorously to complex evolutions of bosons and fermions, such as quantum walks, as follows.

Consider a generic particle, described by the creation and annihilation operators a and a^\dagger . If the particle is injected at mode $|J\rangle$, with input state $a_J^\dagger|0\rangle$, the quantum walk performs a unitary transformation on the creation operator, namely

$$a_J^\dagger \rightarrow \sum_K U_{JK} a_K^\dagger \quad (4.24)$$

Consider now the evolution of the following two-photon polarization entangled states. We assume that the creation operators of vertically and horizontally polarized photons (v^\dagger and h^\dagger , respectively) undergo exactly the same unitary transformation (4.24).

$$|\Psi_{IJ}^\pm\rangle = \frac{h_I^\dagger v_J^\dagger \pm h_J^\dagger v_I^\dagger}{\sqrt{2}} |0\rangle \rightarrow \frac{1}{\sqrt{2}} \sum_{K,L} (U_{IK} U_{JL} \pm U_{JK} U_{IL}) h_K^\dagger v_L^\dagger |0\rangle \quad (4.25)$$

The probability of coincidence detection of two photons in the modes K and L , without measuring the polarization, must be calculated taking into account both the indistinguishable events $h_K^\dagger v_L^\dagger |0\rangle$ and $h_L^\dagger v_K^\dagger |0\rangle$, for $L \neq K$ and only one event $h_K^\dagger v_K^\dagger |0\rangle$ in the case $L = K$; thus:

$$p_\pm(I, J; K, L) = \begin{cases} |U_{IK} U_{JL} \pm U_{JK} U_{IL}|^2 & \text{for } L \neq K \\ \frac{1}{2} |U_{IK} U_{JL} \pm U_{JK} U_{IL}|^2 & \text{for } L = K \end{cases} \quad (4.26)$$

It is interesting to compare the previous expression to the one obtained for a quantum walk of a couple of identical bosons, characterized by the creation operators b_I^\dagger and b_J^\dagger , and of a couple of identical fermions, characterized by the creation operators f_I^\dagger and f_J^\dagger .

Given the commutation rules for bosons and fermions³ the initial two-particle

³For identical particles described by creation and annihilation operators a^\dagger and a , respec-

input state can be rewritten, in the two cases, as follows:

$$b_I^\dagger b_J^\dagger |0\rangle = \frac{1}{2} (b_I^\dagger b_J^\dagger + b_J^\dagger b_I^\dagger) |0\rangle \quad (4.28)$$

$$f_I^\dagger f_J^\dagger |0\rangle = \frac{1}{2} (f_I^\dagger f_J^\dagger - f_J^\dagger f_I^\dagger) |0\rangle \quad (4.29)$$

Note that the form of two input states resemble now closely a symmetric entangled state $|\Psi_{IJ}^+\rangle$ in case of bosons and an antisymmetric entangled state $|\Psi_{IJ}^-\rangle$ in case of fermions. The evolution of the walk in the two cases is indeed:

$$b_I^\dagger b_J^\dagger |0\rangle \rightarrow \frac{1}{2} \sum_{K,L} (U_{IK} U_{JL} + U_{JK} U_{IL}) b_K^\dagger b_L^\dagger |0\rangle \quad (4.30)$$

$$f_I^\dagger f_J^\dagger |0\rangle \rightarrow \frac{1}{2} \sum_{K,L} (U_{IK} U_{JL} - U_{JK} U_{IL}) f_K^\dagger f_L^\dagger |0\rangle \quad (4.31)$$

and the same expressions as in (4.26) for the probability of coincident detection of two particles at two outputs L, K can be retrieved.

Discrete quantum walk by linear optics

Discrete quantum walks of photons can be experimentally realized using an array of beam splitters[145], as shown in Figure 4.11.

Each vertical line of beam splitters represents a step of the quantum walk. Horizontal stripes represent the position $|j\rangle$ of the walker, thus to each beam splitter a position is associated. The quantum coin degree of freedom is given by the fact that the photon can hit the beam splitter on either of the two input modes. Incidence on the upper input mode encodes the $|U\rangle$ quantum coin state, incidence on the lower input mode encodes the $|D\rangle$ quantum coin state.

The beam splitter line implements the following operator:

$$U_{BS} = \frac{1}{\sqrt{2}} \sum_j (|j-1, D\rangle - |j+1, U\rangle) \langle j, D| + (|j-1, D\rangle + |j+1, U\rangle) \langle j, U| \quad (4.32)$$

which can be written as $U_{BS} = EC$, i.e. it performs both the coin flip operation (precisely the Hadamard coin flip) $C = \frac{1}{\sqrt{2}} \begin{pmatrix} 1 & 1 \\ 1 & -1 \end{pmatrix}$ and the evolution E of Eq. (1.7). Note that, if the particle starts at position $|j=0\rangle$, at even (odd) times it will occupy only even (odd) positions.

Provided that all the optical devices used in the walk are polarization insensitive, the polarization degree of freedom may be exploited to entangle the photons injected into the beam splitter array. By playing with the entanglement symmetry it is possible to mimic the quantum dynamics of two identical non-interacting bosons or fermions, as explained before.

tively, the following commutation rules hold:

$$a_J^\dagger a_K^\dagger = \pm a_K^\dagger a_J^\dagger \quad a_J a_K = \pm a_K a_J \quad a_J a_K^\dagger = \delta_{j,k} \pm a_K^\dagger a_J \quad (4.27)$$

where the plus sign applies to bosons while the minus sign applies to fermions, and J, K indicate different modes.

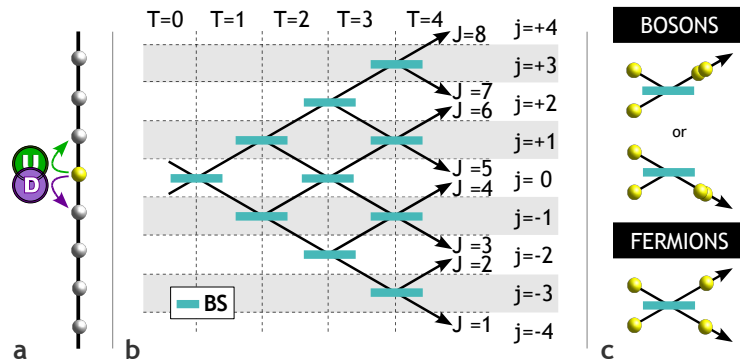


Figure 4.11: (a) One-dimensional quantum walk: depending on the result of the coin toss the walker moves upwards or downwards. (b) Scheme of an array of beam splitters (BSs) for a four-steps discrete-time quantum walk. Vertical dashed lines indicate the steps T of the quantum walk and the horizontal stripes represent the position $|j\rangle$ of the walker. In an array with an even (odd) number of steps the output ports J are grouped into the even (odd) final positions $|j\rangle$ of the walker. (c) Different behaviours of bosons and fermions on a BS.

It must be noticed, at this point, that the experimental realization of such a network of beam splitters is exceedingly difficult with bulk optics, even for a small number of steps. The implementation of T steps requires $\frac{1}{2}T(T+1)$ beam splitters. Aligning this quadratically growing number of elements is a challenging task. Furthermore, for a correct operation of the quantum walk, the phase introduced by the optical paths, passing from each beam splitter to the following, must be controlled and stable.

An integrated waveguide architecture overcomes these problems, allowing to concentrate a large number of optical elements on a small chip, with intrinsic phase stability due to the monolithic structure. In a waveguide implementation, beam splitters are obviously replaced by directional couplers.

In our work we realize an array of directional couplers which implement discrete quantum walk of photons. In particular, the three-dimensional capabilities of femtosecond laser writing are harnessed to achieve an accurate polarization independent behaviour.

4.3.2 Development of the photonic device

4.3.2.1 Polarization independent quantum walk via 3D photonic circuits

As already discussed and widely proved with the experiments reported in the previous Sections, our femtosecond laser written waveguides in EAGLE2000 glass have low birefringence, which does not affect significantly the coherence of the photons. However, the guided modes for the two polarizations have slightly different dimensions, as revealed by an accurate measurement of the mode profiles (Figure 4.12a). This results in a residual polarization dependence in the properties of the fabricated directional couplers, since the coupling coefficient between the two waveguides depends on the overlap integral between the modes.

Consider a directional coupler built with two waveguides brought close along the horizontal (x) direction, which is the most common geometry adopted for these devices (actually, it is also the geometry of the devices reported in Sections 4.1 and 4.2). The vertically (V) polarized modes have a smaller width, along the x axis, with respect to the horizontally (H) polarized modes. This implies a lower evanescent field coupling of the two waveguides, and thus a different reflectivity of the directional coupler, for the V polarization with respect to the H polarization. When several devices need to be cascaded, as in a quantum walk implementation, small differences in the splitting ratios would accumulate and in the end affect the indistinguishability of the two polarizations, which is necessary to implement reliable quantum simulations with polarization entangled photons.

Interestingly, different three-dimensional geometries for the coupler enable to tailor the polarization behaviour of the device and even to reach a perfect polarization insensitivity. For example, if the two waveguides are brought close along the vertical (y) direction, the polarization diversity would be opposite to the previous case. In fact, along the y axis the V polarized mode is slightly greater than the H polarized one. More in general, if the two waveguides lie along an arbitrary direction in the xy plane (see Figure 4.12b) an intermediate situation can be observed. We have thus fabricated several directional couplers with different angles θ for the interaction region, but fixed interaction length and spacing between the waveguides. The waveguide fabrication parameters were the same of Table 4.1. We then estimated the coupling coefficients for H or V polarized inputs. As shown in Figure 4.12c, there exists an angle for which the ratio between the two coefficients is unitary, i.e. the coupler becomes polarization insensitive, thus enabling the realization of a polarization independent quantum walk.

We fabricated a network of directional couplers with the configuration shown in Figure 4.12d, which implements a four steps discrete quantum walk for photons. All the directional couplers are realized with the tilted geometry described above, in which in the interaction region the two waveguides are brought at 11 μm distance, at an angle of 62° , guaranteeing the polarization independence. The length of the interaction region is chosen as $L = 2.1$ mm in order to obtain a balanced splitting ratio. Note that in the interaction region the two waveguides are at different depths in the glass; hence, to connect one coupler to the following the waveguides continuously vary the depth as shown with the color codes in Figure 4.12d. To couple the device with a single-mode fiber array, the two central waveguides of the structure start with an initial separation of 250 μm , while at the output the waveguides are separated by 70 μm . The whole chip is 32 mm long.

The basic cell of the network depicted in Figure 4.12e acts as a Mach-Zehnder interferometer and for the correct operation of the quantum walk all the interferometers present in the network must be phase balanced. Waveguides written at different depths may show in principle slightly different properties (i.e. different effective refractive indices), due to the presence of depth-dependent spherical aberrations when focusing the writing laser beam. However, the highly symmetric three-dimensional geometry implemented in the network (Figure 4.12d-e) is

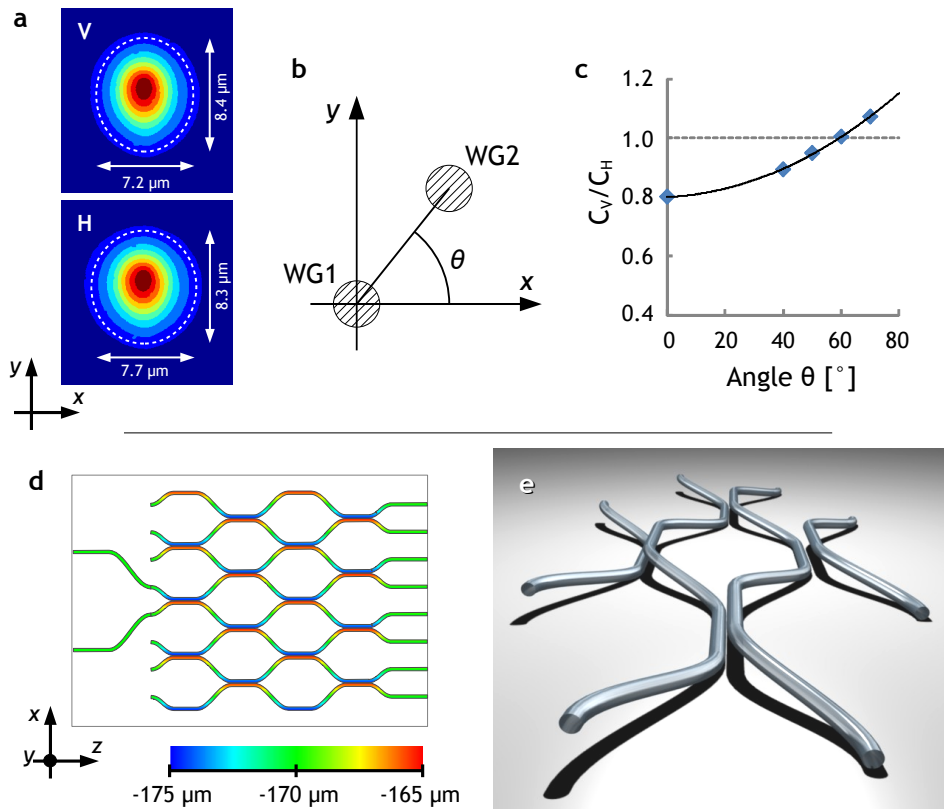


Figure 4.12: (a) Measured intensity profile for the guided modes with polarization V and H, at 806 nm wavelength. The $1/e^2$ dimensions are reported. (b) Schematic cross-section of the interaction region of a directional coupler, where the two waveguides (WG1 and WG2) lies on a plane tilted by an angle θ . (c) Ratio of the estimated coupling coefficients for polarization V (C_V) and polarization H (C_H), for directional couplers fabricated with different angles θ but fixed interaction length 3 mm and distance 11 μm between the waveguides. The fitting line is a guide to the eye. (d) Schematic of the network of directional couplers fabricated for implementing a 4 steps quantum walk. The color coding indicates the writing depth of the waveguides, which is varying from point to point. (e) 3D representation of the basic cell of the network, which acts as a Mach-Zehnder interferometer.

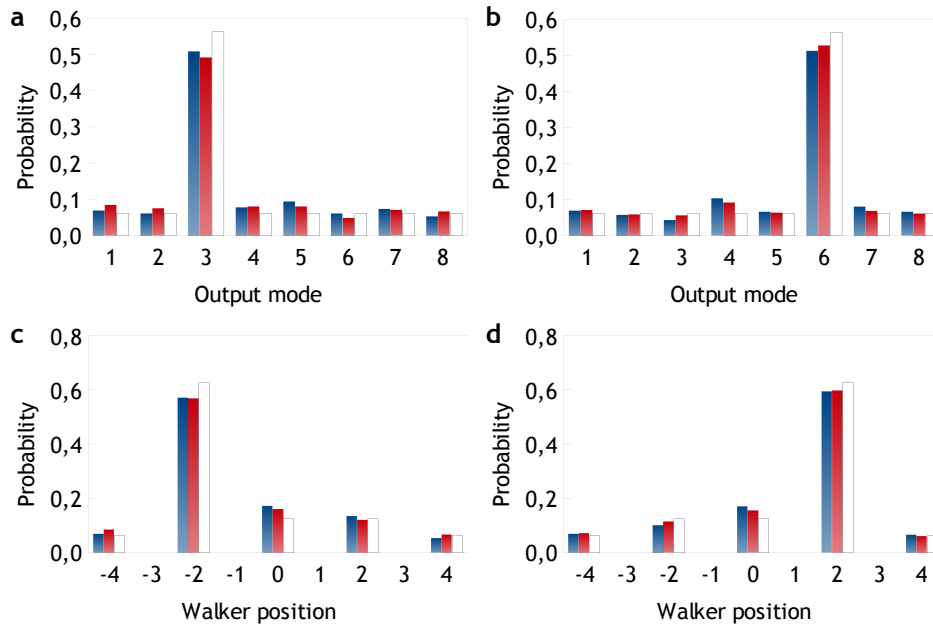


Figure 4.13: Single photon quantum walk, performed by injecting laser light at 806 nm in either of the two inputs. Output modes (a) and position (c) distributions for initial state $|0, U\rangle$, and output modes (b) and position (d) distributions for initial state $|0, D\rangle$ are shown, for both V polarization (red bars) and H polarization (blue bars). White bars represent the theoretical distribution.

designed in such a way that the two branches of each interferometer have the same average depth, so that the optical paths are intrinsically balanced despite the effective refractive index dependence on the writing depth.

4.3.2.2 Characterization with classical light

A first characterization of the quantum walk device was performed in the classical regime, injecting polarized laser light at 806 nm in either of the two input modes and measuring the power distribution at the different outputs. This is equivalent to performing a single particle quantum walk, since interference effects of single photons are the same of coherent light. In particular, the different input modes stand for different initial coin states.

Figure 4.13 shows the experimental output distributions for input polarization H and V, together with the expected one. The distributions in panels a and b refer to the output modes, while the distributions in panels c and d refer to the position j of the walker. Indeed, referring to Figure 4.11, for a walk with T^* step, the relation between the probabilities of photons emerging from one of the $N = 2T^*$ outputs of the BS array (P_j^{BS}) and the final position of the walker

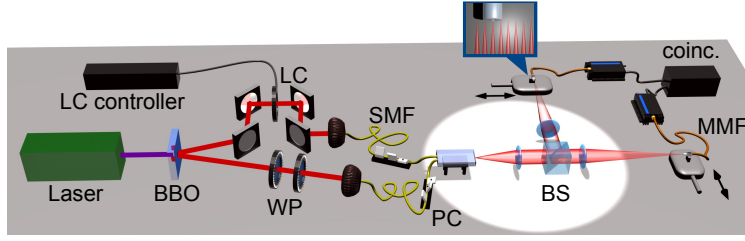


Figure 4.14: Sketch of the experimental setup for the quantum characterization. Polarization entangled photon pairs at wavelength $\lambda = 806$ nm are generated via spontaneous parametric down conversion in a BBO crystal, pumped by a CW laser diode. Separable polarization states can be prepared by inserting polarizing beam splitters (PBSs) and waveplates (WPs). A quarter waveplate (QWP) and a half waveplate (HWP) inserted on the two photon paths allow generation of any kind of entangled states. A delay line (DL) is inserted to control the temporal superposition of the photons, which are then coupled to single mode fibers (SMFs) and injected into the integrated device. Interference filters (IF) determine the photon bandwidth $\Delta\lambda = 6$ nm. A liquid crystal device (LC) is inserted in one of the two paths for a fine control of the phase ϕ . The chip outputs, divided by a beam splitter (BS) and magnified through a telescope of two lenses (focal lengths $f_1 = 50$ mm and $f_2 = 150$ mm), are focused onto multimode fibers (MMFs), coupled to single photon counting modules (SPCMs). The MMFs are mounted on motorized translation stages in order to select an arbitrary combination of two output ports and measure two-photon coincidences. Polarization controllers (PC) are used before the chip to compensate polarization rotations induced by the fibers.

(p_j^{walk}) is:

$$p_{-T^*}^{walk} = P_1^{BS} \quad (4.33)$$

$$p_{-T^*+2k}^{walk} = P_{2k}^{BS} + P_{2k+1}^{BS}, \quad k = 1, \dots, T^* - 1 \quad (4.34)$$

$$p_{T^*}^{walk} = P_{2T^*}^{BS} \quad (4.35)$$

All distributions show excellent fidelity to the theoretical ones (over 99%) for both polarizations.

4.3.3 Quantum characterization

Experimental simulation of bosons, fermions and anyons

The quantum characterization of the device, which actually allowed to simulate the discrete quantum walk of bosons and fermions, was performed using the setup depicted in Figure 4.14. The source of entangled photons is the same used in the experiments reported in Sections 4.1 and 4.2. The output of the integrated device is collected by a suitable telescope, divided into two branches by a bulk beam splitter and then coupled to two multimode fibers. Independent and computer controlled translation of the two multimode fibers on the arms C and D enable to select the output ports to detect, respectively I and J , and measure the single photon signals $\mathcal{S}_C(I)$ and $\mathcal{S}_D(J)$ and two-photon coincidences $\mathcal{C}_{CD}(I, J)$.

The states $|\Psi^+\rangle$ and $|\Psi^-\rangle$ were injected into the chip and the output distributions were reconstructed from the coincidence counts $\mathcal{C}_{CD}(I, J)$, acquired for each combination of the indices I and J . In Figure 4.15a-b the experimental distributions are plotted, with comparison to the theoretical distributions for a quantum walk of bosons and fermions respectively.

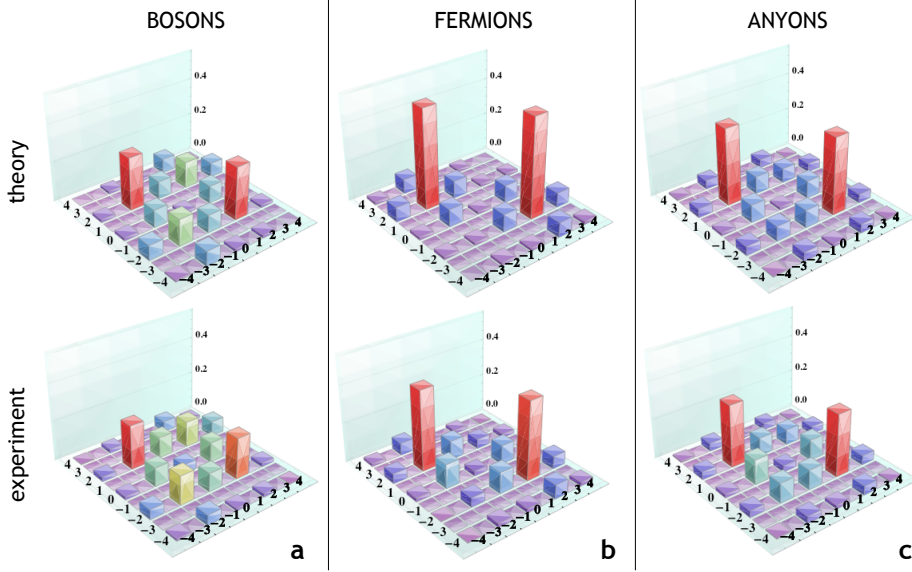


Figure 4.15: Two-particle quantum walks: ideal (*top*) and measured (*bottom*) distributions of (a) bosonic, (b) fermionic and (c) anyonic (with $\phi = \pi/2$) quantum walks.

The presence of relevant diagonal elements in the obtained distribution for bosons highlights the bunching behaviour of a symmetric two-particle system; on the other hand the fermionic distribution presents significant off-diagonal elements, confirming that an antisymmetric two-particle system undergoes the anti-bunching phenomenon. The presence of small but non-vanishing diagonal elements in the fermionic distributions (both theoretical and experimental) is not in contrast with the impossibility for two identical fermions to be in the same state, since the distributions of Figure 4.15 regard the walk positions and not the modes. Indeed, theory predicts rigorously vanishing probabilities to find two photons in the same optical mode when the antisymmetric (fermionic) entangled state is injected.

Generic entangled states $|\Psi^\phi\rangle = \frac{1}{\sqrt{2}}(|H\rangle_A|V\rangle_B + e^{i\phi}|V\rangle_A|H\rangle_B)$, can also be prepared, where ϕ is a generic phase difference between H and V on the mode B . These simulate particles characterized by non semi-integer spin, the so-called anyons⁴, characterized by both bunching and anti-bunching behaviours (i.e. diagonal and off-diagonal elements in the final distribution).

As a further measurement, some anyonic states $|\Psi^\phi\rangle$ were injected in the quantum walk device, in particular with $\phi = \frac{\pi}{4}, \frac{\pi}{2}, \frac{3}{4}\pi$, and the output distributions were measured. In Figure 4.15c the distribution for $\phi = \frac{\pi}{2}$ is reported as an example of an anyonic behaviour.

The experimental data can be compared with the theoretical distributions

⁴This kind of particles is possible only in a two-dimensional Hilbert space, thus they cannot be observed in the ordinary three-dimensional space. The entangled state $|\Psi^\phi\rangle$ simulates two anyons characterized by creation operators satisfying $c_i c_j = e^{i\phi} c_j c_i$ and $c_i c_j^\dagger = e^{i\phi} c_j^\dagger c_i + \delta_{ij}$.

by the similarity $S = (\sum_{i,j} \sqrt{D_{ij}D'_{i,j}})^2 / \sum_{i,j} D_{ij} \sum_{i,j} D'_{ij}$, which is a generalization of the classical fidelity between two distributions D and D' . Obtained similarities are $S_{bos} = 0.982 \pm 0.002$ and $S_{fer} = 0.973 \pm 0.002$ for the bosonic and fermionic quantum walk, and $S_{any}^{\pi/4} = 0.987 \pm 0.002$, $S_{any}^{\pi/2} = 0.988 \pm 0.001$ and $S_{any}^{3\pi/4} = 0.980 \pm 0.002$ for the anyonic quantum walks with $\phi = \frac{\pi}{4}, \frac{\pi}{2}, \frac{3}{4}\pi$, respectively.

4.4 Photonic simulation of the Jaynes-Cummings dynamics

4.4.1 The idea behind the experiment

The Jaynes-Cummings model

The Jaynes-Cummings model is a landmark in modern quantum physics, since it describes the interaction between a two-level quantum system (qubit) and a bosonic mode (Figure 4.16a), for example an atom in the quantized field of a resonant cavity. The hamiltonian of such system is typically written as:

$$\hat{H}_{\text{JC}} = \frac{1}{2}\hbar\omega_0\hat{\sigma}_z + \hbar\omega\hat{a}^\dagger\hat{a} + \hbar g (\hat{\sigma}^\dagger + \hat{\sigma}) (\hat{a}^\dagger + \hat{a}) \quad (4.36)$$

where a and a^\dagger are the annihilation and creation operators of the bosonic mode, with characteristic frequency ω ; $\hat{\sigma}_z = |e\rangle\langle e| - |g\rangle\langle g|$, $\hat{\sigma}^\dagger = |g\rangle\langle e|$, $\hat{\sigma} = |e\rangle\langle g|$ are Pauli operators for a qubit with ground state $|g\rangle$ and excited state $|e\rangle$; ω_0 is the transition frequency of the qubit and g is the interaction strength. \hat{H}_{JC} is composed of three terms, which refer, in the order, to: the qubit, the bosonic mode and the interaction between the two.

To highlight the different dynamics that can arise, it is useful to discuss in some detail the interaction term of the hamiltonian, which describes essentially an electric-dipole-like interaction:

$$\hat{H}_{\text{QF}} = \hbar g (\hat{\sigma}^\dagger + \hat{\sigma}) (\hat{a}^\dagger + \hat{a}) = \hbar g (\hat{\sigma}^\dagger\hat{a} + \hat{\sigma}\hat{a}^\dagger + \hat{\sigma}^\dagger\hat{a}^\dagger + \hat{\sigma}\hat{a}) \quad (4.37)$$

On one hand, $\hat{\sigma}^\dagger a = a|e\rangle\langle g|$ and $\hat{\sigma} a^\dagger = a^\dagger|g\rangle\langle e|$ mean, respectively, photon absorption with the qubit passing from $|g\rangle$ to $|e\rangle$, and photon emission with the qubit decaying from $|e\rangle$ to $|g\rangle$. On the other hand, $\hat{\sigma}^\dagger a^\dagger = a^\dagger|e\rangle\langle g|$ and $\hat{\sigma} a = a|g\rangle\langle e|$ describe counterintuitive situations in which, respectively, a photon is emitted and at the same time the qubit is excited or a photon is absorbed and at the same time the qubit decays.

The Jaynes-Cummings hamiltonian is usually studied in the near-resonance and weak-coupling limits ($|\omega - \omega_0| \ll \omega_0$, $\omega \gg g$). Under these hypotheses it can be shown that the terms $\hat{\sigma}^\dagger a^\dagger$ and $\hat{\sigma} a$ of the interaction hamiltonian \hat{H}_{QF} originate rapidly oscillating terms in the temporal evolution of the wavefunction, which can be neglected. This is the so called *rotating wave approximation*, and in this case \hat{H}_{JC} is rewritten as:

$$\hat{H}_{\text{JC,RWA}} = \frac{1}{2}\hbar\omega_0\hat{\sigma}_z + \hbar\omega\hat{a}^\dagger\hat{a} + \hbar g (\hat{a}\hat{\sigma}^\dagger + \hat{a}^\dagger\hat{\sigma}) \quad (4.38)$$

In such weak coupling limit, which is the one encountered in many quantum electrodynamics experiments, the Jaynes-Cummings model is exactly solvable and predicts, for example, Rabi oscillations and their collapses and revivals. At the other extreme we have the *deep strong coupling* regime, in which g is of the order or greater than ω . This regime has been recently object of a theoretical study[146] but it is indeed very difficult to achieve in experiments of cavity

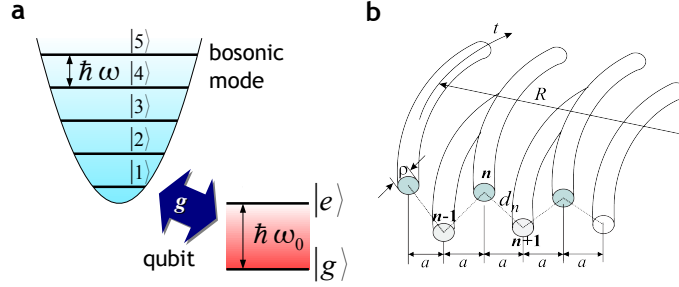


Figure 4.16: (a) Schematic of a two level quantum system (qubit), interacting with a single bosonic mode. (b) Proposed geometry for a photonic structure that realizes the Jaynes-Cummings model. The structure consists of a curved binary waveguide array.

quantum electrodynamics: recent experiments[147] with superconducting artificial atoms have reached only a $g/\omega \simeq 0.1$.

To describe the Jaynes-Cummings interaction in the deep strong coupling regime, the full hamiltonian of Eq. (4.36) must be considered[146, 148]. The state vector of the system can be expanded as:

$$|\psi(t)\rangle = \sum_{n=0}^{\infty} a_n(t)|e\rangle|n\rangle + b_n(t)|g\rangle|n\rangle \quad (4.39)$$

which can be substituted into the Schroedinger's equation $i\hbar\partial_t|\psi(t)\rangle = \hat{H}|\psi(t)\rangle$ to obtain the temporal evolution of a_n and b_n . Interestingly, adopting the following variable change:

$$c_n = \begin{cases} a_n & n \text{ even} \\ b_n & n \text{ odd} \end{cases} \quad f_n = \begin{cases} a_n & n \text{ odd} \\ b_n & n \text{ even} \end{cases}$$

one can write two independent equation sets for the c_n and the f_n :

$$i\frac{dc_n}{dt} = \kappa_n c_{n+1} + \kappa_{n-1} c_{n-1} + (-1)^n \frac{\omega_0}{2} c_n + n\omega c_n \quad (4.40)$$

$$i\frac{df_n}{dt} = \kappa_n f_{n+1} + \kappa_{n-1} f_{n-1} - (-1)^n \frac{\omega_0}{2} f_n + n\omega f_n \quad (4.41)$$

where $n = 0, 1, 2, \dots$ and

$$\kappa_n = g\sqrt{n+1} \quad (4.42)$$

The deep strong coupling regime presents some interesting features[146, 148], which go beyond the well-known rotating wave approximation behaviour. For example, if $\omega_0/\omega \rightarrow 0$ (high frequency of the field, out of resonance) the dynamics is strictly periodic, with period $T = 2\pi/\omega$. Bouncing of photon number wavepackets are observed, with peaks in the photon number which are increasing with increasing g . Even in the case of initial state $|g\rangle|0\rangle$ (qubit initially in the ground state and no photons in the cavity), the expected photon number, oscillating with revivals and collapses, reach considerable values. This periodicity vanishes for $\omega_0/\omega \neq 0$.

Proposal of photonic simulator

Equations (4.40) and (4.41) have the form of coupled mode equations, as in (1.11). A photonic structure in which spatial light propagation displays analogies with the temporal Jaynes-Cummings dynamics has in fact been proposed[148]. In particular, the two uncoupled equations (4.40) and (4.41) can be simulated by two uncoupled waveguide lattices. Each of them consists of a semi-infinite binary waveguide array, for which the tight-binding approximation holds and the coupling coefficients between the waveguides follow the square-root law of Eq. (4.42). A judicious choice of the distances d_n between the waveguides gives the proper coupling constants κ_n . If the coupling coefficients depend on the distance with an exponential law $\kappa(d) = Ce^{-d/d^*}$, the distances d_n will follow a logarithmic trend:

$$d_n = d_0 - \frac{d^*}{2} \ln(n+1) \quad (4.43)$$

The bending of the structure provides a transverse index gradient ω , according to the formula[149]:

$$\omega = 2\pi n_{\text{eff},n} a / R\lambda \quad (4.44)$$

where $n_{\text{eff},n}$ is the effective refractive index of the waveguide n -th, λ is the operation wavelength, R is the bending radius and a the horizontal spacing between waveguides. Note that for producing a uniform transverse index gradient the horizontal spacing a must be constant; on the other hand, different interwaveguide distances are required for satisfying Eq. (4.42), hence the need for the three-dimensional geometry shown in Figure 4.16b. A further propagation constant mismatch ω_0 can be realized varying the effective index of the waveguides. In case of femtosecond laser fabricated waveguides, this can be accomplished by simply varying the writing speed.

4.4.2 Fabrication of the photonic simulator

4.4.2.1 Waveguide parameters optimization

As discussed in Section 1.1.3, a very powerful way to visualize the light propagation pattern exploits the fluorescent emission of color centers, created in fused silica by the femtosecond laser pulses irradiation. Since fluorescence need to be excited around 633 nm, as a first step of our work we optimized the fabrication parameters in fused silica substrate in order to achieve low losses and single mode guiding at this wavelength.

We chose the FemtoREGEN system for the wider parameters range that can be explored. We tested different pulse energies and writing wavelengths (the fundamental and the second harmonic) at very low repetition rate (2 kHz) in order to avoid any thermal effect, which in fused silica may not be desirable[31]. Focusing was always performed by a 0.45 NA objective, without any beam shaping stage. The fundamental wavelength did not provide any waveguiding structure, while optimum guiding properties were found adopting the second harmonic, 300 nJ pulses and 1 mm/s translation speed. Afterwards, we aimed at increasing the processing speed by increasing the repetition rate, while keeping constant the

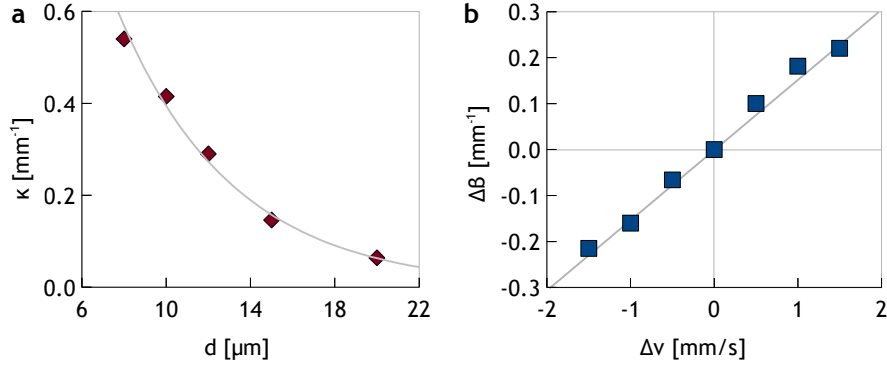


Figure 4.17: (a) Measured coupling coefficients as a function of the distance between waveguides. Exponential fit is shown. (b) Measured variation in the propagation constant ($\Delta\beta$) as a function of the variation in the writing speed of the waveguides. Linear fit is shown.

pulse energy and the fluence (i.e. increasing the translation velocity proportionally to the repetition rate). We observed waveguides with the same properties up to 100 kHz repetition rate, while at 250 kHz insertion losses increased and the waveguide cross-section, observed at an optical microscope, appeared slightly altered by thermal effects. Anyway, at 100 kHz repetition rate the required translation speed already reaches the significantly high value of 50 mm/s, which can cause problem in the precise control of the sample motion. For this reason, we chose the fabrication parameters reported in Table 4.3, i.e. 20 kHz repetition rate and 10 mm/s translation speed.

Propagation losses of 0.5 dB/cm were estimated by measuring the decay of the fluorescence signal of a straight waveguide along the propagation. Hence, these losses include both the scattering losses and the absorption due to the color centers, at the origin of the fluorescence. The $1/e^2$ diameter of the mode intensity profile at 633 nm wavelength was measured to be $\sim 13 \mu\text{m}$.

Fabrication parameters	
Substrate	fused silica
Laser system	FemtoREGEN
Wavelength	520 nm (SHG)
Repetition rate	20 kHz
Pulse energy	300 nJ
Translation speed	10 mm/s
Objective	0.45 NA

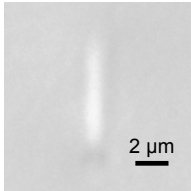


Table 4.3: Waveguide writing parameters used for building the photonic simulator of the Jaynes-Cummings dynamics. Microscope image of the waveguide cross-section is also shown.

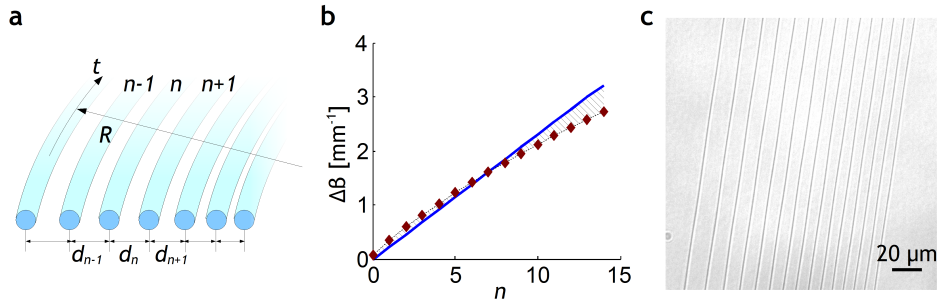


Figure 4.18: (a) Planar array of curved waveguides which realizes the Jaynes-Cummings interaction. (b) Variation $\Delta\beta$ in the propagation constants β of the curved waveguides in the array: actual trend without compensation due to a non-uniform waveguide spacing (*diamonds*) and target linear trend achieved after writing parameters compensation (*solid line*). (c) Top-view microscope image of the curved waveguide array.

4.4.2.2 Coupled waveguides properties

The construction of a photonic structure that reproduces the behaviour of the coupled mode equations (4.40) and (4.41) requires on one hand the knowledge of the coupling coefficient dependence on the waveguide distance, and on the other hand the knowledge of the propagation constant dependence on the writing speed.

Uniform arrays of straight waveguides at different reciprocal distances were fabricated. Light at 633 nm was coupled in the central waveguide and the output distribution was acquired. Fitting back the output distribution with the theory allowed to retrieve the coupling coefficients. The coupling coefficients κ as a function of the waveguide distance d were then fitted with an exponential law (Figure 4.17a). The result was $\kappa(d) = 2.4 \text{ mm}^{-1} e^{-d/5.47 \text{ } \mu\text{m}}$.

Couples of parallel waveguides were then fabricated at the distance of 15 μm . One waveguide of the two was written at 10 mm/s speed. The other waveguide was written at a different speed for each coupler, ranging in the interval $8.5 \div 11.5 \text{ mm/s}$. From the measurement of the output power distribution it is possible to retrieve the propagation constant detuning, by using the solution of the coupled mode equations in case of two non-identical waveguides[42]. A linear dependence of the propagation constant detuning on the velocity difference was found (Figure 4.17b), with a derivative equal to $\Delta\beta/\Delta v \simeq 0.15 \text{ s/mm}^2$.

4.4.2.3 Design issues

The design reported in Figure 4.16b, proposed in [148] for the photonic simulator, suffers from some drawbacks.

First, from the picture one can observe that waveguides that are second neighbours may be at a reciprocal distance which is of the order of that between first neighbours. The actual ratio between the two distances depends on several factors, such as the desired ω and the dependence of the coupling κ on the distance d . We evaluated possible structures with this design using our waveguide parameters and we found that, for reasonable ω , the problem of second-neighbours interactions would have been significant.

A possible solution to the previous problem could be to design a similar structure, with the same interwaveguide distances d_n , with the horizontal spacing a analogous to Figure 4.16b, but with the vertical spacing always in the same direction i.e. the $(n + 1)$ -th waveguide is always shallower than the n -th one. A wider extension in the vertical dimension poses clearly no problems to the three-dimensional abilities of the femtosecond laser writing technique. Nevertheless, it becomes practically impossible to image at the same time waveguides at such different depth, keeping enough resolution.

In the light of these considerations, we chose to adopt a different design for the photonic structures, which is fully planar, shown in Figure 4.18a. It consists of a planar array of curved waveguides with engineered distances d_n in order to implement the desired coupling coefficients κ_n . The circular curvature of the waveguides introduces a transverse refractive index gradient leading to $\omega = 2\pi n_{\text{eff},n} d_n / (R\lambda)$. Since the distances d_n between different waveguides are not uniform in the array (Figure 4.18c), the value of ω also varies with the waveguide number n (see diamonds in Figure 4.18b). To achieve a uniform ω in the array a compensation is required in the effective index $n_{\text{eff},n}$ of the waveguides, yielding a uniform $n_{\text{eff},n} d_n$ product. This compensation can be achieved by suitably choosing the writing speed for each waveguide (Figure 4.17b). In addition to this uniform transverse index gradient, the ω_0 detuning is implemented by a further modulation of the effective refractive index (i.e. writing speed) in alternating waveguides.

4.4.3 Experimental simulation of the deep strong coupling regime

4.4.3.1 The case $\omega_0 = 0$

As a first experiment, we addressed the simulation of the deep strong coupling regime in the case $\omega \gg \omega_0$, i.e. a characteristic frequency of the bosonic mode much larger and strongly detuned with respect to the characteristic frequency of the qubit. This case is equivalent to $\omega_0 \rightarrow 0$, which means that the qubit levels are degenerate.

We manufactured an array of 15 curved waveguides, following the design of Figure 4.18a. Distances between waveguides were engineered following Eq. (4.43) to give $g = 0.15 \text{ mm}^{-1}$. A bending radius of $R = 650 \text{ mm}$ was adopted; together with the effective index compensation (writing speeds varied in the range $10 \div 14 \text{ mm/s}$), this provided a uniform gradient $\omega = 0.23 \text{ mm}^{-1}$. Note that the deep strong coupling regime is reached, given the ratio $g/\omega = 0.65$.

In the experiment, the $n = 0$ waveguide is excited by He:Ne laser light at the input plane (left side in Figure 4.19a), corresponding to the system in the initial state $|\psi(0)\rangle = |e\rangle|0\rangle$. Fluorescence imaging of the light propagation pattern is performed. A periodic bouncing of the photon distribution can be clearly observed, in very good agreement with the expected one (Figure 4.19b). The qubit population of the $|e\rangle$ level is given by $P_e(t) = \sum_{n=0}^{\infty} |c_{2n}|^2$, while the revival probability is defined as $P_r(t) = |\langle \psi(t) | \psi(0) \rangle|^2 = |c_0|^2$. The evolution of these two quantities can be readily retrieved from the light intensity map of

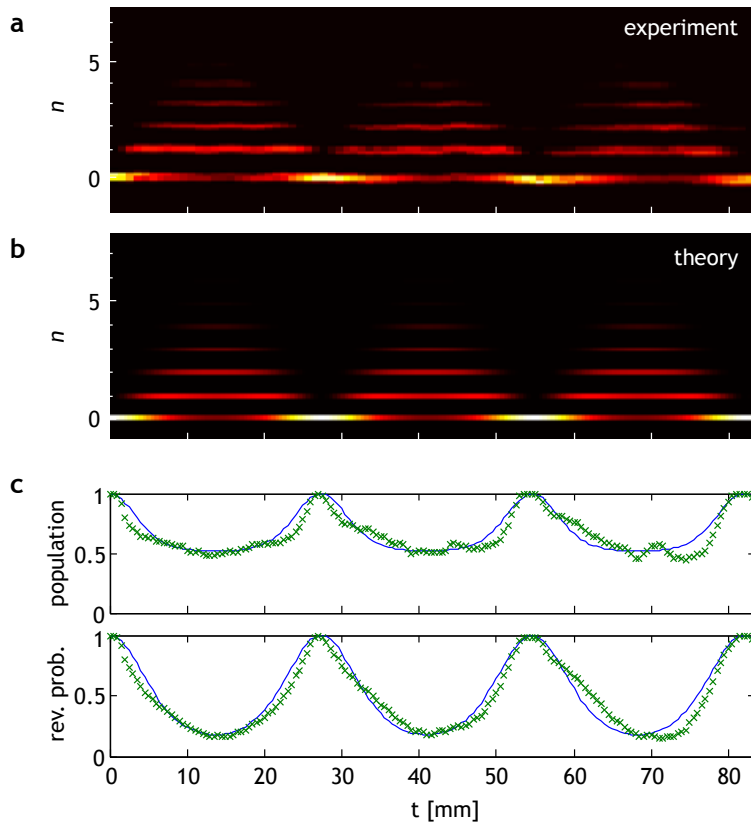


Figure 4.19: (a) Measured and (b) predicted light intensity distributions in the waveguide array for $\omega_0 = 0$, showing the periodic bouncing of photon number statistics $P(n, t)$. (c) Evolution of population P_e of level $|e\rangle$ (*upper panel*) and of the revival probability P_r (*lower panel*) (crosses: experimental points; solid line: theoretical model).

Figure 4.19a, and is depicted in Figure 4.19c.

It can be observed that all the quantities describing the system follow a strictly periodic behaviour, with a period $T = 2\pi/\omega \simeq 27$ mm. This is given by the fact that the hamiltonian of the system (Eq. (4.36)) can be diagonalized[146] and has equally spaced energy levels, with a separation $\hbar\omega$.

4.4.3.2 The case $\omega_0 \neq 0$

We then addressed the case $\omega_0 \neq 0$, maintaining an off-resonance condition ($|\omega| \gg |\omega_0|$). We fabricated several structures of 15 waveguides, with exactly the same parameters of the one realized for the case $\omega = 0$, except for the further modulation in the writing speed to give the detunings $\omega_0 = -0.08, -0.04, +0.04, +0.08$ mm $^{-1}$.

When $\omega_0 \neq 0$, the energies of \hat{H} are no more equally spaced, and the bouncing dynamics ceases to be periodic[146]. However, in strongly off-resonance conditions, an imperfect bouncing dynamics can be still observed in the early stage

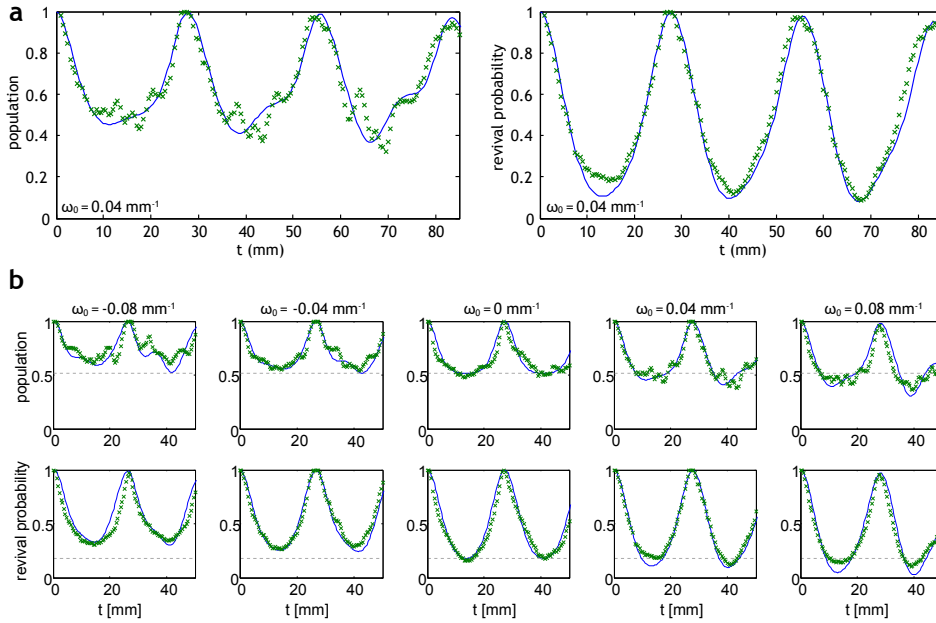


Figure 4.20: (a) Same as Figure 4.19c, but for a waveguide array with $\omega_0 = 0.04 \text{ mm}^{-1}$. (b) Early evolution of revival probability P_r and populations P_e (for $\omega_0 > 0$) and $P_g = 1 - P_e$ (for $\omega_0 < 0$) as ω_0 is tuned from negative (initial state $|\psi(0)\rangle = |g\rangle|0\rangle$) to positive (initial state $|\psi(0)\rangle = |e\rangle|0\rangle$) values. Solid curves: theory; crosses: experimental points. The dashed horizontal lines in the plots show, as reference levels, the minimum values of revival probability and populations attained in the first bounce interval for the $\omega_0 = 0$ case.

of the evolution. As an example, Figure 4.20a shows the evolution of P_e and P_r observed in an array with $\omega_0 = 0.04 \text{ mm}^{-1} \ll \omega$, together with the corresponding theoretical curves, for the system in the initial state $|\psi(0)\rangle = |e\rangle|0\rangle$. Smearing out of the periodic dynamics at successive bounces can be appreciated in this case.

The evolution of both revival probability and populations, besides losing the exact periodic behaviour, is also sensitive to the sign of ω_0 . In fact, according to Eqs. (4.40) and (4.41) the sign of ω_0 defines two distinct initial states of the qubit: the qubit is in the excited state for $\omega_0 > 0$, whereas it is in the ground state for $\omega_0 < 0$. Such different initial conditions lead to different field-atom dynamics for the same initial photon number distribution. This is clearly shown in Figure 4.20b, which represents the early evolution of both revival probability P_r and populations P_e (for $\omega_0 > 0$) and $P_g = 1 - P_e$ (for $\omega_0 < 0$) as ω_0 is tuned from negative to positive values, always for an initial states of absence of photons. Note that, as ω_0 is increased from negative to positive values, the minimum value of both the population and revival probability, reached within the first bounce, decreases. In fact, keeping fixed the atom-field coupling g , the system will be in a lower energy state for the atom initially in the ground state with respect to the case in which the atom is initially excited: this makes it less or more probable, respectively, to create new field quanta.

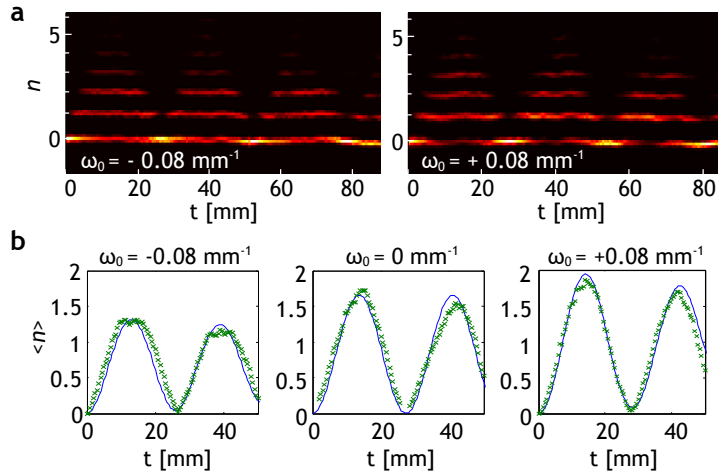


Figure 4.21: (a) Measured light intensity distribution in a waveguide array for $\omega_0 = -0.08 \text{ mm}^{-1}$ (left panel) and $\omega_0 = +0.08 \text{ mm}^{-1}$ (right panel). (b) Evolution of the mean photon number $\langle n \rangle$ for $\omega_0 = 0, \pm 0.08 \text{ mm}^{-1}$.

Indeed, the possibility of creating excitation in both the atom and the field starting from an initial state $|\psi(0)\rangle = |g\rangle|0\rangle$, as demonstrated in the left panels of Figure 4.20b corresponding to $\omega_0 < 0$, is a rather amazing feature of the deep strong coupling regime. This is an effect of the two counter-rotating terms, normally neglected in the rotating wave approximation, and at a first sight it seem to violate energy conservation. Actually, in such regime, also the “coupling” energy is significant, being of the same order of the energy of the isolated qubit and field. Hence, conservation of energy is still guaranteed considering this further contribution.

The different dynamics of the cases $\omega_0 < 0$ and $\omega_0 > 0$ can be further highlighted by the graphs reported in Figure 4.21, where the detailed evolution of the photon number distribution $P(n, t)$ is shown, together with the average number of created photons $\langle n \rangle$, for cases $\omega_0 = -0.08 \text{ mm}^{-1}$ and $\omega_0 = 0.08 \text{ mm}^{-1}$. In both cases $\langle n \rangle$ follows the bouncing dynamics of $P(n, t)$. Anyway, consistently with the above discussion, the maximum value of $\langle n \rangle$ within the bouncing cycle is noticeably larger in the $\omega_0 > 0$ case.

Chapter 5

Conclusions

Several experiments have been reported, highlighting different aspects and potentials of the femtosecond laser micromachining technique.

A three-dimensional Mach-Zehnder interferometer has been demonstrated, directly integrated in a microfluidic chip. This shows not only the possibility of femtosecond laser writing to add new photonic capabilities to existing fluidic lab-on-chips, but also its ability to integrate specific sensing functions, hardly achievable with other technologies. In fact, the particular three-dimensional geometry of the device, impossible to realize by conventional lithographic techniques, enables high spatial resolution on the microchannel, conjugated with elevate refractive index sensitivity. These characteristics are of crucial importance in applications such as detection in microchip capillary electrophoresis and multipoint real-time monitoring of chemical reactions inside a lab-on-chip.

The realization, by femtosecond laser pulses, of a similar integrated structure, combining a Mach-Zehnder interferometer with an etched microchannel, has allowed to demonstrate for the first time quantum interferometry measurements on biological samples. The main issues regarding this kind of measurements have been explored and a clear path towards real world application of quantum enhanced interferometry has been indicated. In fact, optofluidics allows to combine the stability of integrated optical circuits with the capabilities of microfluidics in handling with high precision small volumes of analytes.

Three experiments have been reported, in which the use of femtosecond laser written waveguides have enabled to integrate quantum circuits for polarization encoded qubits. The manipulation of polarization entangled photon states is essential to implement many quantum information protocols for computation and communication. The possibility to harness higher order entanglement, combining linear momentum and polarization, is envisaged. In addition, on-chip realization of the quantum walk model paves the way to the simulation of complexity physics and biophysics phenomena, such as Anderson localization and charge transport in light-harvesting complexes. These results are significant also from the point of view of the fabrication technique, since it is the first time that components such as partially polarizing directional couplers are realized by femtosecond pulses. More in general, a quite innovative approach to polarization handling circuits

is proposed, based on a kind of “universal” waveguide, whose birefringence is low but non-zero, and well determined. Just by varying the three-dimensional geometry of the devices, it is demonstrated how the polarization behaviour can be finely tailored, from a perfect polarization insensitivity up to a fully polarization dependent operation.

The possibility of using femtosecond laser written waveguides to simulate quantum systems has been explored also exploiting quantum-optical analogies, which allow to reproduce complex quantum dynamics in photonic circuits just by injecting coherent light. In particular the regime of “deep strong coupling” of the Jaynes-Cummings hamiltonian, still inaccessible in quantum cavity electrodynamics, has been accurately simulated by means of an engineered waveguide array.

In conclusion, the work of this thesis clearly shows how femtosecond laser micromachining enables to develop complex photonic devices, which open new perspectives in fields such as integrated sensing, quantum computation and simulation.

Appendix A

Classical and quantum interference

A.1 Classical interference

In the framework of classical physics, electromagnetism is completely described by the four Maxwell equations, which regards the electric field \vec{E} and magnetic field \vec{H} . The linearity of these equations guarantees for a *superposition principle* of these fields. Let us consider two electromagnetic sources which generate in a certain point of the space and at a certain time, respectively, a field \vec{E}_1 and \vec{E}_2 , if taken singularly. The effects of the coexistence of these two sources, in that point of the space and at that time, will be the same as of having a field \vec{E}_{res} :

$$\vec{E}_{\text{res}} = \vec{E}_1 + \vec{E}_2 \quad (\text{A.1})$$

In case of waves, the effects and consequences of this principle, are commonly named *interference*. In fact, in particular for the case of waves at optical frequencies, the measurable physical quantity is not the electric (nor magnetic) field itself, but the intensity $I \propto |\vec{E}|^2$. Thus, considering two optical beams of intensities I_1 and I_2 impinging at the same point, Eq. (A.1) implies the following law for the resulting intensity I_{res} :

$$I = I_1 + I_2 + 2\sqrt{I_1 I_2} \cos \phi \quad (\text{A.2})$$

where ϕ is the reciprocal phase difference of the two beams.

Varying the phase ϕ , the resulting intensity changes and interference *fringes* appear. In general, the visibility V of the interference fringes is defined as:

$$V = \frac{I_{\text{res}}^{\text{max}} - I_{\text{res}}^{\text{min}}}{I_{\text{res}}^{\text{max}} + I_{\text{res}}^{\text{min}}} \quad (\text{A.3})$$

with $I_{\text{res}}^{\text{max}}$ and $I_{\text{res}}^{\text{min}}$ maximum and minimum values of the resulting intensity, respectively. Substituting the maxima and minima of Eq. (A.2) in Eq. (A.3) one

obtains:

$$V = \frac{2\sqrt{I_1 I_2}}{I_1 + I_2} \quad (\text{A.4})$$

Maximum (unitary) visibility is reached for $I_1=I_2$.

It is worth noting that to observe interference phenomena the phase difference between the two beams must be well defined and constant in time.

A.2 Electromagnetic field quantization and quantum interference

In quantum mechanics the wave-particle duality emerges: photons are the particles associated to electromagnetic radiation. The quantized electromagnetic field is described by the following hamiltonian (quantized modes of a cavity, considering only one polarization):

$$H_R = \frac{1}{2} \sum \hbar\omega_i (a_i^\dagger a_i + a_i a_i^\dagger) \quad (\text{A.5})$$

where the creation and annihilation operators a^\dagger and a have been introduced¹ and ω_i are the angular frequencies of the different modes. The symmetric expression of the hamiltonian takes into account the bosonic nature of the photons.

Considering an optical beam, the physical quantity of interest (related to the classical intensity) is now the average number of photons, given by the photon number operator $N = a^\dagger a$. The eigenstates of this operator, i.e. states with a fixed number of photons, are called Fock states, defined by:

$$a^\dagger a |n\rangle = n |n\rangle \quad (\text{A.6})$$

The creation and annihilation operators act on the Fock states adding or subtracting a photon, according to:

$$a |n\rangle = \sqrt{n} |n-1\rangle \quad (\text{A.7})$$

$$a^\dagger |n\rangle = \sqrt{n+1} |n+1\rangle \quad (\text{A.8})$$

$$a |0\rangle = 0 \quad (\text{A.9})$$

Classical interference can of course find explanation also in the quantum picture. Anyway, new interference phenomena arise, which can be explained only within the quantum framework. The emblematic example of quantum interference is the interference of two indistinguishable photon at a beam splitter.

A beam splitter is a device that makes two optical modes interact. Be a and b the annihilation operators of the two modes at the input of the beam splitter.

¹ Given the commutation relations $[a_i, a_j] = [a_i^\dagger, a_j^\dagger] = 0$, $[a_i, a_j^\dagger] = \delta_{i,j}$, the hamiltonian (A.5) can be also rewritten as:

$$H_R = \sum \hbar\omega_i \left(a_i^\dagger a_i + \frac{1}{2} \right)$$

According to the Heisenberg picture, these operators evolve through the beam splitter due to the interaction between the modes, to become a' and b' at the output. The following matrix equation holds for the annihilation operators:

$$\begin{bmatrix} a' \\ b' \end{bmatrix} = \begin{bmatrix} \sqrt{T} & i\sqrt{R} \\ i\sqrt{R} & \sqrt{T} \end{bmatrix} \begin{bmatrix} a \\ b \end{bmatrix} \quad (\text{A.10})$$

If we now consider an input state of two indistinguishable photon, one per mode:

$$|1_a 1_b\rangle = a^\dagger b^\dagger |0\rangle \quad (\text{A.11})$$

the output state will be, transforming the operators²:

$$a^\dagger b^\dagger |0\rangle \rightarrow a'^\dagger b'^\dagger |0\rangle$$

$$\begin{aligned} a'^\dagger b'^\dagger |0\rangle &= \left(\sqrt{T}a^\dagger - i\sqrt{R}b^\dagger \right) \left(-i\sqrt{R}a^\dagger + \sqrt{T}b^\dagger \right) |0\rangle = \\ &= -i\sqrt{TR} (a^{\dagger 2} + b^{\dagger 2}) |0\rangle + (T - R) a^\dagger b^\dagger |0\rangle = \\ &= -2i\sqrt{TR} \frac{(|2_a 0_b\rangle + |0_a 2_b\rangle)}{\sqrt{2}} + (T - R) |1_a 1_b\rangle \end{aligned} \quad (\text{A.12})$$

In the general case the output state will be a superposition of the state $\frac{(|2_a 0_b\rangle + |0_a 2_b\rangle)}{\sqrt{2}}$ (two photon in either mode) and $|1_a 1_b\rangle$ (one photon per mode). Interestingly, the latter term completely disappear in the case $T = R = 1/2$ of a balanced beam splitter. This is the Hong-Ou-Mandel effect[100] of quantum interference: if two indistinguishable photons impinge on two modes of a balanced beam splitter they will be never found, at the output, on two separate modes.

Note that in this kind of interference the reciprocal phase of the two photons is not relevant. Indeed, in Fock states, such as the single photon states considered, the phase is not defined at all, because of the Heisenberg uncertainty principle. This phenomenon is thus observed on a beam splitter, without the need for a more complex interferometric configuration.

²The transformation of the creation operators can be easily retrieved from Eq. (A.10), since creation operators are the hermitian conjugate of the annihilation operators.

Journal publications

- A. Crespi, Y. Gu, B. Ngamsom, H.J.W.M. Hoekstra, C. Dongre, M. Pollnau, R. Ramponi, H.H. van den Vlekkert, P. Watts, G. Cerullo, and R. Osellame. Three-dimensional Mach-Zehnder interferometer in a microfluidic chip for spatially-resolved label-free detection. *Lab On a Chip*, 10:1167-1173, 2010
- L. Sansoni, F. Sciarrino, G. Vallone, P. Mataloni, A. Crespi, R. Ramponi, and R. Osellame. Polarization entangled state measurement on a chip. *Physical Review Letters*, 105:200503, 2010
- S. Brivio, D. Polli, A. Crespi, R. Osellame, G. Cerullo, and R. Bertacco. Observation of anomalous acoustic phonon dispersion in SrTiO₃ by broadband stimulated Brillouin scattering. *Applied Physics Letters*, 98:211907, 2011
- A. Crespi, R. Ramponi, R. Osellame, L. Sansoni, I. Bongioanni, F. Sciarrino, G. Vallone, and P. Mataloni. Integrated photonic quantum gates for polarization qubits. *Nature Communications*, 2:566, 2011
- L. Sansoni, F. Sciarrino, G. Vallone, P. Mataloni, A. Crespi, R. Ramponi, and R. Osellame. Two-particle bosonic-fermionic quantum walk via integrated photonics. *Physical Review Letters*, 108:010502, 2012
- A. Crespi, M. Lobino, J.C.F. Matthews, A. Politi, C.R. Neal, R. Ramponi, R. Osellame, and J.L. O'Brien. Measuring protein concentration with entangled photons (*submitted*)
- A. Crespi, S. Longhi, and R. Osellame. Photonic realization of the quantum Rabi model (*submitted*)

Bibliography

- [1] K.M. Davis, K. Miura, N. Sugimoto, and K. Hirao. Writing waveguides in glass with a femtosecond laser. *Opt. Lett.*, 21:1729–1731, 1996.
- [2] G. Della Valle, R. Osellame, and P. Laporta. Micromachining of photonic devices by femtosecond laser pulses. *J. Opt. A-Pure Appl. Opt.*, 11:013001, 2009.
- [3] R.R. Gattass and E. Mazur. Femtosecond laser micromachining in transparent materials. *Nature Photon.*, 2:219–225, 2008.
- [4] B.C. Stuart, M.D. Feit, S. Herman, A.M. Rubenchik, B.W. Shore, and M.D. Perry. Nanosecond-to-femtosecond laser-induced breakdown in dielectrics. *Phys. Rev. B*, 53:1749–1761, 1996.
- [5] C.B. Schaffer, A. Brodeur, and E. Mazur. Laser-induced breakdown and damage in bulk transparent materials induced by tightly focused femtosecond laser pulses. *Meas. Sci. Technol.*, 12:1784–1794, 2001.
- [6] A.P. Joglekar, H. Liu, E. Meyhofer, G. Mourou, and A.J. Hunt. Optics at critical intensity: Applications to nanomorphing. *Proc. Natl. Acad. Sci. USA*, 101:5856–5861, 2004.
- [7] A.M. Streltsov and N.F. Borrelli. Study of femtosecond-laser-written waveguides in glasses. *J. Opt. Soc. Am. B*, 19:2496–2504, 2002.
- [8] W.J. Reichman, D.M. Krol, L. Shah, F. Yoshino, A. Arai, S.M. Eaton, and P.R. Herman. A spectroscopic comparison of femtosecond-laser-modified fused silica using kilohertz and megahertz laser systems. *J. Appl. Phys.*, 99:123112–123112–5, 2006.
- [9] C.W. Ponader, J.F. Schroeder, and A.M. Streltsov. Origin of the refractive-index increase in laser-written waveguides in glasses. *J. Appl. Phys.*, 103:063516, 2008.
- [10] D.J. Little, M. Ams, P. Dekker, G.D. Marshall, and M.J. Withford. Mechanism of femtosecond-laser induced refractive index change in phosphate glass under a low repetition-rate regime. *J. Appl. Phys.*, 108:033110, 2010.
- [11] J.W. Chan, T. Huser, S. Risbud, and D.M. Krol. Structural changes in fused silica after exposure to focused femtosecond laser pulses. *Opt. Lett.*, 26:1726–1728, 2001.
- [12] K. Itoh, W. Watanabe, S. Nolte, and C.B. Schaffer. Ultrafast processes for bulk modification of transparent materials. *MRS Bull.*, 31:620–625, 2006.
- [13] M. Ams, G.D. Marshall, P. Dekker, M. Dubov, V.K. Mezentsev, I. Bennion, and M.J. Withford. Investigation of ultrafast laser–photonic material interactions: Challenges for directly written glass photonics. *IEEE J. Sel. Topics Quantum Electron.*, 14:1370–1381, 2008.
- [14] L. Sudrie, M. Franco, B. Prade, and A. Mysyrowicz. Writing of permanent birefringent microlayers in bulk fused silica with femtosecond laser pulses. *Opt. Commun.*, 171:279–284, 1999.
- [15] E. Bricchi, B.G. Klappauf, and P.G. Kazansky. Form birefringence and negative index change created by femtosecond direct writing in transparent materials. *Opt. Lett.*, 29:119–121, 2004.

- [16] G. Cheng, K. Mishchik, C. Mauclair, E. Audouard, and R. Stoian. Ultrafast laser photoinscription of polarization sensitive devices in bulk silica glass. *Appl. Phys. Lett.*, 80:219–221, 2009.
- [17] A. Marcinkevičius, S. Juodkakis, M. Watanabe, M. Miwa, S. Matsuo, H. Misawa, and J. Nishii. Femtosecond laser-assisted three-dimensional microfabrication in silica. *Opt. Lett.*, 26:277–279, 2001.
- [18] E.N. Glezer, M. Milosavljevic, L. Huang, R.J. Finlay, T.-H. Her, J.P. Callan, and E. Mazur. Three-dimensional optical storage inside transparent materials. *Opt. Lett.*, 21:2023–2025, 1996.
- [19] M. Watanabe, S. Juodkakis, H.B. Sun, S. Matsuo, H. Misawa, M. Miwa, and R. Kaneko. Transmission and photoluminescence images of three-dimensional memory in vitreous silica. *Appl. Phys. Lett.*, 74:3957, 1999.
- [20] S. Eaton, H. Zhang, P. Herman, F. Yoshino, L. Shah, J. Bovatsek, and A. Arai. Heat accumulation effects in femtosecond laser-written waveguides with variable repetition rate. *Opt. Express*, 13:4708–4716, 2005.
- [21] C. B. Schaffer, A. Brodeur, J.F. García, and E. Mazur. Micromachining bulk glass by use of femtosecond laser pulses with nanojoule energy. *Opt. Lett.*, 26:93–95, 2001.
- [22] K. Minoshima, A.M. Kowalewicz, I. Hartl, E.P. Ippen, and J.G. Fujimoto. Photonic device fabrication in glass by use of nonlinear materials processing with a femtosecond laser oscillator. *Opt. Lett.*, 26:1516–1518, 2001.
- [23] R. Osellame, N. Chiodo, G. Della Valle, S. Taccheo, R. Ramponi, G. Cerullo, A. Killi, U. Morgner, M. Lederer, and D. Kopf. Optical waveguide writing with a diode-pumped femtosecond oscillator. *Opt. Lett.*, 29:1900–1902, 2004.
- [24] S.M. Eaton, H. Zhang, M.L. Ng, J. Li, W.-J. Chen, S. Ho, and P.R. Herman. Transition from thermal diffusion to heat accumulation in high repetition rate femtosecond laser writing of buried optical waveguides. *Opt. Express*, 16:9443–9458, 2008.
- [25] D.K.Y. Low, H. Xie, Z. Xiong, and G.C. Lim. Femtosecond laser direct writing of embedded optical waveguides in aluminosilicate glass. *Appl. Phys. A: Mater.*, 81:1633–1638, 2005.
- [26] G. Cerullo, R. Osellame, S. Taccheo, M. Marangoni, D. Polli, R. Ramponi, P. Laporta, and S. De Silvestri. Femtosecond micromachining of symmetric waveguides at 1.5 μm by astigmatic beam focusing. *Opt. Lett.*, 27:1938–1940, 2002.
- [27] Y. Cheng, K. Sugioka, K. Midorikawa, M. Masuda, K. Toyoda, M. Kawachi, and K. Shihoyama. Control of the cross-sectional shape of a hollow microchannel embedded in photostructurable glass by use of a femtosecond laser. *Opt. Lett.*, 28(1):55–57, 2003.
- [28] M. Ams, G. Marshall, D. Spence, and M. Withford. Slit beam shaping method for femtosecond laser direct-write fabrication of symmetric waveguides in bulk glasses. *Opt. Express*, 13:5676–5681, 2005.
- [29] Y. Nasu, M. Kohtoku, and Y. Hibino. Low-loss waveguides written with a femtosecond laser for flexible interconnection in a planar light-wave circuit. *Opt. Lett.*, 30:723–725, 2005.
- [30] R.R. Thomson, H.T. Bookey, N. Psaila, S. Campbell, D.T. Reid, S. Shen, A. Jha, and A.K. Kar. Internal gain from an erbium-doped oxyfluoride-silicate glass waveguide fabricated using femtosecond waveguide inscription. *IEEE Photon. Tech. Lett.*, 18:1515–1517, 2006.
- [31] R. Osellame, N. Chiodo, V. Maselli, A. Yin, M. Zavelani-Rossi, G. Cerullo, P. Laporta, L. Aiello, S. De Nicola, P. Ferraro, A. Finizio, and G. Pierattini. Optical properties of waveguides written by a 26 MHz stretched cavity Ti:sapphire femtosecond oscillator. *Opt. Express*, 13:612–620, 2005.
- [32] M. Ams, G.D. Marshall, P. Dekker, J.A. Piper, and M.J. Withford. Ultrafast laser written active devices. *Laser & Photon. Rev.*, 3:535–544, 2009.
- [33] D.N. Nikogosyan. Multi-photon high-excitation-energy approach to fibre grating inscription. *Meas. Sci. Technol.*, 18:R1, 2007.

- [34] G.D. Marshall, R.J. Williams, N.Jovanovic, M.J. Steel, and M.J. Withford. Point-by-point written fiber-bragg gratings and their application in complex grating designs. *Opt. Express*, 18:19844–19859, 2010.
- [35] H. Zhang, S. Ho, S.M. Eaton, J. Li, and P.R. Herman. Three-dimensional optical sensing network written in fused silica glass with femtosecond laser. *Opt. Express*, 16:14015–14023, 2008.
- [36] K. Sugioka, Y. Hanada, and K. Midorikawa. Three-dimensional femtosecond laser micro-machining of photosensitive glass for biomicrochips. *Laser & Photon. Rev.*, 4:386–400, 2010.
- [37] R. Osellame, H.J.W.M. Hoekstra, G. Cerullo, and M. Pollnau. Femtosecond laser microstructuring: an enabling tool for optofluidic lab-on-chips. *Laser & Photon. Rev.*, 5:442–463, 2011.
- [38] D. Homoelle, S. Wielandy, A.L. Gaeta, N.F. Borrelli, and C. Smith. Infrared photosensitivity in silica glasses exposed to femtosecond laser pulses. *Opt. Lett.*, 24:1311–1313, 1999.
- [39] L. Gui, B. Xu, and T. Chong Chong. Microstructure in lithium niobate by use of focused femtosecond laser pulses. *IEEE Photon. Tech. Lett.*, 16:1337–1339, 2004.
- [40] J. Liu, Z. Zhang, S. Chang, C. Flueraru, and C.P. Grover. Directly writing of 1-to-N optical waveguide power splitters in fused silica glass using a femtosecond laser. *Opt. Commun.*, 253:315–319, 2005.
- [41] S. Nolte, M. Will, J. Burghoff, and A. Tünnermann. Femtosecond waveguide writing: a new avenue to three-dimensional integrated optics. *Appl. Phys. A: Mater.*, 77:109–111, 2003.
- [42] A. Yariv. Coupled-mode theory for guided-wave optics. *IEEE J. Quantum. Electron.*, 9:919–933, 1973.
- [43] A.M. Kowalewicz, V. Sharma, E.P. Ippen, J.G. Fujimoto, and K. Minoshima. Three-dimensional photonic devices fabricated in glass by use of a femtosecond laser oscillator. *Opt. Lett.*, 30:1060–1062, 2005.
- [44] R. Osellame, V. Maselli, N. Chiodo, D. Polli, R. Martinez-Vazquez, R. Ramponi, and G. Cerullo. Fabrication of 3D photonic devices at 1.55 μm wavelength by femtosecond Ti:sapphire oscillator. *Electron. Lett.*, 41:315, 2005.
- [45] A.M. Streltsov and N.F. Borrelli. Fabrication and analysis of a directional coupler written in glass by nanojoule femtosecond laser pulses. *Opt. Lett.*, 26:42–43, 2001.
- [46] S.M. Eaton, W. Chen, L. Zhang, H. Zhang, R. Iyer, J.S. Aitchison, and P.R. Herman. Telecom-band directional coupler written with femtosecond fiber laser. *IEEE Photon. Tech. Lett.*, 18:2174–2176, 2006.
- [47] W.-J. Chen, S.M. Eaton, H. Zhang, and P.R. Herman. Broadband directional couplers fabricated in bulk glass with high repetition rate femtosecond laser pulses. *Opt. Express*, 16:11470–11480, 2008.
- [48] S.M. Eaton, W.J. Chen, H. Zhang, R. Iyer, J. Li, M.L. Ng, S. Ho, J.S. Aitchison, and P.R. Herman. Spectral loss characterization of femtosecond laser written waveguides in glass with application to demultiplexing of 1300 and 1550 nm wavelengths. *J. Lightwave Technol.*, 27:1079–1085, 2009.
- [49] W. Watanabe, T. Asano, K. Yamada, K. Itoh, and J. Nishii. Wavelength division with three-dimensional couplers fabricated by filamentation of femtosecond laser pulses. *Opt. Lett.*, 28:2491–2493, 2003.
- [50] C. Maclair, G. Cheng, N. Huot, E. Audouard, A. Rosenfeld, I.V. Hertel, and R. Stoian. Dynamic ultrafast laser spatial tailoring for parallel micromachining of photonic devices in transparent materials. *Opt. Express*, 17:3531–3542, 2009.
- [51] M. Pospiech, M. Emons, A. Steinmann, G. Palmer, R. Osellame, N. Bellini, G. Cerullo, and U. Morgner. Double waveguide couplers produced by simultaneous femtosecond writing. *Opt. Express*, 17:3555–3563, 2009.

- [52] K. Minoshima, A. Kowalevicz, E. Ippen, and J. Fujimoto. Fabrication of coupled mode photonic devices in glass by nonlinear femtosecond laser materials processing. *Opt. Express*, 10:645–652, 2002.
- [53] C. Florea and K.A. Winick. Fabrication and characterization of photonic devices directly written in glass using femtosecond laser pulses. *J. Lightwave Technol.*, 21:246–253, 2003.
- [54] G. Li, K.A. Winick, A.A. Said, M. Dugan, and P. Bado. Waveguide electro-optic modulator in fused silica fabricated by femtosecond laser direct writing and thermal poling. *Opt. Lett.*, 31:739–741, 2006.
- [55] Y. Liao, J. Xu, Y. Cheng, Z. Zhou, F. He, H. Sun, J. Song, X. Wang, Z. Xu, K. Sugioka, and K. Midorikawa. Electro-optic integration of embedded electrodes and waveguides in LiNbO₃ using a femtosecond laser. *Opt. Lett.*, 33:2281–2283, 2008.
- [56] D.N. Christodoulides, F. Lederer, and Y. Silberberg. Discretizing light behaviour in linear and nonlinear waveguide lattices. *Nature*, 424:817–823, 2003.
- [57] T. Pertsch, U. Peschel, F. Lederer, J. Burghoff, M. Will, S. Nolte, and A. Tünnermann. Discrete diffraction in two-dimensional arrays of coupled waveguides in silica. *Opt. Lett.*, 29:468–470, 2004.
- [58] A. Szameit, D. Blömer, J. Burghoff, T. Pertsch, S. Nolte, and A. Tünnermann. Hexagonal waveguide arrays written with fs-laser pulses. *Appl. Phys. B: Lasers Opt.*, 82:507–512, 2006.
- [59] A. Szameit, F. Dreisow, T. Pertsch, S. Nolte, and A. Tünnermann. Control of directional evanescent coupling in fs laser written waveguides. *Opt. Express*, 15:1579–1587, 2007.
- [60] A. Szameit, J. Burghoff, T. Pertsch, S. Nolte, A. Tünnermann, and F. Lederer. Two-dimensional soliton in cubic fs laser written waveguide arrays in fused silica. *Opt. Express*, 14:6055–6062, 2006.
- [61] A. Szameit, Y.V. Kartashov, F. Dreisow, T. Pertsch, S. Nolte, A. Tünnermann, and L. Torner. Observation of two-dimensional surface solitons in asymmetric waveguide arrays. *Phys. Rev. Lett.*, 98:173903, 2007.
- [62] F. Dreisow, M. Heinrich, A. Szameit, S. Doering, S. Nolte, A. Tünnermann, S. Fahr, and F. Lederer. Spectral resolved dynamic localization in curved fs laser written waveguide arrays. *Opt. Express*, 16:3474–3483, 2008.
- [63] N. Chiodo, G. Della Valle, R. Osellame, S. Longhi, G. Cerullo, R. Ramponi, P. Laporta, and U. Morgner. Imaging of Bloch oscillations in erbium-doped curved waveguide arrays. *Opt. Lett.*, 31:1651–1653, 2006.
- [64] A. Szameit, F. Dreisow, H. Hartung, S. Nolte, A. Tünnermann, and F. Lederer. Quasi-incoherent propagation in waveguide arrays. *Appl. Phys. Lett.*, 90:241113, 2007.
- [65] A. Szameit, Y.V. Kartashov, F. Dreisow, M. Heinrich, T. Pertsch, S. Nolte, A. Tünnermann, V.A. Vysloukh, F. Lederer, and L. Torner. Inhibition of light tunneling in waveguide arrays. *Phys. Rev. Lett.*, 102:153901, 2009.
- [66] L. Martin, G. Di Giuseppe, A. Perez-Leija, R. Keil, F. Dreisow, M. Heinrich, S. Nolte, A. Szameit, A.F. Abouraddy, D.N. Christodoulides, and B.E.A. Saleh. Anderson localization in optical waveguide arrays with off-diagonal coupling disorder. *Opt. Express*, 19:13636–13646, 2011.
- [67] D.R. Reyes, D. Iossifidis, P.A. Auroux, and A. Manz. Micro total analysis systems. 1. Introduction, theory, and technology. *Anal. Chem.*, 74:2623–2636, 2002.
- [68] J. West, M. Becker, S. Tombrink, and A. Manz. Micro total analysis systems: latest achievements. *Anal. Chem.*, 80:4403–4419, 2008.
- [69] D. Mark, S. Haeberle, G. Roth, F. von Stetten, and R. Zengerle. Microfluidic lab-on-a-chip platforms: requirements, characteristics and applications. *Chem. Soc. Rev.*, 39:1153–1182, 2010.
- [70] G.M. Whitesides. The origins and the future of microfluidics. *Nature*, 442:368–373, 2006.
- [71] B. Kuswandi, J. Huskens, and W. Verboom. Optical sensing systems for microfluidic devices: A review. *Anal. Chim. Acta*, 601:141–155, 2007.

- [72] J. Hübner, K.B. Mogensen, A.M. Jorgensen, P. Friis, P. Telleman, and J.P. Kutter. Integrated optical measurement system for fluorescence spectroscopy in microfluidic channels. *Rev. Sci. Instrum.*, 72:229, 2001.
- [73] P. Dumais, C.L. Callender, J.P. Noad, and C.J. Ledderhof. Microchannel-based refractive index sensors monolithically integrated with silica waveguides: Structures and sensitivities. *IEEE Sens. J.*, 8:457–464, 2008.
- [74] C.L. Bliss, J.N. McMullin, and C.J. Backhouse. Rapid fabrication of a microfluidic device with integrated optical waveguides for DNA fragment analysis. *Lab Chip*, 7:1280–1287, 2007.
- [75] R. Osellame, V. Maselli, R. Martinez-Vazquez, R. Ramponi, and G. Cerullo. Integration of optical waveguides and microfluidic channels both fabricated by femtosecond laser irradiation. *Appl. Phys. Lett.*, 90:231118, 2007.
- [76] R. Martinez-Vazquez, R. Osellame, D. Nolli, C. Dongre, H. H. Van den Vlekkert, R. Ramponi, M. Pollnau, and G. Cerullo. Integration of femtosecond laser written optical waveguides in lab-on-chip. *Lab Chip*, 9:91–96, 2009.
- [77] X. Fan, I.M. White, S.I. Shopova, H. Zhu, J.D. Suter, and Y. Sun. Sensitive optical biosensors for unlabeled targets: A review. *Anal. Chim. Acta*, 620:8–26, 2008.
- [78] R.G. Heideman, R.P.H. Kooyman, and J. Greve. Performance of a highly sensitive optical waveguide Mach-Zehnder interferometer immunosensor. *Sens. Actuators B: Chem.*, 10:209–217, 1993.
- [79] M. Weisser, G. Tovar, S. Mittler-Neher, W. Knoll, F. Brosinger, H. Freimuth, M. Lacher, and W. Ehrfeld. Specific bio-recognition reactions observed with an integrated Mach-Zehnder interferometer. *Biosens. Bioelectron.*, 14:405–411, 1999.
- [80] B. Drapp, J. Piehler, A. Brecht, G. Gauglitz, B.J. Luff, J.S. Wilkinson, and J. Ingenhoff. Integrated optical Mach-Zehnder interferometers as simazine immunoprobes. *Sens. Actuators B: Chem.*, 39:277–282, 1997.
- [81] F.J. Blanco, M. Agirregabiria, J. Berganzo, K. Mayora, J. Elizalde, A. Calle, C. Dominguez, and L.M. Lechuga. Microfluidic-optical integrated CMOS compatible devices for label-free biochemical sensing. *J. Micromech. Microeng.*, 16:1006–1016, 2006.
- [82] R.G. Heideman and P.V. Lambeck. Remote opto-chemical sensing with extreme sensitivity: design, fabrication and performance of a pigtailed integrated optical phase-modulated Mach-Zehnder interferometer system. *Sens. Actuators B: Chem.*, 61:100–127, 1999.
- [83] F. Prieto, B. Sepúlveda, A. Calle, A. Llobera, C. Domínguez, and L.M. Lechuga. Integrated Mach-Zehnder interferometer based on ARROW structures for biosensor applications. *Sens. Actuators B: Chem.*, 92:151–158, 2003.
- [84] V. Giovannetti, S. Lloyd, and L. Maccone. Quantum-enhanced measurements: Beating the standard quantum limit. *Science*, 306:1330, 2004.
- [85] K. Goda, O. Miyakawa, E.E. Mikhailov, S. Saraf, R. Adhikari, K. McKenzie, R. Ward, S. Vass, A.J. Weinstein, and N. Mavalvala. A quantum-enhanced prototype gravitational-wave detector. *Nature Phys.*, 4:472–476, 2008.
- [86] K.J. Resch, K.L. Pregnell, R. Prevedel, A. Gilchrist, G.J. Pryde, J.L. O'Brien, and A.G. White. Time-reversal and super-resolving phase measurements. *Phys. Rev. Lett.*, 98:223601, 2007.
- [87] R. Okamoto, H.F. Hofmann, T. Nagata, J.L. O'Brien, K. Sasaki, and S. Takeuchi. Beating the standard quantum limit: phase super-sensitivity of N-photon interferometers. *New J. Phys.*, 10:073033, 2008.
- [88] M.W. Mitchell, J.S. Lundeen, and A.M. Steinberg. Super-resolving phase measurements with a multiphoton entangled state. *Nature*, 429:161–164, 2004.
- [89] T. Nagata, R. Okamoto, J.L. O'Brien, K. Sasaki, and S. Takeuchi. Beating the standard quantum limit with four-entangled photons. *Science*, 316:726, 2007.
- [90] I. Afek, O. Ambar, and Y. Silberberg. High-noon states by mixing quantum and classical light. *Science*, 328:879–881, 2010.

- [91] J.C.F. Matthews, A. Politi, A. Stefanov, and J.L. O'Brien. Manipulation of multiphoton entanglement in waveguide quantum circuits. *Nature Photon.*, 3:346–350, 2009.
- [92] T.D. Ladd, F. Jelezko, R. Laflamme, Y. Nakamura, C. Monroe, and J.L. O'Brien. Quantum computers. *Nature*, 464:45–53, 2010.
- [93] E. Knill, R. Laflamme, and G.J. Milburn. A scheme for efficient quantum computation with linear optics. *Nature*, 409:46–52, 2001.
- [94] J.L. O'Brien, G.J. Pryde, A.G. White, T.C. Ralph, and D. Branning. Demonstration of an all-optical quantum controlled-not gate. *Nature*, 426:264–267, 2003.
- [95] R. Okamoto, H.F. Hofmann, S. Takeuchi, and K. Sasaki. Demonstration of an optical quantum Controlled-NOT gate without path interference. *Phys. Rev. Lett.*, 95:210506, 2005.
- [96] N. Kiesel, C. Schmid, U. Weber, R. Ursin, and H. Weinfurter. Linear optics controlled-phase gate made simple. *Phys. Rev. Lett.*, 95:210505, 2005.
- [97] N.K. Langford, T.J. Weinhold, R. Prevedel, K.J. Resch, A. Gilchrist, J.L. O'Brien, G.J. Pryde, and A.G. White. Demonstration of a simple entangling optical gate and its use in Bell-state analysis. *Phys. Rev. Lett.*, 95:210504, 2005.
- [98] A. Politi, M.J. Cryan, J.G. Rarity, S. Yu, and J.L. O'Brien. Silica-on-silicon waveguide quantum circuits. *Science*, 320:646, 2008.
- [99] A. Politi, J. Matthews, M.G. Thompson, and J.L. O'Brien. Integrated quantum photonics. *IEEE J. Sel. Topics Quantum Electron.*, 15:1673–1684, 2009.
- [100] C.K. Hong, Z.Y. Ou, and L. Mandel. Measurement of subpicosecond time intervals between two photons by interference. *Phys. Rev. Lett.*, 59:2044–2046, 1987.
- [101] G.D. Marshall, A. Politi, J.C.F. Matthews, P. Dekker, M. Ams, M.J. Withford, and J.L. O'Brien. Laser written waveguide photonic quantum circuits. *Opt. Express*, 17:12546–12554, 2009.
- [102] R.P. Feynman. Simulating physics with computers. *Int. J. Theor. Phys.*, 21:467–488, 1982.
- [103] Y. Aharonov, L. Davidovich, and N. Zagury. Quantum random walks. *Phys. Rev. A*, 48:1687–1690, 1993.
- [104] J. Kempe. Quantum random walks: an introductory overview. *Contemp. Phys.*, 44:307–327, 2003.
- [105] M. Mohseni, P. Rebentrost, S. Lloyd, and A. Aspuru-Guzik. Environment-assisted quantum walks in photosynthetic energy transfer. *J. Chem. Phys.*, 129:174106, 2008.
- [106] N. Shenvi, J. Kempe, and K.B. Whaley. Quantum random-walk search algorithm. *Phys. Rev. A*, 67:052307, 2003.
- [107] J.K. Gamble, M. Friesen, D. Zhou, R. Joynt, and S.N. Coppersmith. Two-particle quantum walks applied to the graph isomorphism problem. *Phys. Rev. A*, 81:052313, 2010.
- [108] A.M. Childs. Universal computation by quantum walk. *Phys. Rev. Lett.*, 102:180501, 2009.
- [109] M. Karski, L. Förster, J.-M. Choi, A. Steffen, W. Alt, D. Meschede, and A. Widera. Quantum walk in position space with single optically trapped atoms. *Science*, 325:174–177, 2009.
- [110] H. Schmitz, R. Matjeschk, C. Schneider, J. Glueckert, M. Enderlein, T. Huber, and T. Schaetz. Quantum walk of a trapped ion in phase space. *Phys. Rev. Lett.*, 103:090504, 2009.
- [111] F. Zähringer, G. Kirchmair, R. Gerritsma, E. Solano, R. Blatt, and C. F. Roos. Realization of a quantum walk with one and two trapped ions. *Phys. Rev. Lett.*, 104:100503, 2010.
- [112] C. A. Ryan, M. Laforest, J. C. Boileau, and R. Laflamme. Experimental implementation of a discrete-time quantum random walk on an NMR quantum-information processor. *Phys. Rev. A*, 72:062317, 2005.

- [113] M.A. Broome, A. Fedrizzi, B.P. Lanyon, I. Kassal, A. Aspuru-Guzik, and A.G. White. Discrete single-photon quantum walks with tunable decoherence. *Phys. Rev. Lett.*, 104:153602, 2010.
- [114] A. Schreiber, K. N. Cassemiro, V. Potoček, A. Gábris, P. J. Mosley, E. Andersson, I. Jex, and C. Silberhorn. Photons walking the line: A quantum walk with adjustable coin operations. *Phys. Rev. Lett.*, 104:050502, 2010.
- [115] A. Peruzzo, M. Lobino, J.C.F. Matthews, N. Matsuda, A. Politi, K. Poulios, X.-Q. Zhou, Y. Lahini, N. Ismail, K. Wörhoff, Y. Bromberg, Y. Silberberg, M.G. Thompson, and J.L. O’Brien. Quantum walks of correlated photons. *Science*, 329:1500–1503, 2010.
- [116] A. Schreiber, K. N. Cassemiro, V. Potoček, A. Gábris, I. Jex, and C. Silberhorn. Decoherence and disorder in quantum walks: From ballistic spread to localization. *Phys. Rev. Lett.*, 106:180403, 2011.
- [117] H.B. Perets, Y. Lahini, F. Pozzi, M. Sorel, R. Morandotti, and Y. Silberberg. Realization of quantum walks with negligible decoherence in waveguide lattices. *Phys. Rev. Lett.*, 100:170506, 2008.
- [118] J.O. Owens, M.A. Broome, D.N. Biggerstaff, M.E. Goggin, A. Fedrizzi, T. Linjordet, M. Ams, G.D. Marshall, J. Twamley, M.J. Withford, and A.G. White. Two-photon quantum walks in an elliptical direct-write waveguide array. *New J. Phys.*, 13:075003, 2011.
- [119] S. Longhi. Quantum-optical analogies using photonic structures. *Laser & Photon. Rev.*, 3:243–261, 2009.
- [120] H. Trompeter, W. Krolikowski, D.N. Neshev, A.S. Desyatnikov, A.A. Sukhorukov, Y.S. Kivshar, T. Pertsch, U. Peschel, and F. Lederer. Bloch oscillations and zener tunneling in two-dimensional photonic lattices. *Phys. Rev. Lett.*, 96:53903, 2006.
- [121] S. Longhi, M. Marangoni, M. Lobino, R. Ramponi, P. Laporta, E. Cianci, and V. Foglietti. Observation of dynamic localization in periodically curved waveguide arrays. *Phys. Rev. Lett.*, 96:243901, 2006.
- [122] S. Longhi, G. Della Valle, M. Ornigotti, and P. Laporta. Coherent tunneling by adiabatic passage in an optical waveguide system. *Phys. Rev. B*, 76:201101, 2007.
- [123] A. Perez-Leija, H. Moya-Cessa, A. Szameit, and D.N. Christodoulides. Glauber–Fock photonic lattices. *Opt. Lett.*, 35:2409–2411, 2010.
- [124] R. Keil, A. Perez-Leija, F. Dreisow, M. Heinrich, H. Moya-Cessa, S. Nolte, D.N. Christodoulides, and A. Szameit. Classical analogue of displaced Fock states and quantum correlations in Glauber–Fock photonic lattices. *Phys. Rev. Lett.*, 107:103601, 2011.
- [125] A. Killi, A. Steinmann, J. Dorring, U. Morgner, M.J. Lederer, D. Kopf, and C. Fallnich. High-peak-power pulses from a cavity-dumped Yb:KY(WO₄)₂ oscillator. *Opt. Lett.*, 30:1891, 2005.
- [126] A. Killi and U. Morgner. Solitary pulse shaping dynamics in cavity-dumped laser oscillators. *Opt. Express*, 12:3397–3407, 2004.
- [127] R. Martínez Vázquez, R. Osellame, M. Cretich, M. Chiari, C. Dongre, H.J.W.M. Hoekstra, M. Pollnau, H. van den Vlekert, R. Ramponi, and G. Cerullo. Optical sensing in microfluidic lab-on-a-chip by femtosecond-laser-written waveguides. *Anal. Bioanal. Chem.*, 393:1209–1216, 2009.
- [128] M. Kim, D.J. Hwang, H. Jeon, K. Hiromatsu, and C.P. Grigoropoulos. Single cell detection using a glass-based optofluidic device fabricated by femtosecond laser pulses. *Lab Chip*, 9:311–318, 2009.
- [129] A.J. de Mello. Control and detection of chemical reactions in microfluidic systems. *Nature*, 442:394–402, 2006.
- [130] J.L. Viovy. Electrophoresis of DNA and other polyelectrolytes: Physical mechanisms. *Rev. Mod. Phys.*, 72:813–872, 2000.
- [131] V. Maselli, R. Osellame, G. Cerullo, R. Ramponi, P. Laporta, L. Magagnin, and P.L. Cavallotti. Fabrication of long microchannels with circular cross section using astigmatically shaped femtosecond laser pulses and chemical etching. *Appl. Phys. Lett.*, 88:191107, 2006.

- [132] R.C. West. *Handbook of chemistry and physics*. CRC Press, 1983.
- [133] K.C. Vishnubhatla, N. Bellini, R. Ramponi, G. Cerullo, and R. Osellame. Shape control of microchannels fabricated in fused silica by femtosecond laser irradiation and chemical etching. *Opt. Express*, 17:8685–8695, 2009.
- [134] R. Barer and S. Tkaczyk. Refractive index of concentrated protein solutions. *Nature*, 173:821–822, 1954.
- [135] R. Demkowicz-Dobrzanski, U. Dorner, B.J. Smith, J.S. Lundeen, W. Wasilewski, K. Banaszek, and I.A. Walmsley. Quantum phase estimation with lossy interferometers. *Phys. Rev. A*, 80:13825, 2009.
- [136] M. Kacprowicz, R. Demkowicz-Dobrzanski, W. Wasilewski, K. Banaszek, and I.A. Walmsley. Experimental quantum-enhanced estimation of a lossy phase shift. *Nature Photon.*, 4:357–360, 2010.
- [137] K. Mattle, H. Weinfurter, P.G. Kwiat, and A. Zeilinger. Dense coding in experimental quantum communication. *Phys. Rev. Lett.*, 76:4656–4659, 1996.
- [138] M. Kawachi. Silica waveguides on silicon and their application to integrated-optic components. *Opt. Quantum. Electron.*, 22:391–416, 1990.
- [139] Y. Inoue, H. Takahashi, S. Ando, T. Sawada, A. Himeno, and M. Kawachi. Elimination of polarization sensitivity in silica-based wavelength division multiplexer using a polyimide half waveplate. *J. Lightwave Technol.*, 15:1947–1957, 1997.
- [140] Y. Shimotsuma, P.G. Kazansky, J. Qiu, and K. Hirao. Self-organized nanogratings in glass irradiated by ultrashort light pulses. *Phys. Rev. Lett.*, 91:247405, 2003.
- [141] A.W. Snyder and W.R. Young. Modes of optical waveguides. *J. Opt. Soc. Am.*, 68:297–309, 1978.
- [142] D.F.V. James, P.G. Kwiat, W.J. Munro, and A.G. White. Measurement of qubits. *Phys. Rev. A*, 64:052312, 2001.
- [143] I.L. Chuang and M.A. Nielsen. Prescription for experimental determination of the dynamics of a quantum black box. *J. Mod. Opt.*, 44:2455–2467, 1997.
- [144] I. Bongioanni, L. Sansoni, F. Sciarrino, G. Vallone, and P. Mataloni. Experimental quantum process tomography of non-trace-preserving maps. *Phys. Rev. A*, 82:042307, 2010.
- [145] H. Jeong, M. Paternostro, and M. S. Kim. Simulation of quantum random walks using the interference of a classical field. *Phys. Rev. A*, 69:012310, 2004.
- [146] J. Casanova, G. Romero, I. Lizuain, J.J. García-Ripoll, and E. Solano. Deep strong coupling regime of the Jaynes-Cummings model. *Phys. Rev. Lett.*, 105:263603, 2010.
- [147] T. Niemczyk, F. Deppe, H. Huebl, E.P. Menzel, F. Hocke, M.J. Schwarz, J.J. Garcia-Ripoll, D. Zueco, T. Hümmer, E. Solano, A. Marx, and R. Gross. Circuit quantum electrodynamics in the ultrastrong-coupling regime. *Nature Phys.*, 6:772–776, 2010.
- [148] S. Longhi. Jaynes-Cummings photonic superlattices. *Opt. Lett.*, 36:3407–3409, 2011.
- [149] S. Longhi. Bloch oscillations and Wannier-Stark localization in a tight-binding lattice with increasing intersite coupling. *Phys. Rev. B*, 80:033106, 2009.

‘‘Vanitas vanitatum et omnia vanitas’’